

# Dating circulations of hydrothermal fluids in the crystalline basements of unconformity-related metallic deposits using in situ Rb/Sr geochronology : proof of concept

Quentin Boulogne<sup>1,2\*</sup>, Gaétan Milesi<sup>1,2</sup>, Chantal Peiffert<sup>1</sup>, Emmy Fischer<sup>1,2</sup>, Christophe Ballouard<sup>1</sup>, Mehdi Serdoun<sup>1,3</sup>, Thomas Obin<sup>1,2</sup>, Andreï Lecomte<sup>1</sup>, Pierre Martz<sup>3</sup>, Andrew Kaczowka<sup>4</sup> and Julien Mercadier<sup>1,2</sup>

<sup>1</sup>Université de Lorraine, CNRS, GeoResources, F-54000 Nancy, France

<sup>2</sup>LabCom CREGU, GeoResources, CNRS, Université de Lorraine, Vandœuvre-lès-Nancy, France

<sup>3</sup>Orano Canada, Saskatoon, Canada

<sup>4</sup>Cameco Corporation, Saskatoon, Canada

Correspondence to: Quentin Boulogne ([quentin.boulogne@univ-lorraine.fr](mailto:quentin.boulogne@univ-lorraine.fr))

**Abstract.** The use of *in situ* Rb–Sr geochronology has boomed in recent years following its implementation using LA-ICP-~~QQQ~~-MS/MS technology, which enables fast, *in situ* analyses at the micron scale on selected minerals. The Rb–Sr geochronometer applied to micas is now commonly used to date the crystallization or cooling of metamorphic and magmatic rocks, based on the assumptions of a closed isotopic system after passing the closure temperature and of a homogeneous Sr isotopic composition at the time of crystallization. *In situ* Rb–Sr geochronology applied to micas and related alteration products in geological contexts involving hydrothermal fluid circulation affecting micas after crystallization could provide a new way to decipher the timing and duration of fluid circulation in various settings such as mountain belts or sedimentary basins. The behavior and applicability of the Rb–Sr system in such contexts are, however, poorly understood, as the system may be partially reopened with differential redistribution of Rb and Sr at the grain scale. To test this hypothesis, we selected a case study related to unconformity-related U deposits from the Athabasca Basin (Canada), which formed through intense hydrothermal fluid circulation at the interface between crystalline basement and siliciclastic sedimentary rocks and represent archetypes of unconformity-related metallic deposits. Muscovite grains from metamorphic and magmatic rocks were targeted across a range of alteration states, from hydrothermally unaltered to strongly altered domains. We focused on a specific hydrothermal alteration linked to the formation of hydrothermal illite and sudoite at the expense of metamorphic or magmatic minerals. In unaltered zones, muscovite displayed variable but high Rb/Sr ratios, whereas the <sup>87</sup>Sr/<sup>86</sup>Sr intercepts derived from Rb–Sr regressions were scattered and were not interpreted as meaningful initial isotopic compositions. The resulting ages ranged from ca. 1870 to ca. 1720 Ma and were consistent with the geological context. In distal-to-proximal alteration halos of U deposits, muscovite and related alteration products yielded lower <sup>87</sup>Rb/<sup>86</sup>Sr ratios and highly variable regression intercepts. The mean age calculated across the different samples and investigated sites clustered around ~1640 Ma, a value previously

35 obtained by Ar–Ar geochronology on illite and U–Pb geochronology on other hydrothermal phases and proposed  
36 to correspond to a major hydrothermal event linked to a geodynamic reorganization affecting the Canadian Shield  
37 at the circum-Laurentian scale. The ~1640 Ma age is geologically meaningful in the studied context and is  
38 interpreted as reflecting partial, micrometric-scale resetting of the Rb–Sr system in muscovite during this  
39 hydrothermal event. The wide range of regression intercept values commonly observed in disturbed Rb–Sr  
40 systems is interpreted as an apparent result of open-system behavior, reflecting partial system reopening and non-  
41 conservative redistribution of Rb and Sr at the grain scale, rather than as a physically meaningful initial isotopic  
42 composition. These results demonstrate that detailed analysis of Rb–Sr system perturbations in altered muscovite  
43 and related alteration products can constrain the timing of ancient hydrothermal activity and the spatial dynamics  
44 of fluid-rock interaction. This approach provides a valuable complement to conventional fluid-tracing methods  
45 and opens new perspectives for reconstructing paleo-hydrothermal systems in ancient basement terrains.

46 Key words: Rb–Sr geochronology, Muscovite alteration, Hydrothermal fluid circulation, Athabasca Basin, *In situ*  
47 LA-ICP-MS/MS, Isotopic resetting

## 48 1. Introduction

49 Crystalline basements are environments in which multiple types of fluids can circulate over geological timescales,  
50 depending on the conditions under which these basements formed and later evolved. These fluids may originate  
51 from highly diverse sources (magmatic, metamorphic, basin-derived, meteoric, etc.) and display a wide range of  
52 physicochemical properties and compositions. Their circulation is primarily driven by first-order geological  
53 processes (geodynamic, tectonic, sedimentological, etc.) and is considered to be largely controlled by structural  
54 networks, particularly faults, that enhance permeability and enable surface-derived fluids, for instance, to reach  
55 depths of several kilometers. Beyond faults and their associated damage zones, fluids may also migrate through  
56 broader networks of inherited microfractures and permeable structures within crystalline rocks (e.g., Sibson, 1990;  
57 Faulkner et al., 2010; Viswanathan et al., 2022). These fluids can remain stored for millions of years and may be  
58 mobilized and/or mixed in response to changes in mechanical conditions (e.g., Anders et al., 2014; Frey et al.,  
59 2022). They interact in various ways with the lithologies and mineral assemblages of the basement, inducing  
60 mineralogical, chemical, and/or isotopic modifications that may ultimately lead to the formation of various  
61 resources such as metallic deposits or reservoirs of geothermal waters and metal-rich brines (e.g., Etheridge et al.,  
62 1983; Yardley, 1983). Over the past decades, scientific studies have demonstrated, contrary to earlier assumptions,  
63 that crystalline basements represent favorable environments for fluid circulation and storage (e.g., Juhász et al.,  
64 2002; Walter et al., 2018).

65 Fluids therefore play a key role in the evolution of crystalline basements, and it is of major scientific importance  
66 to identify and date the various episodes of fluid circulation in these environments (e.g., Sibson, 1990; Holness,  
67 2000; Yardley and Bodnar, 2014). Radiometric dating represents a first-order challenge in such contexts, where  
68 multiple fluid types may have circulated successively through the same zone in response to large-scale (tectonic)  
69 or local-scale (fault-related) geological changes (e.g., Rasmussen et al., 2023; Saito et al., 2018; Weinberg et al.,  
70 2020). Each fluid-flow event can leave specific mineralogical markers, often small in size and intermixed with  
71 pre-existing minerals. Isotopic dating is also challenging due to the presence of inherited minerals and initial  
72 isotopic signatures within the basement, which must be distinguished from those specifically related to each fluid  
73 episode (e.g., Dodson, 1973; Grand'Homme et al., 2016). Significant advances have been achieved through the

74 development and application of *in situ* U–Pb dating of hydrothermal minerals (phosphates, titanium oxides,  
75 carbonates, etc.) (e.g., Rasmussen et al., 2001; Rasmussen et al., 2006; Davis et al., 2011; Rabiei et al., 2017;  
76 Adlakha and Hattori, 2021). Recent methodological developments in K–Ar dating of clay minerals emphasize the  
77 systematic separation of multiple grain-size fractions, combined with detailed mineralogical, crystallographic, and  
78 polytype characterization (1Md-1M vs. 2M1 illite), in order to deconvolve mixed detrital and authigenic illite  
79 populations and extract meaningful age information related to distinct crystallization or recrystallization events  
80 (e.g., Reynolds and Thomson, 1993; Velde and Christophe, 1996; Clauer et al., 1997; Hueck et al., 2022; Gerardin  
81 et al., 2024). Such an integrated K–Ar-polytype approach has notably been applied to fault gouges, where dating  
82 different clay fractions allows the timing of synkinematic hydrothermal fluid-faulting episodes to be constrained,  
83 thereby resolving the temporal evolution of brittle deformation and fluid circulation in fault-controlled  
84 hydrothermal systems (e.g., Aldega et al., 2019; Campanha et al., 2026; Schmitz et al., 2025). A limitation of this  
85 approach lies in the fact that these minerals are accessory phases, generally present in limited quantities and/or at  
86 small spatial scales, which creates difficulties in targeting and identification and often requires the use of costly  
87 and time-intensive microscopic techniques, or that they are restricted to specific lithologies or structural contexts.

88 The development of *in situ* Rb–Sr geochronology over the past decade has led to a resurgence of interest in the  
89 use of micas and feldspars as chronometers in crystalline basements, where they are ubiquitous (e.g., Gyomlai  
90 et al., 2023; Jegal et al., 2022; Młynarska et al., 2024; Muñoz-Montecinos et al., 2024). Several studies have  
91 demonstrated the relevance of this approach for dating magmatic (e.g., Larsen and Sundvoll, 2008; Tichomirowa  
92 et al., 2019; Scott Anderson et al., 2015; Bevan et al., 2021) or metamorphic (e.g., Jenkin et al., 2001; Willigers  
93 et al., 2004; Eberlei et al., 2015) events responsible for the crystallization of these minerals, as well as for dating  
94 subsequent thermal and/or fluid-related events that affected these primary minerals after their formation, such as  
95 in the context of hydrothermal gold deposits (Olierook et al., 2020; Liebmann et al., 2022; Ribeiro et al., 2023a,  
96 b; Qiu et al., 2024). These pioneering studies have suggested that the Rb–Sr chronometer may be partially to  
97 completely reset within inherited minerals during post-crystallization fluid and/or thermal events. Furthermore,  
98 this approach could allow direct dating of hydrothermal circulations affecting basement environments using  
99 metamorphic and/or magmatic minerals and their alteration products.

100 The objective of this contribution is to test this hypothesis in the context of paleo-hydrothermal systems developed  
101 at the interface between a crystalline basement and a sedimentary basin. These systems have generated, throughout  
102 Earth history, metallic deposits of various commodities such as Pb, Zn, Cu, U, F, and Ba (e.g., Boiron et al., 2010;  
103 Cathelineau et al., 2012; Oummouch et al., 2017). The case study focuses on the unconformity-related uranium  
104 deposits of the Athabasca Basin (Saskatchewan, Canada), which host the world’s highest-grade uranium deposits.  
105 These deposits have been the subject of intensive scientific research for over sixty years, and much is known about  
106 the typology, age, and geological context of the associated alterations and mineralization. Uranium mineralization  
107 formed during hydrothermal episodes that postdated basin deposition and were active in both basin and basement  
108 settings. These events led to the formation of localized zones of clay-rich alteration, mainly illite and chlorite,  
109 surrounding the orebodies, and are thought to result from interactions between host rocks and evaporitic brines  
110 derived from the basin. Although the formation mechanisms are broadly similar to those responsible for other  
111 unconformity-related metalliferous deposits worldwide, the interpretation of geochronological data in such long-  
112 lived and overprinted hydrothermal systems remains problematic. Existing chronometers commonly yield complex  
113 or equivocal age signatures that do not directly correspond to discrete alteration events. This persistent challenge

underscores the need to evaluate alternative mineral-isotope systems, such as Rb–Sr signatures recorded by basement micas and related hydrothermal products, to more accurately constrain the chronology of alteration associated with the uranium mineralization.

## 2. Geological settings

### 2.1. Geological history of the Wollaston-Mudjatik Transition Zone

The Athabasca Basin unconformably overlies the Archean to Paleoproterozoic basement rocks known as the Western Churchill Structural Province (WSP). The WSP is divided into two lithostructural subprovinces: the Rae Subprovince to the west and the Hearne Subprovince to the east (Annesley et al., 2005) (Fig. 1A). The Trans-Hudson Orogeny (THO), which represents a major Paleoproterozoic belt, is linked to the collision between the Rae, Hearne, and Superior cratons. The beginning of this orogeny is characterized by the amalgamation between 1920 and 1840 Ma of the Rae and Hearne cratons, leading to the formation of the Western Churchill Structural Province (WSP) and to an oceanic arc in the Manikewan Ocean (Ansdell, 2005; Corrigan, 2012; Corrigan et al., 2005, 2009). The gradual closure of the Manikewan Ocean led to the successive accretion of juvenile crustal segments between 1880 and 1860 Ma. The final stage of the THO resulted in the complete closure of the Manikewan Ocean and in the continental collision between the margin of the Hearne craton bordered by the accreted juvenile arcs and the northern edge of the Superior craton between 1830 and 1800 Ma (Corrigan et al., 2009). Finally, the latter stages of THO deformation are marked by the emplacement at ca. 1800 and 1720 Ma of pegmatites and aplites, in relation to sinistral deformation along shear bands in a transpressional context (e.g., Chiarenzelli, 1989; Bickford et al., 1990; Chiarenzelli et al., 1998; Bickford et al., 2005; Schneider et al., 2007).

The western margin of the Hearne Craton comprises two distinct domains of Paleoproterozoic age: the Mudjatik domain and the Wollaston domain (Fig. 1A). The Mudjatik domain is predominantly composed of Archean tonalite-trondhjemite felsic gneiss domes (2.64–2.58 Ga; Annesley et al., 1997a, 1997b, 1999). In contrast, the Wollaston domain is composed mainly of Paleoproterozoic metasediments attributed to the Wollaston Supergroup (deposited at ca. 2050–1860 Ma; Yeo and Delaney, 2007; Tran et al., 2008), including paragneisses, banded iron formations, quartzites, and marbles. These units are interpreted as evidence of sedimentation initially controlled by a passive-margin setting, which evolved into a back-arc basin and then into a foreland basin in response to tectonic processes related to the collision phase (Annesley et al., 2005; Jeanneret et al., 2016). The two lithotectonic domains are separated by the Wollaston-Mudjatik Transition Zone (WMTZ), within which the present study area is located (Fig. 1A). This zone exhibits an anastomosed structure oriented from northeastern to southwestern, a trait that was inherited from the THO. The deformation phases associated with the various stages of THO formation mentioned above can be observed within this zone.

The basement rocks underwent three tectono-metamorphic events. The first event (M1-D1) is dated from ca. 1840 to 1813 Ma based on U–Pb dating of monazite and zircon from migmatitic metapelites of the Wollaston Supergroup. These rocks host a garnet-cordierite ± sillimanite assemblage that experienced partial melting at peak conditions of 750–825 °C and  $\leq 10$  kbar (Annesley et al., 1992, 1997a,b,c, 1999a,b; Jeanneret et al., 2017; Toma et al., 2024). The second event (M2-D2), dated from ca. 1813 to 1770 Ma, is recorded within migmatites and pegmatites. It corresponds to an isothermal decompression down to 0.5–0.9 kbar at temperatures of 750–825 °C, within the stability field of cordierite under suprasolidus conditions, as constrained by U–Pb dating of

152 monazite and zircon (Annesley et al., 1992, 1997a,b,c, 1999a,b; Jeanneret et al., 2017; Toma et al., 2024). The  
153 third event corresponds to an exhumation and orogenic cooling phase. Although its onset is poorly constrained,  
154 this phase is generally considered to extend from ca. ~~1.77 Ga~~1770 Ma (750 °C, ~~0.5 kbar~~GPa) to ca. ~~1.72 Ga~~1720  
155 Ma (350 °C, ~~0.2 kbar~~GPa), as documented by several studies (Annesley and Madore, 1994; Annesley et al., 1992,  
156 1997a,b,c, 2005; Jeanneret et al., 2017; Martz ~~et al.~~, 2017). This exhumation phase is characterized by pronounced  
157 retrograde transformations linked to early-stage hydrothermal activity. These include the breakdown of cordierite  
158 in favour of phyllosilicates, biotite chloritization, remobilization and precipitation of sulfides, graphite, and  
159 muscovite, circulation of quartz-rich fluids, and dissolution-reprecipitation processes affecting monazite and  
160 zircon (Card, 2012, ~~2013~~2014; Card and Noll, 2016). This phase is further constrained by cooling ages derived  
161 from biotite Rb–Sr (Worden et al., 1985; Schneider et al., 2007), muscovite K–Ar (Philippe et al., 1993), and  
162 muscovite Ar–Ar systems (Alexandre et al., 2009).

## 163 2.2. Geological history of the Athabasca Basin

164 The Paleoproterozoic to Mesoproterozoic Athabasca Basin is a large intracratonic basin located in northern  
165 Saskatchewan and Alberta (Ramaekers et al., 2007). The sedimentary sequence of this basin, known as the  
166 Athabasca Supergroup, was deposited between ca. 1760–1720 Ma (Ramaekers et al., 2007; Jeanneret et al., 2016)  
167 and 1541 Ma for the youngest known age (Creaser and Stasiuk, 2007). Stratigraphic, geochronological, and fluid-  
168 inclusion *P-T* data indicate that the basin reached a maximum depth of 2 to 5 km depending on the methods  
169 considered (Pagel et al., ~~1975~~1975a, b; Chi et al., 2018), with a preserved thickness of 1.5 km today (Hobson and  
170 ~~MacAuley~~MacAulay, 1969). The stratigraphic sequence is organized into four major clastic sedimentary sequences  
171 that record a progressive deepening of the basin (Jefferson et al., ~~2007~~2007). The first sequence, represented by  
172 the Fair Point Formation, consists of conglomerates and quartz-pebble arenites infilling the Jackfish Sub-basin,  
173 located in the western part of the basin, during the initial sag phase around 1760 Ma (e.g., Ramaekers et al., 2007;  
174 Pehrsson et al., 2023). The second sequence, including the Smart/Read and Manitou Falls formations, fills the  
175 Cree Sub-basin, situated in the eastern and southeastern parts of the basin, and reflects the development of a  
176 shallow half-graben with NW-directed palaeoflow between 1680 and 1650 Ma (Ramaekers et al., 2007; Jeanneret  
177 et al., 2016; Pehrsson et al., 2023). The third sequence, represented by the Lazenby Lake and Wolverine Point  
178 formations, shows vertical fining and records a major paleoenvironmental shift around 1640 Ma, characterized by  
179 abrupt deepening in the western basin, a marine incursion, and a transition to axial palaeocurrents sourced from  
180 the north or east (Rainbird et al., 2007; Ramaekers et al., 2007), as indicated by vitric tuff layers dated at  $1644 \pm$   
181  $13$  Ma (U–Pb zircon; Rainbird et al., 2007). The final sequence, which includes the Locker Lake, Otherside,  
182 Douglas, and Carswell formations, reflects detrital and marine sedimentation during continued subsidence and  
183 tectonic reorganization associated with the Kuungmi rifting (Pehrsson et al., 2023), notably recorded by organic-  
184 rich black shales of the Douglas Formation dated by Re–Os at  $1541 \pm 13$  Ma (Creaser and Stasiuk, 2007). Overall,  
185 the basin maintains a largely coherent oval geometry with minimal deformation, except for the Ordovician  
186 Carswell impact structure, which locally disrupts the Athabasca Supergroup (Ramaekers et al., 2007; Pehrsson  
187 et al., 2023).

## 188 2.3. Petrographic and metallogenic characteristics of unconformity-related uranium deposits in the 189 Athabasca Basin

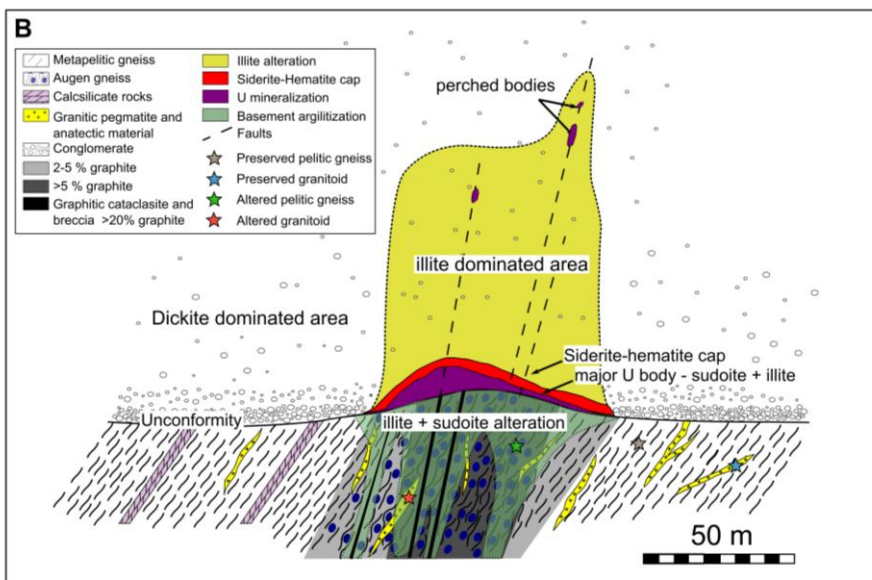
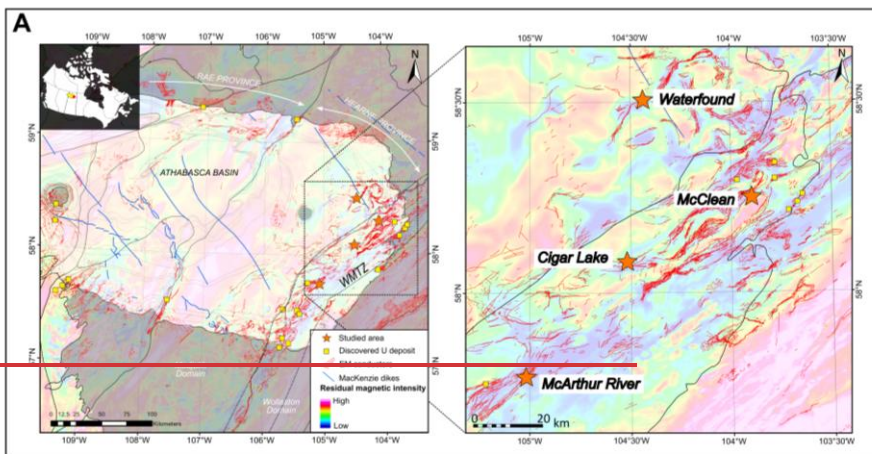
a mis en forme : Police :Italique

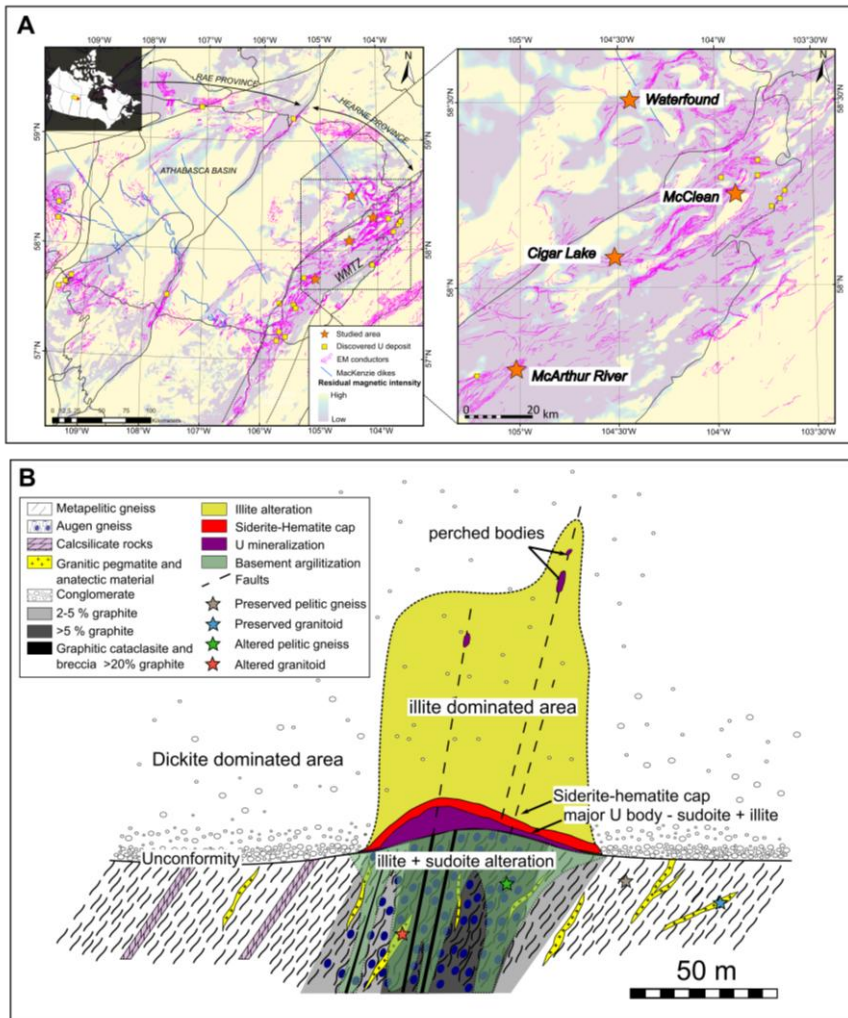
190 The Athabasca Basin unconformity-related uranium deposits are globally renowned for their exceptionally high  
191 grades, reaching up to 20 wt. %  $U_3O_8$ . The principal uranium deposits are concentrated in the eastern part of the  
192 Athabasca Basin and are spatially associated with a NE-SW-trending anastomosed transition zone inherited from  
193 the Trans-Hudsonian Orogeny (THO), commonly referred to as the Wollaston-Mudjatik Transition Zone. This  
194 structural corridor comprises a ca. 50-km-wide network of graphite-rich shear zones, typically described as  
195 graphite conductors, as they exhibit high electrical conductivity, a physical property that allows their detection by  
196 electromagnetic geophysical methods used for uranium exploration (Fig. 1). The uranium deposits are spatially  
197 associated with graphite-rich shear zones, and uranium orebodies show diverse morphologies and structural  
198 associations depending on their location: (i) at the unconformity, within the first meters of sandstones and  
199 conglomerates; (ii) within the basement, extending several hundred meters below the unconformity along shear  
200 zones; or (iii) as perched deposits located tens to hundreds of meters above the unconformity within the  
201 sedimentary sequence. The mineralized zones are surrounded by hydrothermal alteration halos that can extend  
202 several tens of meters into both the basin and the basement and serve as critical geochemical and mineralogical  
203 guides for U exploration. In the basin, alteration halos overlying basement-hosted deposits or surrounding  
204 sandstone-hosted mineralization are dominated by illite, with variable amounts of kaolinite, sudoite (tri-  
205 dioctahedral Mg-chlorite), and dravite (magnesian tourmaline), depending on the deposit.

206 Within the basement, three principal alteration types are superimposed, as exemplified by the world-class Cigar  
207 Lake deposit (Fig. 1C). The first type corresponds to retrograde metasomatic alteration related to the final  
208 exhumation and orogenic cooling phase of the Trans-Hudsonian Orogeny (THO). It is marked by partial to  
209 complete biotite chloritization, discrete quartz and muscovite crystallization, and hydrothermal graphite formation.  
210 These alteration types and their associated petrographic features have been extensively documented in the vicinity  
211 of unconformity-related uranium deposits within the Athabasca Basin (e.g., Carl et al., 1992; Derome et al., 2005;  
212 Cloutier et al., 2011; Mercadier et al., 2011; Alexandre et al., 2012; Adlakha et al., 2015; Martz et al., 2019a;  
213 Menier et al., 2020; Powell et al., 2022). The second type corresponds to regolith alteration developed within the  
214 upper tens of meters of the basement following its exhumation after the Trans-Hudsonian Orogeny. It is  
215 characterized by a laterally correlative weathering profile comprising four zones: (i) a bleached kaolinite-rich and  
216 hematite-depleted zone at the unconformity; (ii) a highly oxidized hematite-rich zone; (iii) a red-green transitional  
217 zone characterized by hematite and chlorite; and (iv) a thicker green-to-red zone enriched in illite, chlorite, and  
218 hematite (e.g., Macdonald, 1980; Halter, 1988). The third type corresponds to post-basin-deposition hydrothermal  
219 alteration, which represents the most extensive alteration type. It is proposed to be linked with uranium  
220 mineralization and is characterized by the massive replacement of primary minerals by an illite- and sudoite-  
221 dominated clay assemblage.

222 The main accepted model for the formation of these deposits is known as “diagenetic-hydrothermal” and involves  
223 the circulation of oxidized brines of marine origin containing NaCl-CaCl<sub>2</sub> at temperatures of around 120 ~~to~~ 200  
224 °C in the basin and underlying bedrock (Derome et al., 2005; Richard et al., 2011, 2013, 2015). The interaction of  
225 these brines with basin and/or basement rocks favors the formation of alteration halos and mobilizes uranium in  
226 its oxidized form ( $U^{6+}$ ), which is transported through fractures and reactivated graphitic structures. Uranium  
227 precipitates within structural and physicochemical traps, where dissolved hexavalent uranium ( $U^{6+}$ ) is reduced to  
228 tetravalent uranium ( $U^{4+}$ ) (Hoeve and Sibbald, 1978; Jefferson et al., 2007).

229 Published absolute ages for the precipitation of primary uranium mineralization at the scale of the basin span a  
230 broad range, from ca. 1590 to 1200 Ma. These estimates derive from U–Pb analyses of UO<sub>2</sub> and from K–Ar or  
231 Ar–Ar geochronology of clay minerals (Cumming and Krstic, 1992; Philippe et al., 1993; McGill et al., 1993;  
232 Fayek [et al., 2002b](#) and [Riciputi, 2002](#); Alexandre et al., 2009; Cloutier et al., 2011; Powell et al., 2022). Building  
233 on these age constraints, an alternative hypothesis invoking an earlier episode of uranium mineralization and/or  
234 hydrothermal alteration merits consideration. Numerous studies have shown that U–Pb systematics of uraninite  
235 and associated alteration minerals in unconformity-related deposits are commonly overprinted by multiple fluid-  
236 flow events, resulting in partial Pb loss and a broad dispersion of apparent ages (Kotzer and Kyser, 1990; Fayek  
237 and Kyser, 1997; Fayek et al., [2002a,b](#); [Fayek and Riciputi, 2002](#); Kyser et al., 2015). Consequently, the  
238 existence of an older hydrothermal system, potentially active in the ca. 1640–1680 Ma interval, cannot be ruled  
239 out and may be cryptic due to subsequent alteration, uranium remobilization, and isotopic resetting during younger  
240 tectono-hydrothermal episodes. This interpretation is consistent with evidence for repeated basin-scale fluid  
241 circulation and late-stage meteoric fluid ingress documented in the Athabasca Basin, processes that are known to  
242 modify both clay mineral K–Ar/Ar–Ar ages and uraninite U–Pb signatures. A similarly complex temporal  
243 evolution is recognized in unconformity-related uranium systems of northern Australia, where *in situ* U–Pb  
244 analyses of uraninite suggest initial mineralization or hydrothermal alteration as early as ca. 1680–1640 Ma,  
245 followed by multiple younger resetting events extending into the Mesoproterozoic and Paleozoic (Clauer et al.,  
246 2015; Skirrow et al., 2016).





248

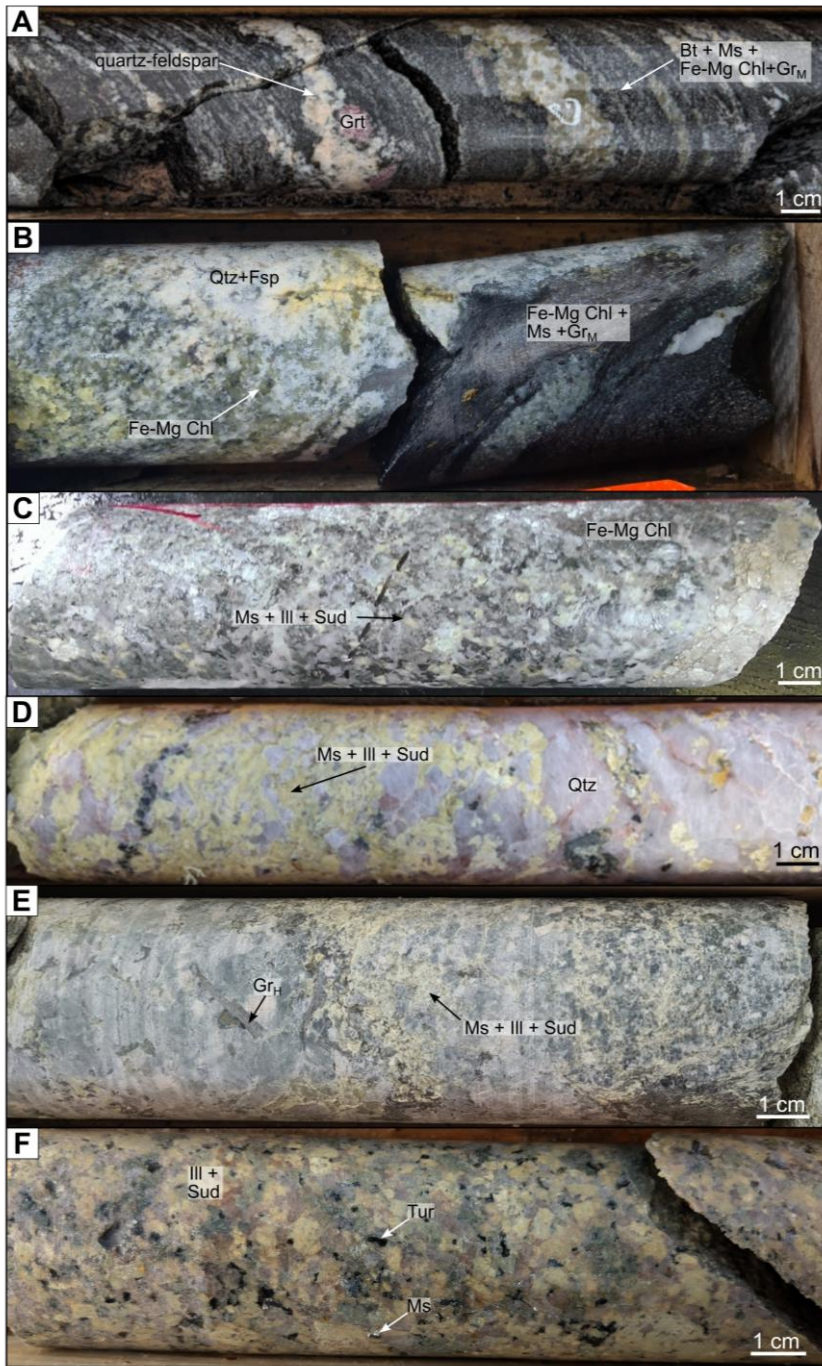
249 Figure 1: (A) Left: map of the Athabasca Basin (Saskatchewan, Canada) with the outline of the different lithotectonic  
 250 units forming the basement. Right: zoom of the study area located in the eastern part of the Athabasca Basin along the  
 251 WMTZ. The red lines represent graphitic conductors: (in magenta) are interpreted from electromagnetic (EM) data  
 252 by the Saskatchewan Geological Survey (SGS) from airborne EM surveys, which correspond to graphitic-rich  
 253 shear zones hosting uranium mineralization. The yellow squares represent deposits or mineralizations with economic  
 254 potential, and the blue stars represent the studied sites. Data source: Saskatchewan Geological Survey (electromagnetic  
 255 data).

256 Map created using ArcGIS Pro. Coordinate Reference System (CRS): WGS 84. (B) Schematic cross-section through  
 257 the main ore body of Cigar Lake, archetype of unconformity-related U deposits. U is located at the unconformity above  
 258 a ductile-brittle graphitic shear zone (Modified after Martz et al., 2019a) and is associated with an alteration  
 259 halo dominated by illite and sudoite in both basin and basement. The theoretical locations of the four types of samples  
 260 examined in this study are indicated by colored stars.

### 261 3. Materials and methods

### 262 3.1. Sampling strategy

263 Four study areas located in the northeastern segment of the Wollaston-Mudjatik Transition Zone (WMTZ) were  
264 selected to evaluate the applicability of in-situ Rb–Sr geochronology to date the main hydrothermal alteration  
265 (illite-sudoite) associated with the U mineralisation within the basement rocks. From north to south, these areas  
266 comprise the Waterfound (WF) and McClean South (MCS) prospects, and the Cigar Lake (CL) and McArthur  
267 River (MAC) deposits. All samples from WF, MCS, and CL analyzed in this study were obtained from drill cores  
268 collected during the past five years as part of U exploration programs conducted by Orano Canada Inc., whereas  
269 samples from MAC were provided by Cameco Corporation. The sampling strategy at the four study sites was  
270 designed to ensure both lateral and vertical representativeness, spanning from unaltered basement zones (Fig. 2A,  
271 B) to hydrothermally altered domains characterized by illite-sudoite assemblages associated with the  
272 mineralization (Fig. 2C, D, E, F). For MCS, five drill holes were considered from west to east: MCS-03, MCS-05,  
273 MCS-34, MCS-35C and MCS-31 (mineralized conductor). For WF, six drill holes were considered from southwest  
274 to northeast: WF-93, WF-98, WF-66, WF-77 and WF-75 (mineralized conductor) and WF-100 (outside the La  
275 Rocque Conductive Corridor). For CL, two drill holes were considered from west to east: WC-449 (mineralized  
276 conductor) and WC-473 (non-mineralized conductor). For MAC, five drill holes were considered from west to  
277 east: MC-408, MC-408-01, MC-418, MC-410-01, MC-410-02 (mineralized conductor). Pelitic gneisses and  
278 anatectic granitoids represent the two dominant lithologies within the WMTZ, particularly within the graphite-rich  
279 shear zones that host mineralization, which justifies their selection for this study. Across all investigated sites, four  
280 samples of pelitic gneisses unaffected by illite-sudoite alteration were analyzed, together with five samples of  
281 anatectic granitoids and/or associated leucosomes that were likewise preserved from this alteration. Their altered  
282 equivalents comprise ten samples of pelitic gneisses affected by illite-sudoite alteration and nineteen samples of  
283 anatectic granitoids and/or leucosomes exhibiting the same alteration signature. All samples were specifically  
284 selected based on their high muscovite modal abundances and the presence of muscovite grains of sufficient size  
285 to enable *in situ* Rb–Sr analyses by LA-ICP-MS.



287 Figure 2. Macroscopic pictures of drill cores intervals sampled for this study (A) Anatectic pelitic gneiss containing  
288 metamorphic graphite (GrM), biotite (Bt), muscovite (Ms) and Fe-Mg chlorite (Fe-Mg Chl) within the restite; the  
289 contact between the quartz-feldspar leucosome (Qtz+Fsp) and the restite is marked by garnet. Evidence of retro-  
290 metamorphic alteration is visible within the quartz-feldspar leucosome and is characterized by a fir-green coloration  
291 [MC-408\_591.3 m]. (B) Anatectic pelitic gneiss showing an accumulation of metamorphic graphite in the restite; the  
292 quartz-feldspar leucosome exhibits retro-metamorphic alteration features, with Fe-Mg chlorite imparting a dark green  
293 coloration to the core rock [MCS-05\_285.5 m]. The restite is composed of metamorphic graphite, biotite, muscovite. (C)  
294 Strongly altered granitoid characterized by nearly complete replacement of feldspars and plagioclase by illite and  
295 sudoite (Ill+Sud), while quartz and ferromagnesian chlorites remain preserved. Here, muscovite is embedded within  
296 the illite-sudoite assemblage and is not macroscopically observable [WC-449\_434.4 m]. (D) Granitoid exhibiting  
297 pervasive illite-sudoite alteration, within which muscovite is entirely incorporated into the fine-grained alteration  
298 matrix and is not discernible at the macroscopic scale [MC-410-02\_687.4 m]. (E) Anatectic pelitic gneiss hosting  
299 hydrothermal graphite concentrations within the leucosome, associated with the retrograde metamorphic features and  
300 an illite-sudoite alteration matrix in which muscovite is cryptic and not macroscopically distinguishable. [MCS-34\_273.7  
301 m]. (F) Granitoid exhibiting intense illite-sudoite alteration of primary minerals, imparting an apple-green coloration  
302 to the entire drill core, with muscovite and tourmaline also locally preserved and macroscopically visible [WF-93\_581.0  
303 m].

## 304 3.2. Methods

305 Scanning electron microscopy (SEM), electron probe microanalysis (EPMA), and micro-X-ray fluorescence  
306 ( $\mu$ XRF) analyses were performed at the Service Commun de Microscopies Électronique et de Microanalyse X  
307 (SCMEM) in Nancy, France, whereas *in situ* Rb–Sr isotopic analyses were carried out on the ICP platform at  
308 GeoRessources, Université de Lorraine (Nancy, France).

### 309 3.2.1. Petrography - Optical and SEM

310 Samples were first observed using a conventional optical microscope under transmitted light. Thin-section scale  
311 mapping was conducted using a Keyence VHX-2000 optical microscope. Muscovite and associated minerals were  
312 imaged using a TESCAN VEGA 3 LM scanning electron microscope (SEM). This SEM is equipped with a  
313 conventional tungsten filament and is coupled to two Bruker XFlash 6–30 mm<sup>2</sup> EDS detectors. The backscattered  
314 electron (BSE) images were obtained using the following parameters: an accelerating voltage of 15 kV, a working  
315 distance (WD) of 15 mm, a beam current of 0.5 nA, and an acquisition speed of 1 ms per pixel.

### 316 3.2.2. X-ray fluorescence (XRF)

317 Thin sections were analyzed using a BRUKER M4 TORNADO micro-XRF, which enables localized analysis of  
318 elements ranging from sodium to uranium, with a maximum spatial resolution of approximately 20  $\mu$ m and a  
319 sensitivity varying from around one percent for light elements (Na) to several tens of ppm for more sensitive  
320 elements (Zr). The device is equipped with a rhodium X-ray tube, polycapillary optics to focus the beam and two  
321 Bruker SDD-type EDS detectors to ~~enhance~~enhance acquisition speed, allow for the identification of diffraction  
322 peaks, and reduce shadowing effects. Mapping parameters included a 35  $\mu$ m step size, with a dwell time of 10 ms,  
323 corresponding to a scan speed of 3.5 mm/s. X-ray tube parameters were set to 400  $\mu$ A and 50 kV, under a ~~20-mbar~~  
324 Pa vacuum.  $\mu$ -XRF data were subsequently processed using the M4 TORNADO software to generate elemental  
325 maps.

### 326 3.2.3. Electron probe microanalysis (EPMA)

327 X-ray elemental maps of K ( $K\alpha$ ), Rb ( $K\alpha$ ), Mg ( $K\alpha$ ), Al ( $K\alpha$ ), Ca ( $K\alpha$ ), F ( $K\alpha$ ), Fe ( $K\alpha$ ), Mn ( $K\alpha$ ) and Na ( $K\alpha$ )  
328 on selected areas in thin sections were carried out using a CAMECA SX5 TACTIS electron microprobe, equipped

329 with a LaB<sub>6</sub> tip and five vertical WDS spectrometers. The analytical conditions included a beam current of 100  
330 nA, an accelerating voltage of 25 kV, and a counting time of 20 ms per pixel.

#### 331 3.2.4. In situ Rb–Sr isotopic analysis (LA-ICP-MS/MS)

332 *In situ* Rb–Sr analyses on muscovite were carried out using a LA-ICP-MS/MS system. The <sup>87</sup>Rb/<sup>86</sup>Sr and <sup>87</sup>Sr/<sup>86</sup>Sr  
333 ratios of the studied samples and reference materials were determined using an Agilent 8900 ICP-QQQMS/MS  
334 coupled with a 193 nm ArF excimer laser ablation system ESI 193 nm ArF with a TwoVol2 dual-volume ablation  
335 cell. All samples were ablated employing a 50 μm spot size for 90 to 110 s (30 to 40 s of gas blank measurement  
336 and 30 to 40 s of ablation time followed by 30 s of sample washout), with a repetition rate of 10 Hz and a laser  
337 energy density of 6 J.cm<sup>-2</sup>. Helium at a flow rate of 700 mL.min<sup>-1</sup> was used as a carrier gas in the ablation cell,  
338 then mixed with N<sub>2</sub> via a Y connector at a flow rate of 4 mL min<sup>-1</sup> and argon nebulization gas at a flow rate of 700  
339 mL.min<sup>-1</sup> before entering the ICP-MS torch. The reaction gas N<sub>2</sub>O was used to overcome isobaric interferences  
340 to separate <sup>87</sup>Sr from <sup>87</sup>Rb due to the efficiency of N<sub>2</sub>O in reacting with Sr<sup>+</sup> to form SrO<sup>+</sup> ions, which was not the  
341 case for Rb<sup>+</sup>. The following isotopes were measured (integration time in parentheses): <sup>28</sup>Si → <sup>28</sup>Si (2 ms), <sup>84</sup>Sr →  
342 <sup>84</sup>Sr (5 ms), <sup>84</sup>Sr → <sup>100</sup>SrO (120 ms), <sup>85</sup>Rb → <sup>85</sup>Rb (20 ms), <sup>85</sup>Rb → <sup>101</sup>Rb (5 ms), <sup>86</sup>Sr → <sup>86</sup>Sr (5 ms), <sup>86</sup>Sr → <sup>102</sup>SrO  
343 (120 ms), <sup>87</sup>Sr → <sup>87</sup>Sr (5 ms), <sup>87</sup>Sr → <sup>103</sup>SrO (120 ms), <sup>88</sup>Sr → <sup>88</sup>Sr (5 ms), <sup>88</sup>Sr → <sup>104</sup>SrO (120 ms). A scan of all  
344 isotopes (sampling period) took approximately 565 ms. Seven sessions were conducted to analyze all samples.  
345 The NIST SRM 610 glass (Woodhead and Hergt, 2001) and MicaMg mica (Hogmalm et al., 2017, Jegal et al.,  
346 2022) were used as external standards for the correction of the <sup>87</sup>Sr/<sup>86</sup>Sr and <sup>87</sup>Rb/<sup>86</sup>Sr ratios, respectively. La Posta  
347 biotite was used as a secondary reference material, with a reported weighted mean age of 91.6 ± 1.2 Ma (Zack and  
348 Hogmalm, 2016), to verify the instrumental and analytical conditions. LA-ICPMS/MS data were processed using  
349 the Lolite 4 software. Although matrix effects between phlogopite and natural muscovite cannot be entirely excluded  
350 when using MicaMg as primary reference material for <sup>87</sup>Rb/<sup>86</sup>Sr correction (Glorie et al., 2024), its use currently  
351 remains unavoidable as it represents the only widely available and internationally distributed nano-powder  
352 reference material specifically designed and validated for in situ Rb–Sr dating by LA-ICP-MS/MS. La Posta biotite  
353 was used as a secondary reference material to monitor the stability of the instrumental setup and the long-term  
354 reproducibility of the analytical protocol. It has a reported weighted mean age of 93.8 ± 2.5 Ma and an initial  
355 <sup>87</sup>Sr/<sup>86</sup>Sr ratio of 0.70483 ± 0.0005 (ID-TIMS, Walawender et al., 1990). The Sr/Sr<sub>i</sub> value for La Posta calculated  
356 using NIST 610 was consistent and further confirmed by the value calculated for MicaMg via NIST 610.  
357 Reproducing both the reference age and the initial Sr isotopic composition provides an independent assessment of  
358 analytical accuracy. To quantitatively evaluate long-term reproducibility, La Posta analyses acquired over a three-  
359 year period were grouped by analytical session. For each session, an isochron age was calculated independently.  
360 The resulting session ages were then combined using a weighted mean, in which each session age was weighted  
361 by the inverse square of its internal uncertainty, and the dispersion of individual session ages around this weighted  
362 mean, quantified as the standard deviation of the weighted residuals, yields an external reproducibility of  
363 approximately 1.6% (2σ), which is adopted as a realistic estimate of long-term analytical uncertainty  
364 (Supplementary Figure S1). Final age uncertainties reported in this study incorporate both the internal analytical  
365 uncertainty and this external reproducibility through quadrature propagation, such that σ<sub>total</sub> = √(σ<sub>internal</sub><sup>2</sup> +  
366 σ<sub>reproducibility</sub><sup>2</sup>). The overall weighted mean age is 93.9 ± 1.2 Ma (2σ) with an MSWD of 0.38. In addition,  
367 regression intercepts from individual sessions were compiled to calculate a weighted mean initial <sup>87</sup>Sr/<sup>86</sup>Sr ratio of  
368 0.7045 ± 0.0018 (2σ). This value is in excellent agreement with the ID-TIMS constrained value of 0.70483 reported

369 by Walawender et al. (1990). The consistency of both age and intercept values over three years demonstrates robust  
370 long-term stability of Sr isotopic measurements. These results indicate no evidence for significant instrumental  
371 drift, calibration bias, or matrix-dependent effects, and effectively exclude an analytical origin for the anomalously  
372 low initial  $^{87}\text{Sr}/^{86}\text{Sr}$  values observed in some samples. LA-ICP-MS/MS data reduction was performed using Lolite  
373 4 (Paton et al., 2011). The processed and calibrated data for  $^{87}\text{Sr}/^{86}\text{Sr}$  and  $^{87}\text{Rb}/^{86}\text{Sr}$  ratios were plotted in  
374 conventional isochron and radial plots and used to calculate Rb–Sr isochron ages and corresponding regression  
375 intercepts using IsoplotR (Vermeesch, 2018). In the following, regression intercepts refer strictly to the  
376 mathematical intercepts of Rb–Sr regressions and are not interpreted as true initial  $^{87}\text{Sr}/^{86}\text{Sr}$  ratios.

377 Concentrations of  $^{87}\text{Rb}$ ,  $^{86}\text{Sr}$ , and  $^{87}\text{Sr}$  were calculated from LA-ICP-MS isotopic measurements using a  
378 reproducible procedure that accounts for isotopic abundances, measured Rb–Sr ratios, and matrix effects. Total  
379  $^{87}\text{Rb}$  concentrations (ppm) were derived from the measured  $^{85}\text{Rb}$  signal by correcting for the natural isotopic  
380 abundances ( $^{85}\text{Rb} = 0.7217$ ,  $^{87}\text{Rb} = 0.2783$ ) of Rb according to Eq. (1):

$$(1) \quad ^{87}\text{Rb} = ^{85}\text{Rb}_{\text{measured}} \times \frac{0.7217}{0.2783}$$

382 Concentrations of  $^{86}\text{Sr}$  were then calculated from the measured  $^{87}\text{Rb}/^{86}\text{Sr}$  ratios obtained from the Rb–Sr regression  
383 diagrams according to Eq. (2):

$$(2) \quad ^{86}\text{Sr} = \frac{^{87}\text{Rb}}{(^{87}\text{Rb}/^{86}\text{Sr})_{\text{measured}}}$$

386 Subsequently,  $^{87}\text{Sr}$  concentrations were calculated using the measured  $^{87}\text{Sr}/^{86}\text{Sr}$  ratios according to Eq. (3):

$$(3) \quad ^{87}\text{Sr} = (^{87}\text{Sr}/^{86}\text{Sr})_{\text{measured}} \times ^{86}\text{Sr}$$

389 To correct for instrumental fractionation and sample–standard differences, a matrix correction factor of 0.532038  
390 was applied to all calculated concentrations according to Eq. (4):

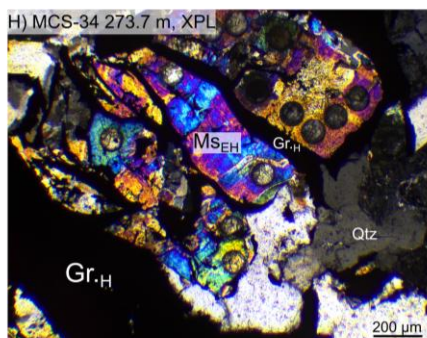
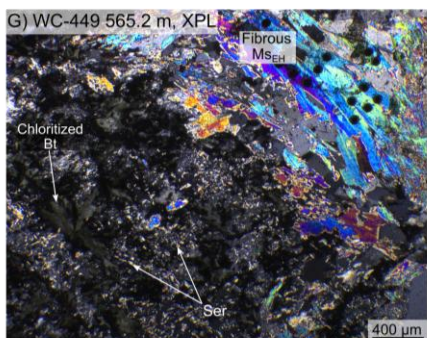
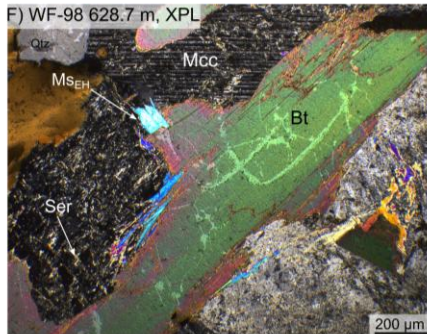
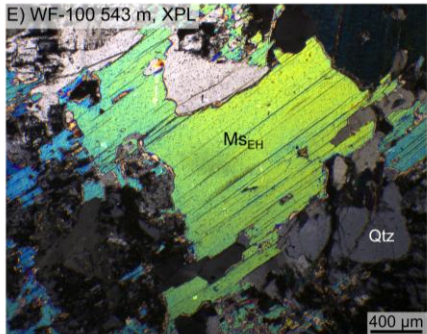
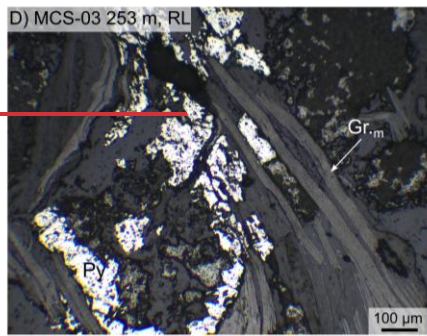
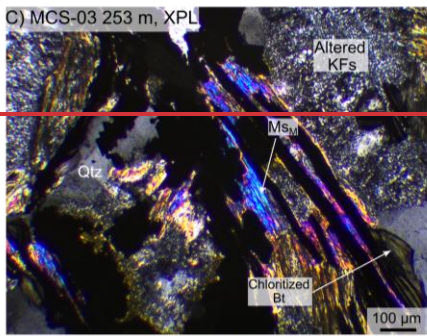
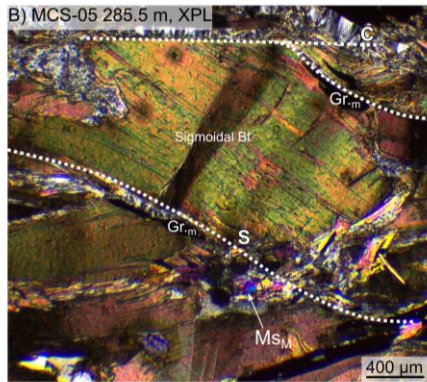
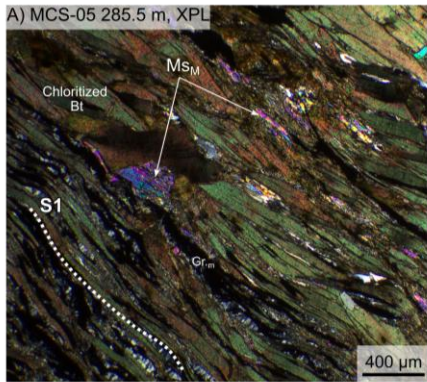
$$(4) \quad C_{\text{corrected}} = C_{\text{calculated}} \times 0.532038$$

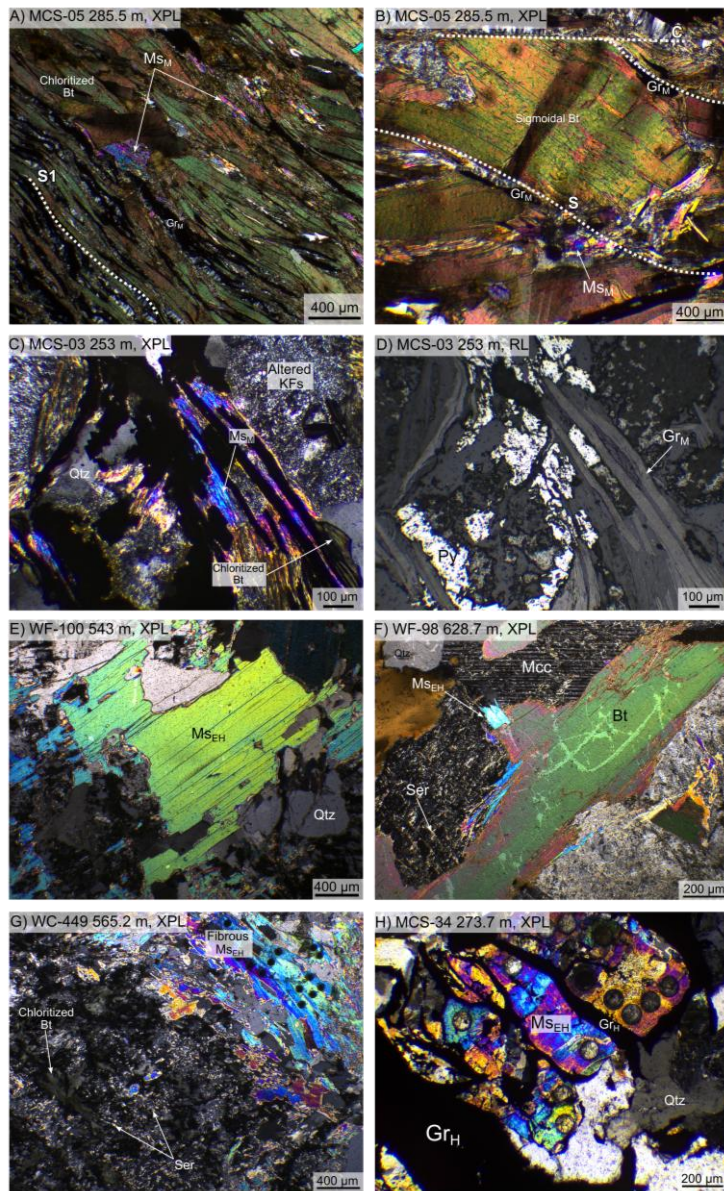
392 This factor was determined from the internal standard MicaMg by comparing the measured  $^{85}\text{Rb}$  concentration  
393 with its published reference value (Jegal et al., 2022) and then applied proportionally to  $^{87}\text{Rb}$ ,  $^{87}\text{Sr}$ , and  $^{86}\text{Sr}$  in all  
394 samples. The complete dataset of raw Rb–Sr isotopic ratios, single-spot ages, uncertainties, and matrix-corrected  
395 elemental concentrations is provided in Supplement Table S1.

#### 396 4. Results

397 Two types of muscovite, identified in the least altered zones of the metasomatic halos, were investigated (Fig. 2A  
398 and B): (i) (retro-)metamorphic muscovite associated with the retrograde mineral assemblage within metamorphic  
399 rocks and (ii) early hydrothermal muscovite within magmatic rocks as a secondary phase. All of the studied  
400 samples exhibit evidence of a first -alteration associated with the retrograde metamorphism and are variably  
401 overprinted by a second hydrothermal alteration that is described below.

402





404  
 405 Figure 3. (A-B) Graphitic pelitic gneiss [MCS-05\_285.5 m]. (A) Pelitic gneiss displaying a well-developed foliation.  
 406 Biotite (Bt) and thick flakes of metamorphic graphite (~~GrM~~~~GrM~~) are aligned along the S1 foliation, while retrograde  
 407 metamorphic muscovite (MsM) crystallizes at the rims of biotite, perpendicular to S1. (B) Plastically deformed biotite  
 408 marking a C-S fabric, with fine-grained metamorphic muscovite precipitating around biotite and within biotite pressure  
 409 shadows. (C-D) Graphitic pelitic gneiss with retrograde mineral assemblage [MCS-03\_253 m]. Assemblage of quartz  
 410 (Qtz), K-feldspar (KFs), metamorphic muscovite, pyrite (Py), and metamorphic graphite, ~~together~~ that has undergone  
 411 chloritization related to retrograde metamorphic alteration. Metamorphic muscovite is aligned with tabular flakes of  
 412 metamorphic graphite. (E-F) Granitoid rocks [~~WF-100\_543 m~~]. (E) Subhedral early hydrothermal muscovite

(MS<sub>Fe</sub>, MS<sub>FeII</sub>) crystals. [WF-100\_543 m]. (F) Assemblage of biotite, quartz, and microcline (Mcc), showing early stages of sericitization (Ser). Early hydrothermal muscovite precipitated as a secondary phase along biotite grain boundaries and has locally replaced, now altered and sericitized, K-feldspar [WF-98\_628.7 m]. (G) Leucosome of metapelitic gneiss characterized by fibrous aggregates of early hydrothermal muscovite crosscutting partially to completely chloritized biotite [WC-449\_565.2 m]. (H) Leucosome of metapelitic gneiss with early hydrothermal muscovite associated with large flakes of hydrothermal graphite (Gr<sub>H</sub>) [MCS-34\_273.7 m].

a mis en forme : Indice

#### 4.1. Metamorphic muscovite

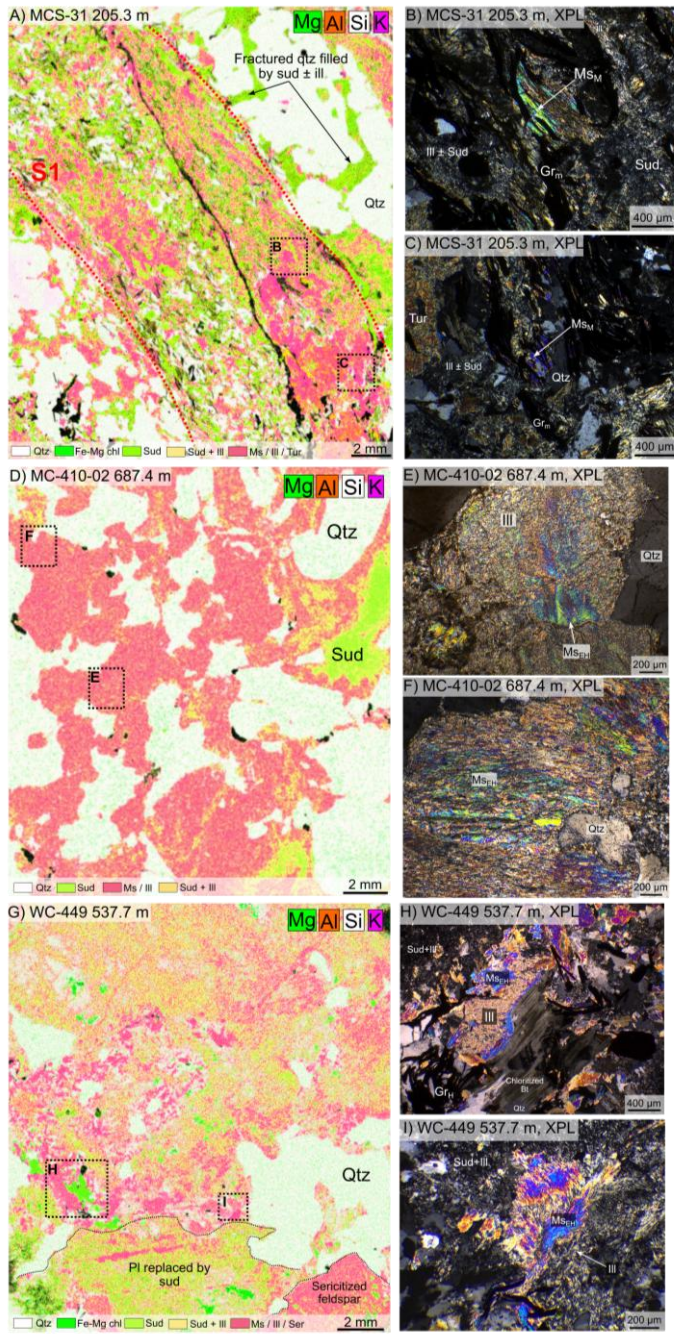
Metamorphic muscovite is exclusively developed along the foliation planes of Palaeoproterozoic metapelites (Fig. 2A,B) (e.g., Schneider et al., 2007; Skipton et al., 2016; Jeanneret et al., 2017; Martz *et al.*, 2017). These rocks are characterized by quartz and sericitized K-feldspar, and are bounded by graphite-rich shear zones containing biotite, muscovite, and pyrite (Fig. 3A). Biotite occurs as lath-shaped crystals, locally plastically deformed showing C-S planes, ranging from 0.5 to 1 mm in length, and oriented parallel to the subvertical S1 foliation. Muscovite is present as euhedral to subhedral crystals, predominantly crystallizing along the rims of metamorphic biotite, with an orientation perpendicular to the S1 foliation, suggesting a crystallization stage postdating biotite growth possibly along the retrograde *P-T* path (Fig. 3A). Muscovite is also present within pressure shadows around biotite mica-fish, suggesting that muscovite crystallization was contemporaneous with ductile deformation (Fig. 3B). Metamorphic biotites are locally pseudomorphosed by Fe-Mg chlorite, a marker of retrograde metamorphism or fluid-induced alteration (Fig. 3C). The metamorphic muscovite is commonly associated with medium-sized, euhedral to tabular flakes of metamorphic graphite aligned along the foliation. Sulfides such as pyrite and chalcopyrite are frequently associated with this metamorphic graphite (Fig. 3D).

a mis en forme : Police :Italique

#### 4.2. Early hydrothermal muscovite

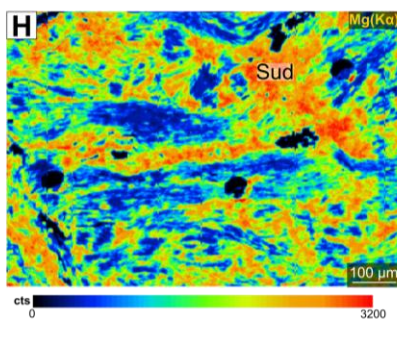
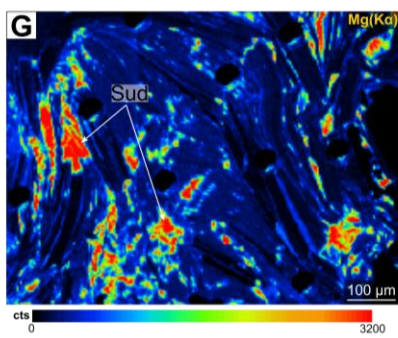
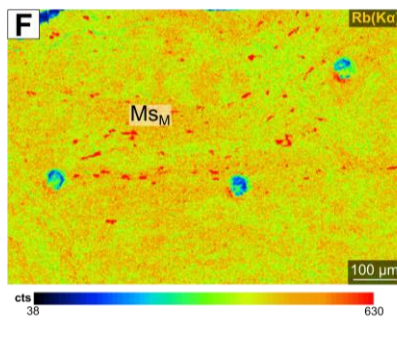
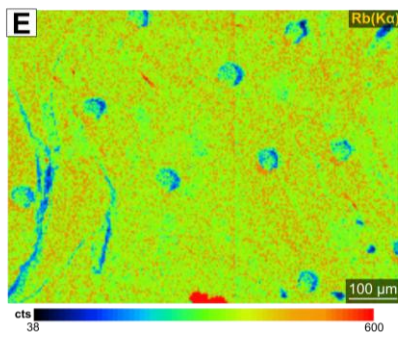
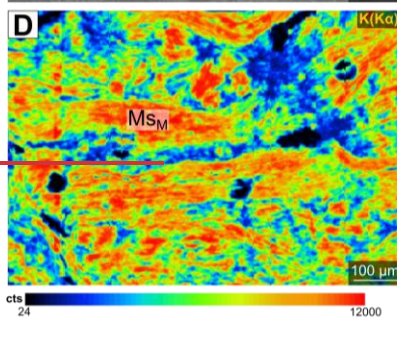
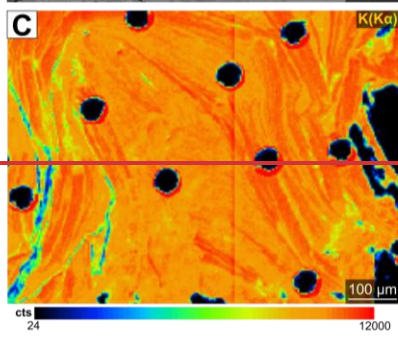
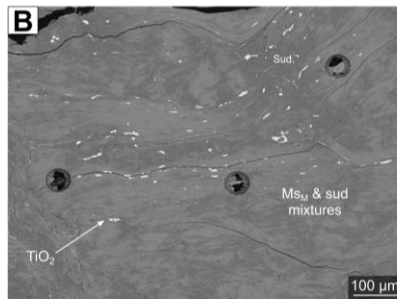
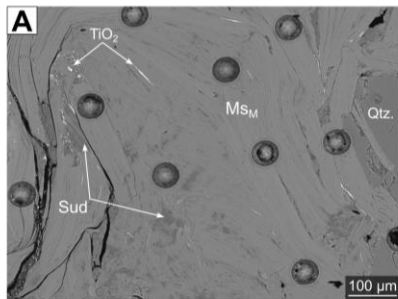
Early hydrothermal muscovite occurs within anatectic granitoids or within the leucosomes of metapelitic gneisses (Fig. 2C, D, E, F) (e.g., Schneider et al., 2007; Skipton et al., 2016; Martz *et al.*, 2017; Obin, 2025). These lithologies are primarily composed of quartz, K-feldspar of the microcline type, often altered to sericite forming very fine microlamellar aggregates with a shimmering whitish-grey appearance, plagioclase, and biotite laths, which are partially to completely pseudomorphosed by Fe-Mg chlorite (Fig. 3E, F). Muscovite in these rocks occurs either as subhedral crystals or as fibrous aggregates that may have partially to completely replaced chloritized biotite or have precipitated along biotite grain boundaries as fine-grained crystals (Fig. 3E, F, G). It may also have locally replaced K-feldspar (Fig. 3F). Muscovite is frequently associated with hydrothermal graphite, which occurs as large flakes (up to 0.5 cm) precipitating interlayered with muscovite within late fractures or forming radiating patterns in granitic leucosomes (Fig. 3H). These lithologies may also be locally enriched in tourmaline, occurring as euhedral to subhedral crystals with strong relief and second-order yellow to green interference colors. Accessory phases include zircon, monazite, and apatite, present as subhedral crystals or as veinlets crosscutting the aforementioned minerals.

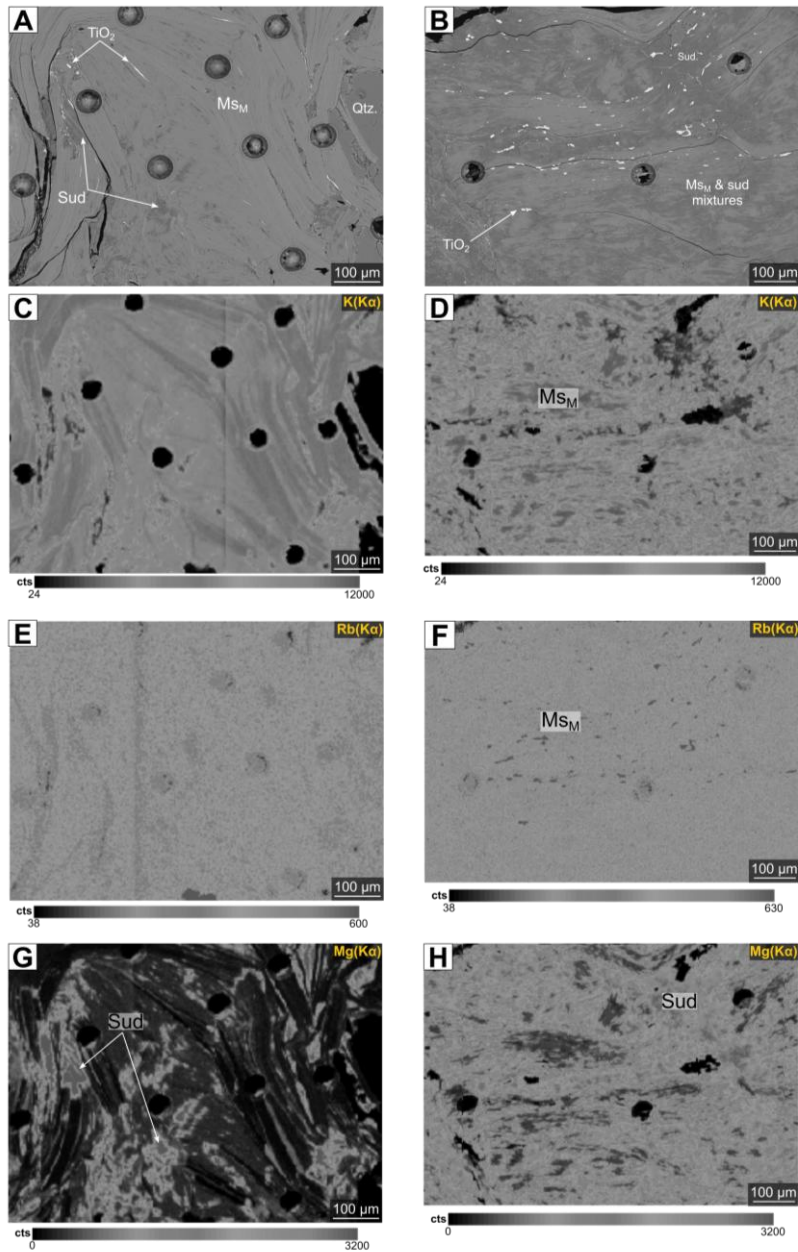
#### 4.3. Petrographic characteristics of altered muscovites



449 **Figure 4. (A) Micro-X-ray fluorescence ( $\mu$ -XRF) elemental maps of a thin section showing the distribution of Mg, Al, Si,**  
450 **and K within a migmatitic graphitic pelitic gneiss including a leucosome [MCS-31\_205.3 m]. Illite (Ill)-sudoite (Sud)**  
451 **alteration is hosted along the mylonitic foliation planes of pelitic gneisses and occurs pervasively within the leucosome.**  
452 **Sudoite also precipitates within fractures crosscutting the quartz (Qtz) vein. (B-C) Magnified views of (A) showing illite-**  
453 **sudoite alteration affecting metamorphic muscovite (Msm). (D)  $\mu$ -XRF elemental mapping displaying the Mg, Al, Si,**  
454 **and K distribution within an anatectic granitoid [MC-410-02\_687.4 m]. Illite/sudoite ratios vary across the sample, with**  
455 **domains that are fully illitized and others enriched in sudoite. (E-F) Magnified views of (D) illustrating the illitization**  
456 **of early hydrothermal muscovite (MseH). (G)  $\mu$ -XRF elemental maps showing the Mg, Al, Si, and K distribution within**  
457 **an anatectic granitoid [WC-449\_537.7 m]. Illite and sudoite crystallize pervasively, with spatial variations in the**  
458 **illite/sudoite ratio. (H-I) Magnified views of (G) showing early hydrothermal muscovite illitization and the coexistence**  
459 **of illite-sudoite replacing early minerals. Biotite associated with early hydrothermal muscovite is completely chloritized.**

460 This hydrothermal alteration affects both metamorphic muscovite (Figs. 4A-C) and early hydrothermal muscovite  
461 (Figs. 4D-I). This Mg-K-type alteration pervasively affects the two lithologies that constitute the graphite-rich  
462 shear zones, whether through the mylonitic foliation planes of pelitic gneisses (Figs. 4A-C), the grain boundaries  
463 of magmatic to early hydrothermal minerals in anatectic granitoids and leucosomes (Figs. 4D-I), or through  
464 fracture networks indiscriminately crosscutting the two lithologies. At the microscopic scale, this alteration is  
465 expressed by the extensive replacement of primary and retro-metamorphic minerals by a clay assemblage  
466 predominantly composed of micrometric illite, spatially associated with sudoite (a magnesium-rich trioctahedral  
467 chlorite). However, this alteration is not uniformly distributed within the different lithologies, and the illite/sudoite  
468 ratio varies between lithologies and within the same lithology (Figs. 4D, G). In anatectic granitoids and  
469 leucosomes, the alteration is marked by the partial replacement of K-feldspar and the complete replacement of  
470 plagioclase, which are more prone to alteration, by this clay assemblage (Figs. 4D-I). Fractures crosscutting quartz  
471 and feldspars are commonly filled with illite and/or sudoite crystals (Fig. 4A). The cleavage planes of muscovite  
472 are partially to completely disrupted, and their birefringence colors approach those of illite, reflecting the onset of  
473 muscovite illitization, particularly visible along grain margins (Figs. 4E, F, H, I). Under cross-polarized light, illite  
474 occurs as lath-shaped crystals (Figs. 4E, F, H, I). Sudoite appears as needle-like crystals with low relief, generally  
475  $<2 \mu\text{m}$  in length (Figs. 4B, C, H, I). Figure 5 highlights the effect of illite-sudoite alteration within a single sample  
476 (MC-410-01, 677.9 m), comparing a relatively preserved zone showing the onset of alteration (Fig. 5A) with a  
477 fully altered zone (Fig. 5B). Backscattered electron (BSE) images reveal that in the least altered area, muscovite  
478 retains its characteristic cleavage planes (Fig. 5A), whereas in the most altered area, muscovite has completely lost  
479 its original morphology and is replaced by sudoite  $\pm$  illite. Mixtures of these two phases can be distinguished  
480 through grayscale contrast variations (Fig. 5B). Elemental X-ray maps obtained by EPMA further emphasize these  
481 mineralogical and chemical transformations (Fig. 5C-H). In the least altered zone, muscovite exhibits variable K  
482 ( $K\alpha$ ) intensities, with maximum values in the most preserved domains and progressively decreasing intensities in  
483 areas showing incipient alteration (Fig. 5C). The Rb ( $K\alpha$ ) signal follows a similar pattern, reaching its highest  
484 values in the K-rich zones (Fig. 5E). This decrease in K and Rb intensities correlates with the occurrence of Mg  
485 ( $K\alpha$ )-rich areas associated with sudoite formation along fracture zones (Fig. 5G). In the most altered zone,  
486 muscovite relics (or “ghosts”) are identified by their relatively high K ( $K\alpha$ ) and Rb ( $K\alpha$ ) intensities (Fig. 5D, F),  
487 which are spatially anti-correlated with the Mg ( $K\alpha$ ) signal. The latter reaches its maximum intensity within the  
488 sudoite matrix that surrounds these muscovite remnants (Fig. 5H).



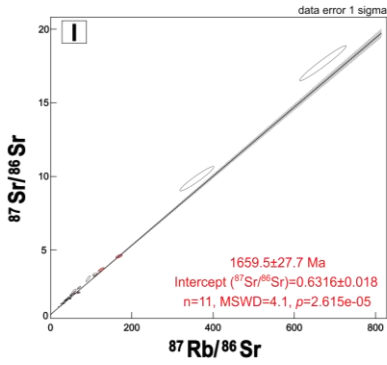
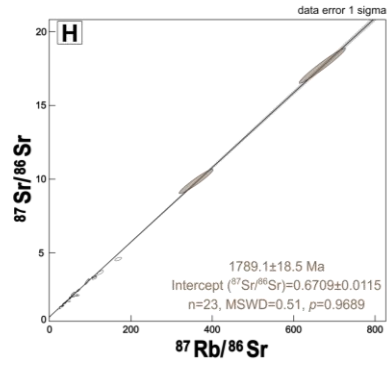
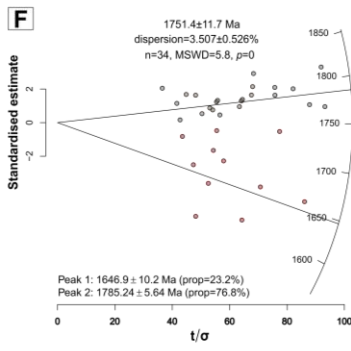
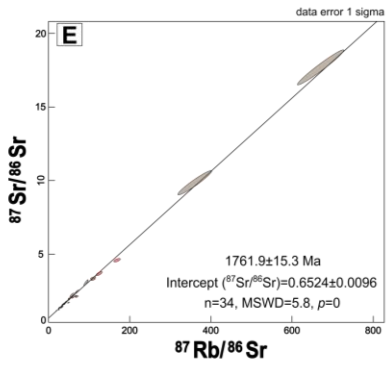
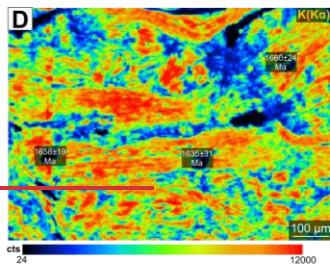
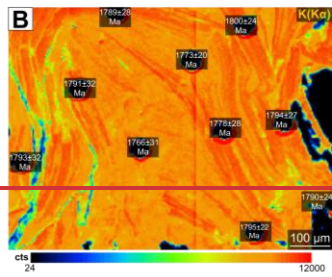
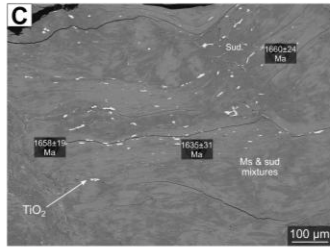
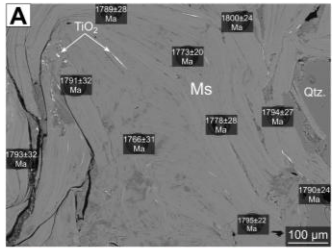


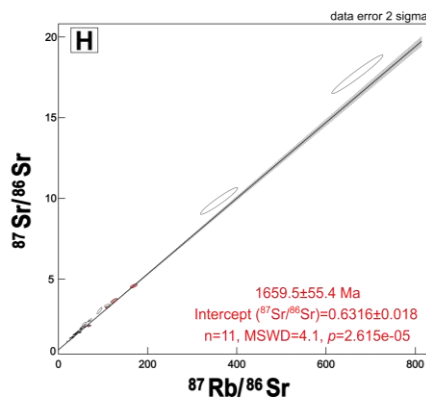
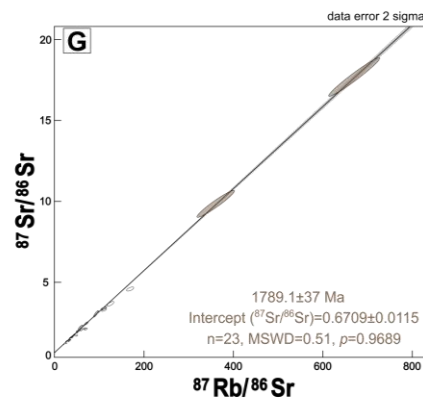
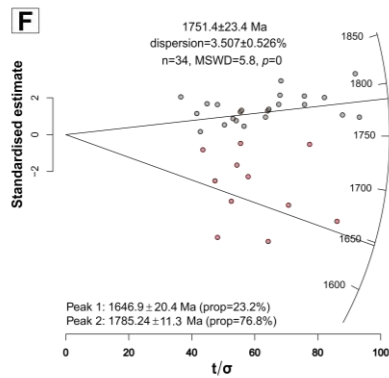
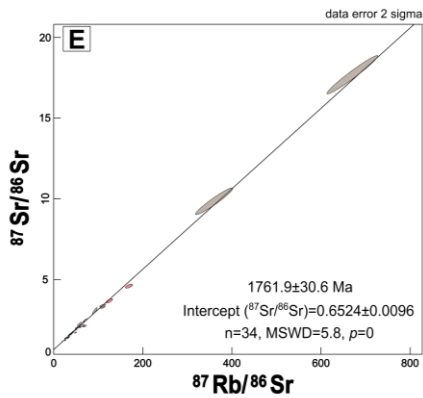
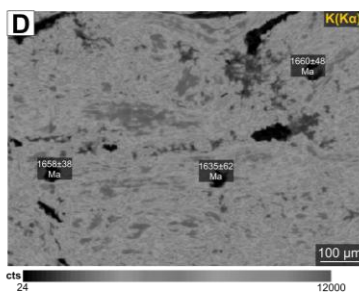
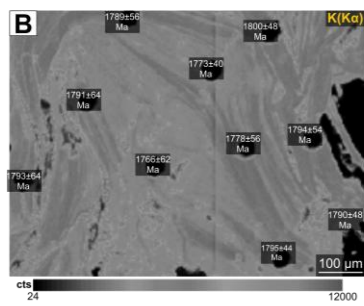
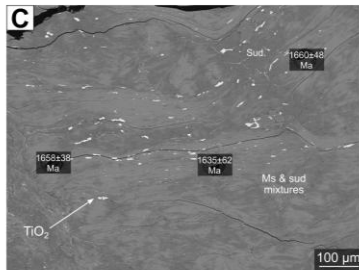
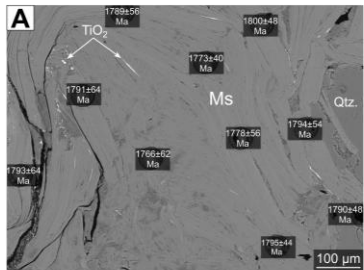
490  
 491 Figure 5. Two zones within the same pelitic gneiss sample [MC-410-01, 677.9 m] are shown, ranging from weakly altered  
 492 (A, C, E, G) to strongly altered by sudoite (B, D, F, H). (A) Preserved to partially preserved metamorphic muscovite  
 493 (Ms<sub>M</sub>) showing the onset of alteration to sudoite along fractures, expressed by darker grey tones. (B) Strongly altered

494 metamorphic muscovite replaced by a sudoite-dominated matrix, containing very fine (<1 μm) TiO<sub>2</sub> exsolution lamellae  
495 that formed from the alteration of muscovite. Circular holes correspond to 50-μm-diameter laser ablation pits. (C-D)  
496 X-ray elemental maps of K (Kα) for (A) and (B), respectively. (C) Gradual decrease in apparent K concentration from  
497 the fully preserved zone toward the incipiently altered domain. (D) K-enriched “ghosts” of muscovite, whereas altered  
498 zones are strongly to entirely depleted in K. (E-F) X-ray elemental maps of Rb (Kα) acquired by EPMA for (A) and (B),  
499 respectively. Apparent Rb concentration is higher in the most preserved zones in (E) and within muscovite ghosts in (D)  
500 compared with illite-sudoite zones. (G-H) X-ray elemental maps of Mg (Kα) acquired by EPMA for (A) and (B),  
501 respectively. (G) Zones filled with sudoite are highlighted by high apparent Mg concentrations. (H) Apparent Mg  
502 concentration is maximal in sudoite-rich areas and anticorrelated with the K distribution shown in (D).

#### 503 4.4. In situ Rb–Sr geochronology

504 Rb–Sr isotopic analyses were performed on metamorphic and early hydrothermal muscovite sampled from both  
505 unaltered and illite-sudoite-altered zones, and from the two investigated lithologies- (Supplement Table S1). To  
506 assess the impact of the illite-sudoite alteration on the isotopic systematics of basement minerals, a representative  
507 sample of a pelitic gneiss (MC-410-01, at a depth of 677.9 m) containing both well-preserved (Fig. 6A, B) and  
508 partially preserved to altered muscovite grains (Fig. 6C, D) was selected for detailed *in situ* analysis by LA-ICP-  
509 MS/MS. The complete Rb–Sr dataset obtained from this sample defines a Rb–Sr regression corresponding to a  
510 date of  $1761.9 \pm 15.330.6$  Ma ( $n = 34$ , MSWD = 5.8,  $p \approx 0$ ,  $\pm 2\sigma$  internal;  $\pm 41.6$  Ma including external  
511 reproducibility), with  $^{87}\text{Rb}/^{86}\text{Sr}$  ratios ranging from 19.62 to 670.44 and a corresponding  $^{87}\text{Sr}/^{86}\text{Sr}$  intercept of  
512  $0.6524 \pm 0.0096$  (Fig. 6E). The elevated MSWD value and the null probability associated with the reduced  $\chi^2$  test  
513 indicate significant excess scatter in the isotopic data, consistent with heterogeneous isotopic behavior at the grain  
514 scale. Given this dispersion, Rb–Sr single-spot dates were calculated for each laser ablation point following the  
515 approach of Rösler and Zack (2022), allowing for a direct comparison between isotopic data, petrographic  
516 observations, and elemental mapping. The resulting single-spot dates display a systematic relationship with K (Kα)  
517 intensity maps, showing a decrease in apparent dates with decreasing K intensity, consistent with the progressive  
518 alteration of muscovite (Fig. 6B, D). Radial plots illustrating the distribution of single-spot dates and isotopic ratios  
519 (Galbraith, 1988, 1990; Rösler and Zack, 2022) reveal two statistically distinguishable populations with partial  
520 overlap: a dominant population at  $1785.2 \pm 5.611.2$  Ma (76.8%), corresponding predominantly to the least altered  
521 muscovite domains, and a younger population at  $1646.9 \pm 10.220.4$  Ma (23.2%), associated with increasingly  
522 altered domains (Fig. 6F). When plotted separately on Rb–Sr regression diagrams, analyses from the least altered  
523 muscovite domains yield a statistically robust regression corresponding to a date of  $1789.1 \pm 18.537$  Ma ( $n = 23$ ,  
524 MSWD = 0.51,  $p = 0.9689$ ,  $\pm 2\sigma$  internal;  $\pm 47$  Ma including external reproducibility), with a  $^{87}\text{Sr}/^{86}\text{Sr}$  intercept  
525 of  $0.6709 \pm 0.0115$  (Fig. 6H). In contrast, analyses from the more altered and mixed domains define a less  
526 statistically reliable regression at  $1659.5 \pm 27.755.4$  Ma ( $n = 11$ , MSWD = 4.1,  $p = 2.6 \times 10^{-5}$ ,  $\pm 2\sigma$  internal;  $\pm 61$  Ma  
527 including external reproducibility), associated with a  $^{87}\text{Sr}/^{86}\text{Sr}$  intercept of  $0.6316 \pm 0.018$  (Fig. 6G). The elevated  
528 MSWD values obtained for the altered domains again indicate substantial isotopic scatter. On the basis of these  
529 observations and the coexistence of mixed isotopic populations within a single sample, the analytical approach  
530 applied to the entire dataset, supported by petrographic and microstructural evidence, consisted of distinguishing  
531 the most preserved metamorphic and early hydrothermal muscovite from those more strongly altered by an illite-  
532 sudoite clay assemblage, in order to constrain the crystallization dates of these two muscovite types and the  
533 potential timing(s) of alteration (Fig. 7A-E).





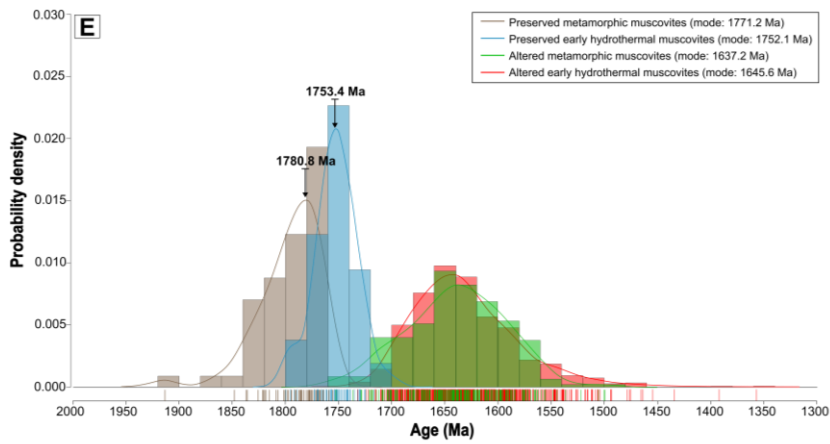
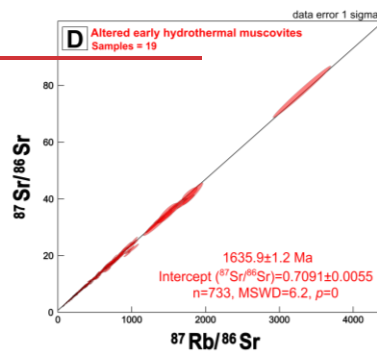
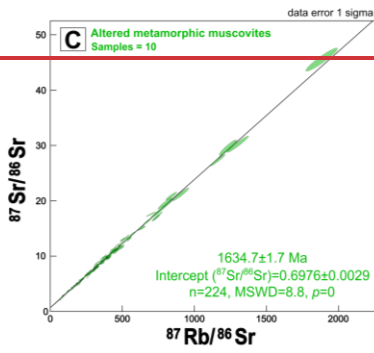
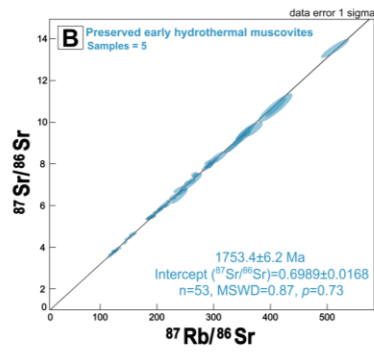
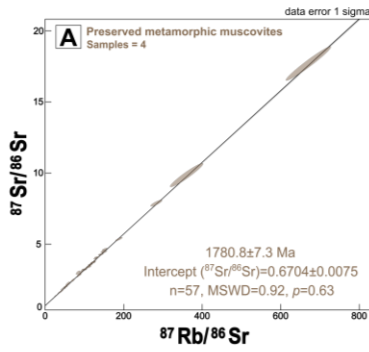
536 Figure 6. (A-D) BSE images and corresponding X-ray elemental maps of K ( $K\alpha$ ) acquired by EPMA for the pelitic gneiss sample [MC-  
537 410-01, 677.9 m] shown in Fig. 5, displaying the calculated Rb–Sr single-spot dates (Rösel and Zack, 2022) for each ablation pit. (A-  
538 B) The calculated Rb–Sr single-spot dates decrease toward zones exhibiting reduced apparent K concentrations. (C-D) The calculated  
539 Rb–Sr single-spot dates are significantly younger in domains fully altered to sudoite compared to those in (A) and (B), which  
540 correspond to preserved to partially preserved zones. (E) Muscovite Rb–Sr isochrons for the sample [MC-410-01, 677.9 m] obtained  
541 from both preserved and altered areas. (F) Radial plot showing the dispersion of isotopic ratios and calculated single-spot dates in  
542 preserved and altered domains (Galbraith, 1988, 1990; Rösel and Zack, 2022), revealing two main populations. (G) Muscovite Rb–Sr  
543 isochrons for preserved domains of the sample [MC-410-01, 677.9 m]. (H) Muscovite Rb–Sr isochrons for altered domains of the same  
544 sample. Brown symbols correspond to preserved muscovite, and red symbols correspond to partially to completely altered muscovite.  
545 All errors are reported at  $\pm 2\sigma$ .

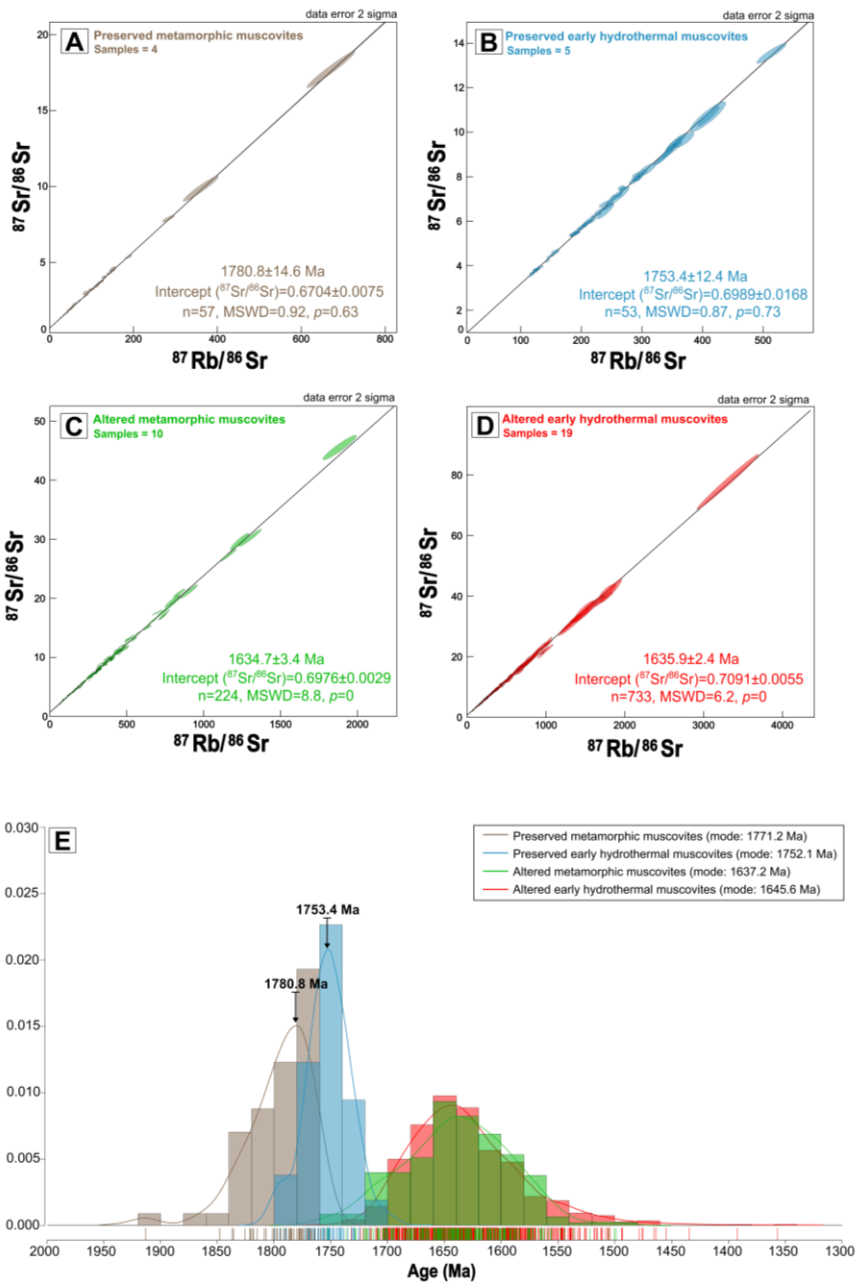
#### 546 4.4.1. Rb–Sr dating of metamorphic muscovite

547 The weighted mean of the Rb–Sr data obtained from all preserved metamorphic muscovite grains (four samples)  
548 defines a composite Rb–Sr regression at  $1780.8 \pm 7.3$  14.6 Ma ( $n = 57$ , MSWD = 0.92,  $p = 0.63$ ,  $\pm 2\sigma$  internal:  
549  $\pm 32$  Ma including external reproducibility), associated with a  $^{87}\text{Sr}/^{86}\text{Sr}$  intercept of  $0.6704 \pm 0.0075$  and overall  
550  $^{87}\text{Rb}/^{86}\text{Sr}$  ratios ranging from 19 to 671 (Fig. 7A). Rb–Sr single-spot dates for preserved metamorphic muscovite  
551 were calculated using a fixed  $^{87}\text{Sr}/^{86}\text{Sr}$  reference value of 0.6704, corresponding to the intercept of the composite  
552 regression. This value is used here as an operational reference parameter; owing to its low magnitude, reasonable  
553 variations in this parameter exert only a minor influence on the calculated dates, as previously demonstrated by  
554 Rösel and Zack (2022). The resulting single-spot dates range from  $1760 \pm 15$  30 Ma to  $1914 \pm 44$  88 Ma and define  
555 a single statistically coherent population with a modal value of 1771.2 Ma (Fig. 7E). Matrix-corrected elemental  
556 concentrations (using an applied correction factor of 0.532038) range from 33 to 145 ppm (average: 81 ppm) for  
557  $^{87}\text{Rb}$ , from 0.19 to 2.46 ppm (average: 1.03 ppm) for  $^{86}\text{Sr}$ , and from 1.28 to 4.50 ppm (average: 2.73 ppm) for  $^{87}\text{Sr}$ .

#### 558 4.4.2. Rb–Sr dating of early hydrothermal muscovite

559 The weighted mean of the Rb–Sr data obtained from preserved early hydrothermal muscovite (five samples)  
560 defines a composite regression at  $1753.4 \pm 6.2$  12.4 Ma ( $n = 53$ , MSWD = 0.87,  $p = 0.73$ ,  $\pm 2\sigma$  internal:  $\pm 31$  Ma  
561 including external reproducibility), associated with a  $^{87}\text{Sr}/^{86}\text{Sr}$  intercept of  $0.6989 \pm 0.0168$  and overall  $^{87}\text{Rb}/^{86}\text{Sr}$   
562 ratios ranging from 34 to 514 (Fig. 7B). Rb–Sr single-spot dates for preserved early hydrothermal muscovite were  
563 calculated using the same fixed  $^{87}\text{Sr}/^{86}\text{Sr}$  reference value of 0.6704, which has a negligible influence on the  
564 resulting dates (e.g., Rösel and Zack, 2022). The calculated single-spot dates span from  $1701.9 \pm 28.8$  57.6 Ma to  
565  $1799.5 \pm 21.4$  42.8 Ma and cluster into a single statistically consistent population with a modal value of 1752.1 Ma  
566 (Fig. 7E). Matrix-corrected elemental concentrations (using an applied correction factor of 0.532038) range from  
567 60.5 to 144.7 ppm (average: 111.3 ppm) for  $^{87}\text{Rb}$ , from 0.22 to 2.26 ppm (average: 0.55 ppm) for  $^{86}\text{Sr}$ , and from  
568 1.82 to 3.97 ppm (average: 3.15 ppm) for  $^{87}\text{Sr}$ .





570

571 Figure 7. (A) Rb-Sr isochrons for metamorphic muscovite preserved from illite-sudoite alteration, represented by four samples. (B)  
 572 Rb-Sr isochrons for early hydrothermal muscovite preserved from illite-sudoite alteration, represented by five samples. (C) Rb-Sr

573 isochrons for metamorphic muscovite affected by illite-sudoite alteration, represented by ten samples. (D) Rb—Sr isochrons for early  
574 hydrothermal muscovite affected by illite-sudoite alteration, represented by nineteen samples. (E) Density diagram constructed from  
575 individual single-spot dates obtained for preserved metamorphic muscovite (brown), preserved early hydrothermal muscovite (blue),  
576 illite-sudoite altered metamorphic muscovite (dark red), and illite-sudoite altered early hydrothermal muscovite (red). A bin width of  
577 20 Ma was used for the histogram. The isochron dates calculated in (A) and (B) are indicated by bold arrows for the preserved  
578 metamorphic and early hydrothermal muscovite.

#### 579 4.4.3. Rb—Sr dating of altered muscovites

580 The weighted mean of the dates obtained for the metamorphic muscovite affected by illite-sudoite hydrothermal  
581 alteration defines regressions at  $1634.7 \pm 1.7$  ca. 1635 Ma for metamorphic muscovite (ten samples,  $n = 224$ ,  
582  $MSWD = 8.8$ ,  $p = 0$ ,  $\pm 2\sigma$  internal;  $\pm 26$  Ma including external reproducibility) and at  $1635.9 \pm 1.2$  ca. 1636 Ma  
583 for early hydrothermal muscovite (nineteen samples,  $n = 733$ ,  $MSWD = 6.2$ ,  $p = 0$ ,  $\pm 2\sigma$  internal;  $\pm 26$  Ma  
584 including external reproducibility), associated with  $^{87}\text{Sr}/^{86}\text{Sr}$  intercepts of  $0.6976 \pm 0.0029$  and  $0.7091 \pm 0.0055$ ,  
585 respectively (Fig. 7C, D). The elevated MSWD values and null probabilities indicate significant excess scatter in  
586 both datasets for both muscovite types. Single-spot Rb—Sr dates obtained from altered muscovite display a broad  
587 and erratic distribution, ranging from  $1498.6 \pm 11.4$  ca. 1499 Ma to  $1756.2 \pm 22.9$  ca. 1757 Ma (modal value of 1637.2 Ma)  
588 for metamorphic muscovite, and from  $1357.0 \pm 32.4$  ca. 1358 Ma to  $1735.1 \pm 21.9$  ca. 1736 Ma (modal value of 1645.6 Ma)  
589 for early hydrothermal muscovite (Fig. 7E). Matrix-effect-corrected concentrations (using and applied correction  
590 factor of 0.532038) for the metamorphic muscovite range from 21.7 to 213.6 ppm (mean: 99.9 ppm) for  $^{87}\text{Rb}$ , from  
591 0.10 to 3.74 ppm (mean: 0.62 ppm) for  $^{86}\text{Sr}$ , and from 0.9 to 5.8 ppm (mean: 2.76 ppm) for  $^{87}\text{Sr}$ . Matrix-effect-  
592 corrected concentrations for the early hydrothermal muscovite range from 9.18 to 3222.9 ppm (mean: 190.4 ppm)  
593 for  $^{87}\text{Rb}$ , from 0.05 to 15.8 ppm (mean: 0.82 ppm) for  $^{86}\text{Sr}$ , and from 0.44 to 75.4 ppm (mean: 4.95 ppm) for  $^{87}\text{Sr}$ .

594 The analysis of calculated single-spot Rb—Sr dates as a function of uncertainty quartiles reveals an overall  
595 homogeneous distribution, with moderate variations in central values and dispersion across uncertainty levels (Fig.  
596 8A). The dataset was divided into four groups corresponding to the uncertainty quartiles (Q0—Q25, Q25—Q50,  
597 Q50—Q75, and Q75—Q100). The group with the lowest uncertainty (Q0—Q25) comprises 241 observations,  
598 yielding a mean date of 1633.3 Ma ( $\sigma = 45.3$  Ma). The second quartile (Q25—Q50) includes 239 samples, with a  
599 mean date of 1630.7 Ma ( $\sigma = 44$  Ma). In the third quartile (Q50—Q75), the mean remains stable at 1630.6 Ma,  
600 although the standard deviation increases slightly ( $\sigma = 51.5$  Ma), reflecting greater variability. Finally, the quartile  
601 with the highest uncertainty (Q75—Q100) encompasses 239 data points, showing a slightly higher mean date  
602 (1637.2 Ma) and the greatest dispersion ( $\sigma = 53.9$  Ma). Examination of the minimum and maximum values  
603 indicates a gradual broadening of the single-spot Rb—Sr date distribution with increasing uncertainty, ranging  
604 from 1493.8 to 1752.7 Ma in the first quartile to 1357.0 to 1751.5 Ma in the last. This trend suggests that  
605 measurements associated with higher uncertainties encompass a wider range of dates (Fig. 8B). Overall, the  
606 normalized kernel density estimates (KDE) of single-spot date distributions by quartile display relatively similar  
607 patterns, indicating no major bias related to analytical uncertainty, although a slight increase in variability is  
608 observed. This observation highlights that, while individual uncertainties do not significantly affect the mean of  
609 the single-spot dates, they are associated with greater dispersion in the extreme values. To address the  
610 heterogeneous distribution of single-spot dates and the variability of their individual uncertainties, a statistical  
611 approach based on a Gaussian Mixture Model (GMM) was applied (McLachlan and Peel, 2000; Melnykov and  
612 Melnykov, 2012; Glodek et al., 2013; Nguyen and McLachlan, 2015; McLachlan et al., 2019). The GMM, applied

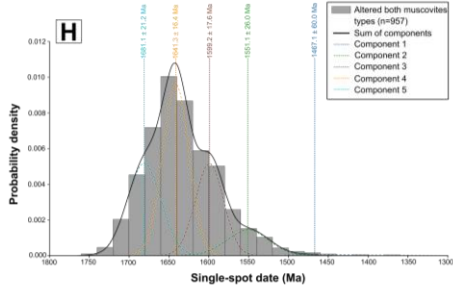
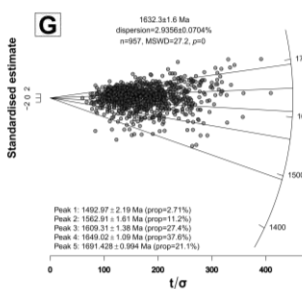
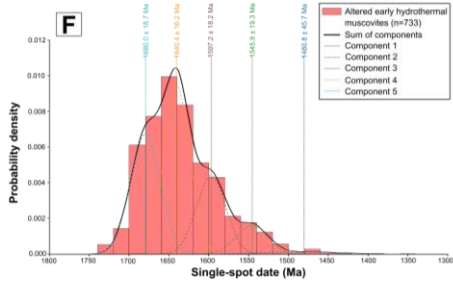
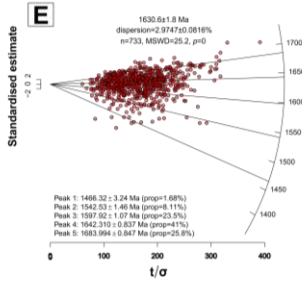
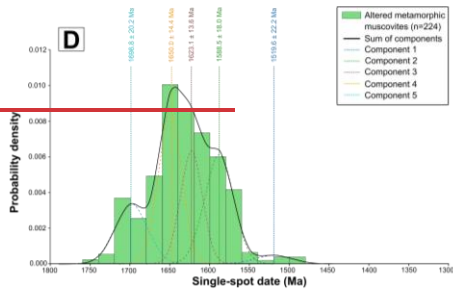
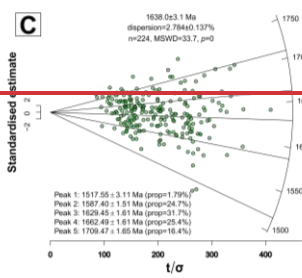
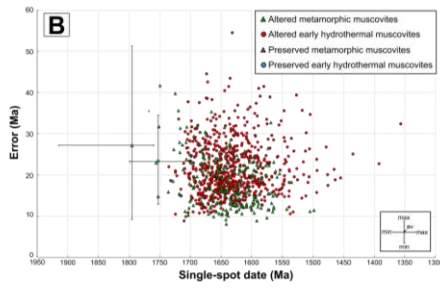
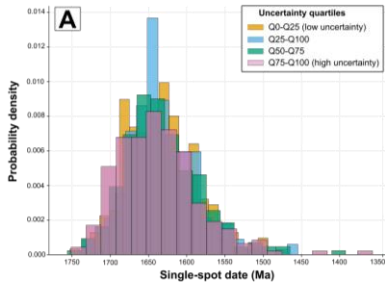
a mis en forme : Français (France)

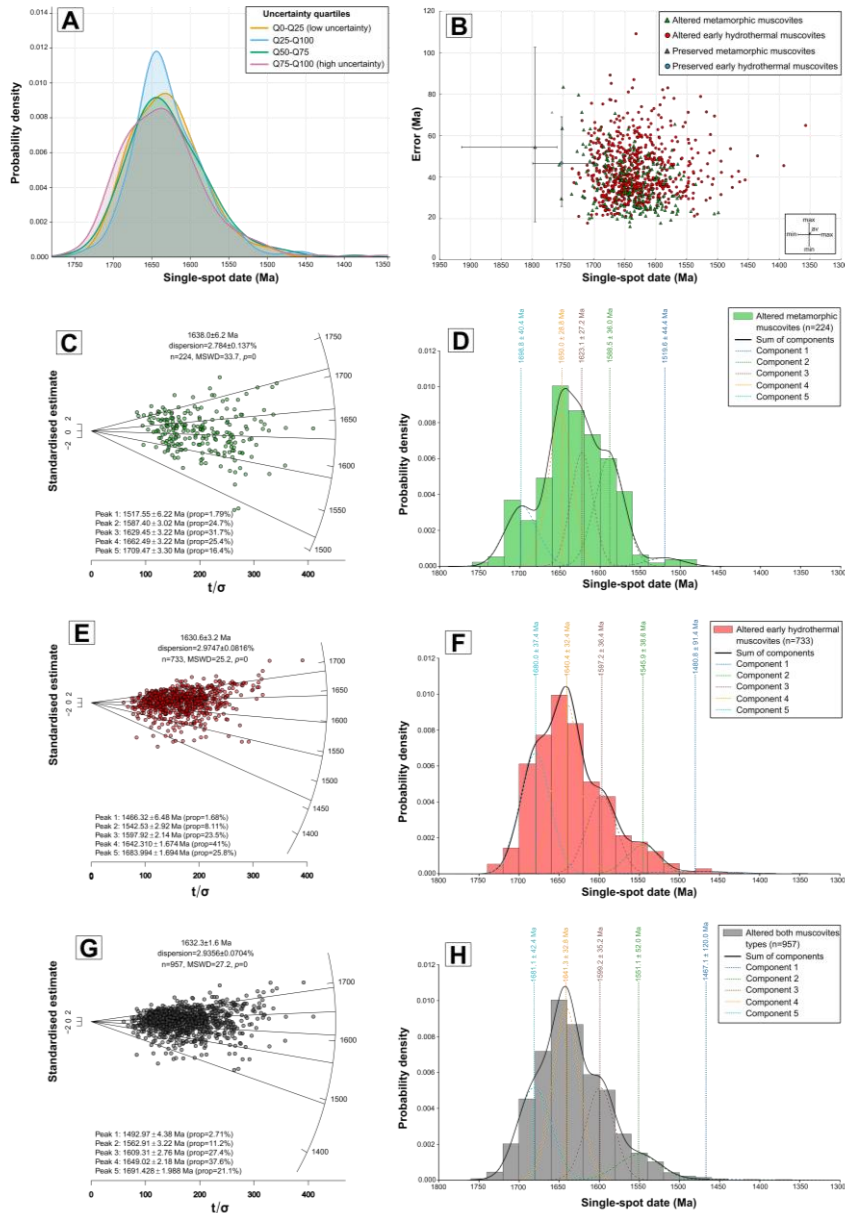
a mis en forme : Français (France)

a mis en forme : Français (France)

a mis en forme : Français (France)

613 to the logarithmically transformed Rb–Sr single-spot dates of both muscovite types, enables the decomposition  
614 of the overall dataset into multiple components characterized by distinct probabilistic centers. A suite of GMMs  
615 with varying numbers of Gaussian components was evaluated, with model performance assessed using the  
616 Bayesian Information Criterion (BIC), which balances goodness of fit against model complexity. Although  
617 solutions with different numbers of components were obtained, the five-component model emerged most  
618 consistently across repeated runs and is therefore presented here. This configuration is compatible with the number  
619 of populations identified from IsoplotR radial plots (Galbraith, 1988, 1990), providing a coherent basis for  
620 methodological comparison. The GMM-derived components were subsequently examined in relation to the  
621 statistically coherent clusters defined by the radial plot approach, which explicitly accounts for individual  
622 analytical uncertainties. Statistical analyses conducted on the hydrothermally altered muscovite show good overall  
623 consistency between the date clusters identified by the radial plots (IsoplotR) and those inferred from the GMM.  
624 For altered metamorphic muscovite, the radial plot reveals five statistical groupings (Fig. 8C):  $1517.6 \pm 3.16.2$  Ma  
625 (1.8 % of analyses),  $1587.4 \pm 1.53.0$  Ma (24.7 %),  $1629.5 \pm 1.63.2$  Ma (31.7 %),  $1662.5 \pm 1.63.2$  Ma (25.4 %),  
626 and  $1709.5 \pm 1.73.4$  Ma (16.4 %). The corresponding GMM also distinguishes multiple components, including a  
627 dominant one at  $1650.0 \pm 14.428.8$  Ma (33.3 %), and secondary components at  $1698.8 \pm 20.240.4$  Ma (18.9 %),  
628  $1623.1 \pm 13.627.2$  Ma (24.5 %),  $1585.5 \pm 1836.0$  Ma (21.0 %), and  $1519.6 \pm 22.244.4$  Ma (2.4 %) (Fig. 8D). For  
629 altered early hydrothermal muscovite, the radial plot identifies five statistical clusters (Fig. 8E):  $1466.3 \pm 3.26.4$   
630 Ma (1.7 % of analyses),  $1542.5 \pm 1.53.0$  Ma (8.1 %),  $1597.9 \pm 1.12.2$  Ma (23.5 %),  $1642.3 \pm 0.81.6$  Ma (41 %),  
631 and  $1684.0 \pm 0.81.6$  Ma (25.8 %). The corresponding GMM also resolves several components, including a main  
632 one at  $1640.4 \pm 16.232.4$  Ma (38.4 %), and secondary components at  $1680.0 \pm 18.737.4$  Ma (31.7 %),  $1597.2 \pm$   
633  $18.236.4$  Ma (19.7 %),  $1545.9 \pm 19.338.6$  Ma (8.1 %), and  $1480.8 \pm 45.791.4$  Ma (1.8 %) (Fig. 8F). When  
634 combining the results for illite-sudoite zones of both muscovite types, the radial plot identifies five statistical  
635 clusters (Fig. 8G):  $1493.0 \pm 2.24.4$  Ma (2.7 % of analyses),  $1562.9 \pm 1.63.2$  Ma (11.2 %),  $1609.3 \pm 1.42.8$  Ma  
636 (27.4 %),  $1649.0 \pm 1.12.2$  Ma (37.6 %), and  $1691.4 \pm 1.2.0$  Ma (21.1 %). The corresponding GMM also  
637 distinguishes several components, including a dominant one at  $1641 \pm 16.432.8$  Ma (37.6 %), and secondary  
638 components at  $1681.1 \pm 21.242.4$  Ma (28.2 %),  $1599.2 \pm 17.635.2$  Ma (23.7 %),  $1551 \pm 2652$  Ma (9.6 %), and  
639  $1467 \pm 60120$  Ma (0.9 %) (Fig. 8H).





641

642 Figure 8. (A) Probability Kernel density histogram estimates (KDE) of calculated Rb-Sr single-spot dates for metamorphic and  
 643 hydrothermal muscovite affected by illite-sudoite alteration, sorted according to the quartiles of individual analytical uncertainties.  
 644 The shape of the single-spot date distributions varies slightly with uncertainty level. Low uncertainties correspond to tightly clustered  
 645 and homogeneous Rb-Sr single-spot dates, whereas high uncertainties are associated with greater dispersion and more pronounced  
 646 asymmetry. (B) Scatter plot of analytical uncertainties versus Rb-Sr single-spot dates for altered metamorphic and early

647 hydrothermal muscovite. For the preserved metamorphic and early hydrothermal muscovites, the mean values of single-spot Rb–Sr  
648 dates and their associated analytical uncertainties are reported, together with their respective maximum and minimum values. (C)  
649 Radial plot illustrating the dispersion of isotopic ratios and calculated single-spot dates for altered metamorphic muscovite. Five  
650 statistical populations are identified in the radial plot. (D) Gaussian mixture model (GMM) applied to log-transformed dates,  
651 representing the distribution of Rb–Sr single-spot dates of altered metamorphic muscovite, weighted by their uncertainties, together  
652 with the five components identified by the GMM. (E) Radial plot showing the dispersion of isotopic ratios and calculated single-spot  
653 dates for altered early hydrothermal muscovite. Five statistical populations are identified. (F) Gaussian mixture model applied to log-  
654 transformed dates representing the distribution of Rb–Sr single-spot dates for altered early hydrothermal muscovite, weighted by  
655 uncertainties, together with the five components identified by the GMM. (G) Radial plot showing the dispersion of isotopic ratios and  
656 calculated single-spot dates for altered metamorphic and early hydrothermal muscovite combined. Five statistical populations are  
657 identified. (H) Gaussian mixture model applied to log-transformed dates representing the distribution of combined altered  
658 metamorphic and early hydrothermal muscovite Rb–Sr single-spot dates, weighted by uncertainties, as well as the five components  
659 identified by the GMM. The components identified by the GMM closely correspond to the statistical populations defined by the radial  
660 plots, taking into account the associated uncertainties. A bin width of 20 Ma was used for each GMM, consistent with the average of  
661 the individual analytical uncertainties calculated for each spot.

## 662 5. Discussion

### 663 5.1. Behavior of Rb and Sr and related Rb/Sr isotopic systems in muscovite from basement lithologies 664 affected by post-crystallization hydrothermalism

665 The study of basement lithologies along a gradient from non-hydrothermally altered to strongly hydrothermally  
666 altered zones beneath unconformity-type uranium deposits has revealed significant mineralogical, geochemical,  
667 and isotopic modifications. Across the four investigated sites, this alteration, macroscopically characterized by an  
668 apple-green color affecting the foliation planes of metapelitic gneisses, leucosomes, and granitoids, as well as  
669 filling fractures crosscutting the host lithologies (Figs. 2C, D, E, F and 4), manifests microscopically as the  
670 progressive replacement of primary and retro-metamorphic minerals (plagioclase, K-feldspars, muscovite, biotite,  
671 Fe-Mg chlorite) by an assemblage of illite and sudoite. Textural evidence suggests that these two minerals  
672 crystallized synchronously or nearly synchronously (Pacquet and Weber, 1993; Percival and Kodama, 1989). This  
673 alteration induces pronounced mineralogical transformations in both metamorphic and early hydrothermal  
674 muscovite, involving a partial to complete breakdown of their crystal structure. This process is expressed either as  
675 illitization initiated along the cleavage planes of muscovite, synchronous or quasi-synchronous with sudoite  
676 precipitation, or as massive sudoite crystallization enveloping muscovite relics (Figs. 4 and 5B–8). Illite-sudoite  
677 alteration constitutes the most pervasive and intense hydrothermal alteration affecting both the Athabasca Basin  
678 sandstones and the underlying basement in the vicinity of unconformity-related uranium mineralization, and has  
679 long been recognized as a robust exploration vector for U deposits (e.g., Carl et al., 1992; Derome et al., 2005;  
680 Cloutier et al., 2009; Ng et al., 2013; Martz, 2017; Kaczowka, 2021; Powell et al., 2022). This alteration is  
681 associated with a loss of Al, Na, K and Sr and a gain in Mg, Li and B (Martz et al., 2019a). The loss of K, Na, Al  
682 and Sr is easily explained by the K-feldspars and plagioclases replacement by illite plus sudoite. ~~Part~~Some of these  
683 elements ~~remains~~remain in the system and ~~is~~are in situ transferred to the newly-formed clays, whereas the rest  
684 ~~leaves~~leave the system. This process results from the circulation of marine-derived basinal brines, generated during  
685 early to middle diagenesis of the sedimentary basin (Hoeve and Sibbald, 1978; Kotzer and Kyser, 1995; Kyser et  
686 al., 2000).

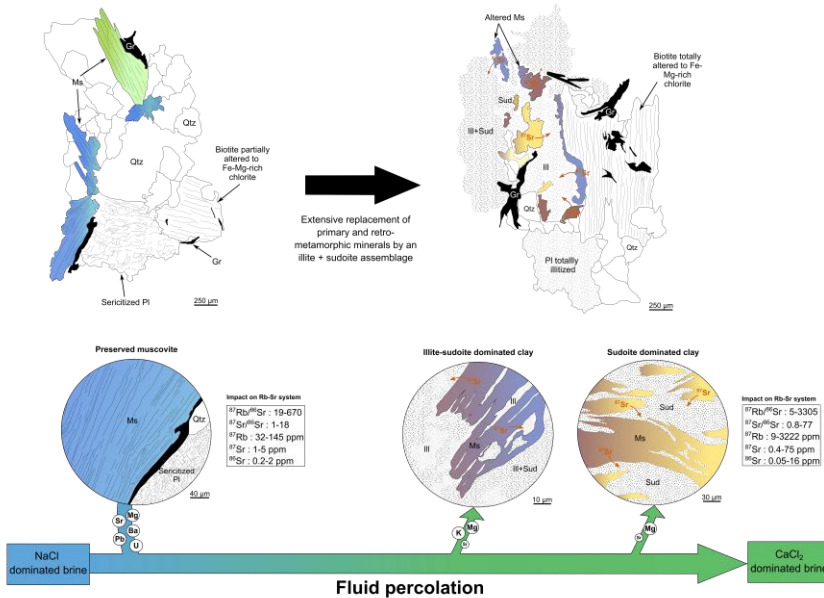
a mis en forme : Police :Non Italique

687 This illite + sudoite assemblage formed at temperatures between 150 and 220 °C, under pressures corresponding  
688 approximately to the base of the sedimentary basin (ca. ~~0.1–0.3 kbar~~**GPa**) (Halter, 1988; Kotzer and Kyser, 1995;  
689 Cloutier et al., 2009; Martz, 2017). It is associated with important chemical modifications of the host rocks, notably  
690 the loss of K, Na, Al, and Sr due to destabilization of primary feldspars and micas, and the concomitant gain in  
691 Mg, Li, B, and Ca reflecting the composition of the basinal brine and its prolonged interaction with silicates. The  
692 observed B and Mg enrichments are attributed to the intrinsic composition of the basinal fluid (Mercadier et al.,  
693 2012; Richard et al., 2011) rather than to a local metamorphic source. Variations in the illite/sudoite ratio reflect  
694 changes in thermal gradient (Beaufort et al., 2005; Kotzer and Kyser, 1995; Martz, 2017), in fluid composition  
695 (Cloutier et al., 2009), notably the  $K^+/Mg^{2+}$  ratio, as well as in host rock lithology (Bruneton, 1993; Pacquet and  
696 Weber, 1993; Mercadier et al., 2012; ~~Cuney and Kyser and Cuney~~, 2015; Martz, 2017) and system pH (Kyser et  
697 al., 2000; Kister et al., 2005; Mercadier et al., 2012; Martz, 2017). The illite-sudoite alteration is not related to the  
698 recrystallization of new generations of metamorphic or early hydrothermal muscovite but instead results from fluid  
699 circulation that induces mineralogical, geochemical, and isotopic modifications. Isotopically, progressive  
700 alteration leads to systematic variations in Rb–Sr systematics, as mineralogical transformations modify both  
701 elemental concentrations and isotopic ratios. The ~~range of~~  $^{87}Rb/^{86}Sr$  ratios ~~increase~~**broadens** from 20–670 to 5–  
702 3305, while  $^{87}Sr/^{86}Sr$  ratios shift from 1.18 to 1.78, with corresponding single-spot dates decreasing from 1701.9–  
703 1914.8 to 1357.0–1756.2 Ma (Fig. 9). ~~According to Dodson (1973), the loss~~**The behaviour of radiogenic  $^{87}Sr$**   
704 ~~controls the Rb–Sr geochronometer. In the presence of fluid-rock interaction is best understood in terms of fluid-~~  
705 ~~mediated recrystallization and open-system isotopic exchange, rather than purely thermally-activated volume~~  
706 ~~diffusion (Villa, 1998; Villa, 2022).~~

707 The observed shift in Rb–Sr systematics is primarily attributed to the partial to complete loss of radiogenic  $^{87}Sr$   
708 from the system in response to fluid circulation associated with illite-sudoite alteration. This process results in  
709 partial to complete resetting of the Rb–Sr isotopic system (Matheny et al., 1990; Kalt et al., 1994; Evans et al.,  
710 1995; Eberlei et al., 2015). Elemental maps further demonstrate that Rb is also mobile; however, the mobility of  
711 radiogenic  $^{87}Sr$  is significantly greater than that of Rb and non-radiogenic Sr. This contrast in mobility accounts  
712 for the observed variations in both Rb/Sr ratios and Sr isotopic compositions (Fig. 5E and F) and could explain the  
713 erratic data distribution. The structural destabilization of metamorphic and early hydrothermal muscovite during  
714 hydrothermal alteration, facilitated by illitization and/or sudoitization along cleavage planes, may have enhanced  
715 diffusion and leaching of radiogenic  ~~$^{87}Sr$~~  **$^{87}Sr$** . This process likely promoted the transfer of  $^{87}Sr$  into clay phases  
716 and/or the fluid phase (Fig. 9). In addition, radiogenic  $^{87}Sr$  produced in situ ~~may occupy transient interlayer or~~  
717 ~~defect-related positions that are crystallochemically unfavorable for a divalent cation, whose ideal coordination~~  
718 ~~environment lies in octahedral sites. This crystallochemical mismatch promotes diffusion of  $^{87}Sr$  out of interfolial~~  
719 ~~domains typically reserved for monovalent LILEs such as  $K^+$  or  $Rb^+$  (e.g., Brigatti and Guggenheim, 2002). The~~  
720 ~~transfer of  $^{87}Sr$  into the fluid phase could account for the Sr contents measured in brines trapped in fluid inclusions~~  
721 ~~(Mercadier et al., 2012; Richard et al., 2011; Martz, 2017). occupies the interlayer (I-site) in muscovite, substituting~~  
722 ~~for monovalent cations such as  $K^+$  or  $Rb^+$  (Brigatti and Guggenheim, 2002), whereas common Sr ( $^{86}Sr$ ,  $^{88}Sr$ ) is~~  
723 ~~predominantly hosted in the octahedral (M-site), where divalent cations are stable. This crystallochemical~~  
724 ~~distinction means that preferential removal of radiogenic  $^{87}Sr$  from the I-site alone would be expected to drive the~~  
725 ~~regression intercept toward chondritic or higher values, not toward the sub-chondritic values observed here. The~~  
726 ~~anomalously low intercept values (~0.67) are therefore better interpreted as the result of isochron rotation under~~

727 [open-system conditions involving non-conservative, grain-scale redistribution of both Rb and Sr \(Brooks et al.,](#)  
 728 [1976; Villa, 1998; Villa, 2022\)](#), rather than as a direct consequence of selective I-site  $^{87}\text{Sr}$  loss. As demonstrated  
 729 [by Villa \(1998, 2022\)](#), fluid-mediated recrystallization operates orders of magnitude faster than thermally-activated  
 730 [volume diffusion and represents the dominant mechanism of isotopic exchange in micas affected by hydrothermal](#)  
 731 [fluids. In this framework, the structural destabilization of muscovite along cleavage planes during illitization and](#)  
 732 [sудоitization, facilitated by the circulating Ca-Cl<sub>2</sub>-dominated brines, promoted fluid-assisted dissolution-](#)  
 733 [reprecipitation and non-conservative redistribution of Rb and Sr at the grain scale, consistent with the](#)  
 734 [hydrochronological framework described by Villa \(2022\). The transfer of Sr into the fluid phase is independently](#)  
 735 [supported by Sr enrichment documented in fluid inclusions from the Athabasca Basin brines \(Mercadier et al.,](#)  
 736 [2012; Richard et al., 2011; Martz, 2017\).](#)

737 Furthermore, the measured isotopic ratios  $^{87}\text{Rb}/^{86}\text{Sr}$  and  $^{87}\text{Sr}/^{86}\text{Sr}$ , as well as  $^{87}\text{Rb}$  and  $^{87}\text{Sr}$  concentrations, are  
 738 significantly higher in altered muscovites than in unaltered muscovites. The simultaneous increase in  $^{87}\text{Rb}/^{86}\text{Sr}$   
 739 and  $^{87}\text{Sr}/^{86}\text{Sr}$  ratios in muscovites affected by alteration or fluid circulation reflects reopening of the Rb–Sr system  
 740 and selective mass redistribution of Sr during the hydrothermal event. Glodny and Grauert (2009) and Eberlei et  
 741 al. (2015) demonstrated that such concurrent increases do not require mica recrystallization but rather result from  
 742 a combination of dynamic fluid-rock interaction processes. These include: (i) a net loss of Sr through accelerated  
 743 diffusion along defects (microfractures, cleavage planes, subgrains, dislocations), favoring the preferential loss of  
 744 radiogenic Sr from transient interlayer sites or defect-related positions in muscovite; (ii) a decrease in the molar  
 745 fraction of Sr, which automatically increases the  $^{87}\text{Rb}/^{86}\text{Sr}$  ratio since Rb is relatively immobile; and (iii) a minor  
 746 incorporation of Sr, possibly more radiogenic, from the matrix reservoir or from the fluid (e.g., derived from  
 747 feldspar alteration) into altered muscovite, which can slightly increase the measured  $^{87}\text{Sr}/^{86}\text{Sr}$  ratio.



749 Figure 9. Schematic representation of the effect of illite-sudoite alteration on the Rb–Sr geochronometer in basement-hosted muscovite  
750 within the context of unconformity-related uranium deposits, resulting from the percolation of a Ca-Cl-dominated brine and fluid-  
751 rock interaction. This hydrothermal episode induces extensive replacement of primary and retro-metamorphic minerals by an illite-  
752 sudoite clay assemblage whose modal proportions vary among samples. The alteration fluid, which may circulate along pre-existing  
753 pathways generated during retro-metamorphic alteration of primary minerals, disrupts the crystal lattice of muscovite along cleavage  
754 planes. This structural breakdown leads to the loss of radiogenic <sup>87</sup>Sr from muscovite, which is redistributed into the fluid and/or the  
755 newly formed clay phases. Systematic fluid-inclusion studies (e.g., Mercadier et al., 2012; Richard et al., 2011; Martz, 2017) reveal that  
756 the regional brine, initially seawater-derived and NaCl-dominated, became progressively enriched in K, Sr, Mg, and B, and evolved  
757 toward a CaCl-dominated composition through prolonged interaction with the host rocks. This alteration episode also results in  
758 increased Rb/Sr isotopic ratios in muscovite, together with elevated <sup>87</sup>Rb and <sup>87</sup>Sr contents, which may be explained by Sr loss from the  
759 muscovite molar fraction and by minor incorporation of Sr derived from either the rock matrix reservoir or the circulating fluid.

## 760 5.2. Assessing the reliability and applicability of the Rb–Sr system in metamorphic and early 761 hydrothermal muscovite

762 The characterization of well-preserved micro-domains enabled the acquisition of statistically robust isotopic ages  
763 for both the metamorphic muscovite associated with the foliation of metapelitic gneisses and the early  
764 hydrothermal muscovite from anatectic granitoids or occurring in the leucosomes of metapelitic gneisses. These  
765 muscovite grains preserved from illite-sudoite alteration define well-correlated Rb–Sr regressions yielding dates  
766 of  $1780.8 \pm 7.3$  Ma and  $1753.4 \pm 6.2$  Ma, respectively (Fig. 7A, B). Sr regressions yielding dates of  $1780.8 \pm 14.6$   
767 Ma ( $2\sigma$  internal;  $\pm 32$  Ma including external reproducibility) and  $1753.4 \pm 12.4$  Ma ( $2\sigma$  internal;  $\pm 31$  Ma including  
768 external reproducibility), respectively (Fig. 7A, B). It should be noted that in open-system Rb–Sr behaviour, fluid-  
769 rock interaction can rotate an originally valid isochron through non-conservative redistribution of Rb and Sr at the  
770 grain scale, yielding geologically meaningful slopes but mathematically anomalous intercepts that fall below  
771 physically feasible initial <sup>87</sup>Sr/<sup>86</sup>Sr values (Brooks et al., 1976; Villa, 1998; Villa, 2022). As demonstrated by Villa  
772 (1998, 2022), the isotopic perturbations formerly attributed to thermally-driven volume diffusion in micas have  
773 since been shown to reflect fluid-mediated recrystallization, which operates orders of magnitude faster than pure  
774 Fickian diffusion and represents the dominant mechanism of isotopic exchange in micas affected by hydrothermal  
775 fluids. Such rotation does not invalidate the age information recorded by the slope of the regression. However, the  
776 corresponding regression intercepts ( $0.6704 \pm 0.0075$  and  $0.6989 \pm 0.0168$ ) fall below the minimum <sup>87</sup>Sr/<sup>86</sup>Sr value  
777 of the solar system ( $-0.698$ ) and therefore cannot represent physically meaningful initial isotopic compositions.  
778 These intercepts are thus not interpreted as true initial <sup>87</sup>Sr/<sup>86</sup>Sr ratios but rather as apparent values resulting from  
779 disturbed Rb–Sr systematics. Low MSWD values ( $< 1$ ) and high p-values ( $p \gg 0.05$ ) indicate strong internal  
780 coherence of the datasets, suggesting that the regressions are statistically robust despite their anomalous intercepts.  
781 Such features are characteristic of rotated or disturbed isochrons formed under open-system conditions, in which  
782 Rb and Sr are redistributed in a non-conservative manner (Brooks et al., 1976; Faure and Mensing, 2013; Dickin,  
783 2018). Proportional loss of Rb relative to Sr, selective Sr mobility during fluid-rock interaction, or partial isotopic  
784 resetting during metamorphism may rotate an originally valid isochron, yielding geologically reasonable slopes  
785 but non-physical intercepts (Brooks et al., 1976; DePaolo, 1981; Villa, 1998; Villa, 2022; Faure and Mensing,  
786 2013). The reproducibility of measured <sup>87</sup>Sr/<sup>86</sup>Sr ratios for the NIST SRM 610 reference material, together with  
787 the consistency of the regression intercept obtained for the La Posta biotite reference material, indicates that the  
788 measured <sup>87</sup>Sr/<sup>86</sup>Sr ratios and derived regression intercepts are not attributable to analytical bias or standardization  
789 issues, thereby effectively excluding an analytical or calibration-related origin. Accordingly, the anomalously low  
790 intercept values are interpreted as mathematical artefacts arising from open-system Rb–Sr behavior and isochron

791 rotation under fluid-mediated conditions, rather than as geologically meaningful isotopic signatures or evidence  
792 of an analytical artefact. In contrast, the slopes of the regressions may still record geologically significant timing  
793 information related to muscovite crystallization or partial isotopic resetting, as has been documented in other  
794 disturbed Rb—Sr systems (Brooks et al., 1976; Villa, 1998; Villa, 2022; Zack and Hogmalm, 2016).

795 The single-spot ages obtained from metamorphic muscovite developed along foliation planes in Paleoproterozoic  
796 pelitic gneisses (e.g., Schneider et al., 2007; Skipton et al., 2016; Jeanneret et al., 2017; Martz, 2017) range from  
797  $1914 \pm 44$  Ma to  $1760 \pm 15$  Ma, with a modal value of 1771.2 Ma and an isochroneisochron age of  $1780.8 \pm$   
798  $7.3$ – $14.6$  Ma ( $2\sigma$  internal;  $\pm 32$  Ma including external reproducibility) (Fig. 10). The mean age derived from single-  
799 spot analyses, together with the isochron age, falls within the temporal window of the M2-D2 event, which  
800 generated the northeast-striking structural trend of the WMTZ and formed under a sinistral transpressional tectonic  
801 regime during the late stages of the oblique Hudsonian collision, between ca. 1813 and 1770 Ma (Fig. 10).  
802 Thermobarometric estimates indicate that rocks of the study area were re-equilibrated under conditions of ca. 0.5  
803 kbarGPa and  $750$ – $825$  °C at this time (Annesley et al., 1992, 1997a,b,c, 1999a,b; Jeanneret et al., 2017; Toma et  
804 al., 2024). The M2-D2 temporal interval is supported by geochronological constraints derived from other mineral  
805 phases using various U—Pb chronometers, including monazite (Pb diffusion at ca.  $500$ – $800$  °C; e.g., Cherniak et  
806 al., 2004; McFarlane and Harrison, 2006), zircon ( $>900$  °C; Cherniak and Watson, 2001), and titanite ( $500$ – $800$   
807 °C; Kohn, 2017). The distribution of Rb—Sr single-spot ages in metamorphic muscovite is shifted toward the  
808 lower limit of this time window (Fig. 10) and reflects the neoformation of muscovite along the retrograde P-T path  
809 ( $\leq \sim 700$  °C), possibly in the presence of fluids and the cooling of muscovite below the closure temperature of the  
810 Rb—Sr system, estimated at ca.  $450$ – $600$  °C (Dodson, 1973). Above this closure temperature, Sr diffusion  
811 remained sufficiently rapid to maintain an open isotopic system, allowing equilibration with the surrounding matrix  
812 or between minerals.

813 In contrast, the single-spot ages measured in early hydrothermal muscovite crystallized within anatectic granitoids  
814 or within leucosomes of metapelitic gneisses (e.g., Schneider et al., 2007; Skipton et al., 2016; Martz, 2017) range  
815 from  $1799.5 \pm 21.4$  Ma to  $1701.9 \pm 28.8$  Ma, with a mode at 1752.1 Ma and an isochroneisochron age of  $1753.4$   
816  $\pm 6.2$ – $12.4$  Ma ( $2\sigma$  internal;  $\pm 31$  Ma including external reproducibility) (Fig. 10). The mean age derived from  
817 single-spot analyses, together with the isochron age, falls within the temporal window of the exhumation and  
818 orogenic cooling phase of the Trans-Hudsonian orogen, a period characterized by the end of migmatization with  
819 the crystallization of leucosomes, the emplacement of leucogranitic intrusions, and the onset of hydrothermal  
820 activity associated with the cooling phase. Although its precise duration remains poorly constrained, this cooling  
821 interval is typically considered to span from ca. 1.77-Ga1770 Ma ( $750$  °C, 0.5 kbarGPa) to ca. 1.72-Ga1720 Ma  
822 ( $350$  °C, 0.2 kbarGPa), as documented in several studies (Annesley and Madore, 1994; Annesley et al., 1992,  
823 1997a, b, c; Annesley et al., 2005; Jeanneret et al., 2017; Martz, 2017). The end of this period is associated with  
824 pronounced retrograde transformations, including the breakdown of cordierite to phyllosilicates, biotite  
825 chloritization, sulfide, graphite and muscovite precipitation, quartz-rich fluid circulation, and dissolution-  
826 reprecipitation of monazite and zircon (Card, 2012, 20132014; Card and Noll, 2016). These processes are further  
827 constrained by cooling ages obtained from Rb—Sr biotite (Worden et al., 1985; Schneider et al., 2007), K—Ar  
828 muscovite (Philippe et al., 1993), and Ar—Ar muscovite (Alexandre et al., 2009). This timeframe has also been  
829 interpreted as reflecting a late thermal event associated with the emplacement of the Kivalliq Igneous Suite (KIS)  
830 to the northeast of the Athabasca Basin, with the Wollaston Domain being intruded by the Nueltin Granite of the

a mis en forme : Police :Italique

831 same suite (ca. 1770–1730 Ma), which may have reset U–Pb metamorphic rutile ages (Adlakha and Hattori,  
832 2021). Additionally, hydrothermal graphite, commonly spatially associated with early hydrothermal muscovite  
833 within the Wollaston-Mudjatik Transition shear zones, yields highly precise (<1 %) Re–Os isochron ages of  
834  $1731.5 \pm 7.4$  Ma ( $2\sigma$ ; MSWD = 1.3). These ages are interpreted to record graphite formation during the exhumation  
835 and orogenic cooling phase of the THO (Martz, 2017) and/or a period of elevated heat flow associated with the  
836 KIS emplacement (Adlakha and Hattori, 2021), wherein aqueous fluids mobilized carbon from adjacent wall rocks  
837 into semi-brittle to brittle-ductile shear zones (Toma et al., 2022). Overall, the Rb–Sr single-spot ages of early  
838 hydrothermal muscovite are consistent with the exhumation and orogenic cooling stage of the THO, during which  
839 anatectic granitoids were emplaced and/or magmatic activity of the Kivalliq Igneous Suite occurred, and they  
840 further align with the circulation of carbon-bearing aqueous fluids responsible for the formation of hydrothermal  
841 graphite. Comparison of the Rb–Sr ages obtained from alteration-free metamorphic and early hydrothermal  
842 muscovite with existing literature datasets indicates that the Rb–Sr system constitutes a suitable geochronometer  
843 in this geological context, as evidenced by the reproducibility of comparable Rb–Sr ages across four distinct sites  
844 within the WMTZ of the THO (Fig. 10).

### 845 **5.3. Assessing the reliability and applicability of the Rb–Sr system to date hydrothermal system in** 846 **crystalline basement**

847 Variably altered muscovite crystals occurring in illite-sudoite hydrothermal alteration zones in the four study sites  
848 along the WMTZ in the eastern Athabasca Basin display highly scattered Rb–Sr single-spot dates and substantial  
849 individual uncertainties, ranging from  $1756.2 \pm 22.945.8$  to  $1504.9 \pm 11.1357.0 \pm 64.8$  Ma. Despite this  
850 variability, muscovite from both altered pelitic and granitic protoliths shows comparable Rb–Sr single spot data  
851 distributions. Gaussian Mixture Modelling (GMM) and radial plot analysis define five statistically coherent  
852 populations shared by both muscovite generations affected by illite-sudoite alteration. However, their  
853 geochronological resolution is intrinsically limited because the analytical uncertainties are large. This reflects the  
854 inherent difficulty of precisely dating Paleoproterozoic geological events, as all isotopic systems tend to yield  
855 significant errors at such ancient ages (e.g., Fayek et al., 2002 and Riciputi, 2002; Alexandre et al., 2005; Rainbird  
856 et al., 2007; Schneider et al., 2007; Davis et al., 2011; Jeanneret et al., 2017; Adlakha and Hattori, 2021; Toma et  
857 al., 2022). The identification of five sub-populations does not imply that this is the only possible partitioning, but  
858 rather the one favored by the model under the present configuration, given the single-spot age values and their  
859 associated uncertainties. Small sub-populations should likewise be interpreted cautiously: although they may  
860 correspond to genuine age modes, they may also reflect asymmetries, outliers, or an artificial segmentation of an  
861 otherwise continuous distribution. Several studies have demonstrated that Gaussian mixture models can generate  
862 artificial components when fitting continuous or asymmetric distributions (McLachlan & Peel, 2000; Bishop,  
863 2006; Hastie et al., 2009, 2001). When substantial overlap exists between Gaussian components, the model often  
864 represents a single underlying population using multiple components (Fräley & Raftery, 2002). Ultimately, the  
865 components should be regarded primarily as probabilistic centers, which we attempt to compare with published  
866 datasets from the literature (Figs. 8, 10). It should be noted that BIC-based GMM algorithms tend to overestimate  
867 the number of populations with increasing sample size (Vermeesch, 2018), and that the present data are equally  
868 consistent with a smaller number of broader, partially overlapping distributions. The age components identified  
869 here are therefore not interpreted as discrete geological events but as probabilistic centers whose significance is

870 [evaluated through their correspondence with independently dated tectono-hydrothermal events documented in the](#)  
871 [regional record.](#)

872 A dominant population at ca. 1640 Ma, representing the majority of the dataset and potentially overlooked without  
873 prior petrographic constraints, is consistently recorded across four independent sites within the WMTZ of the  
874 THO, supporting the regional significance and robustness of this age population. This main cluster is accompanied  
875 by subordinate age groups at ca. 1680 Ma, ca. 1600 Ma, ca. 1550 Ma, and by a minor population near ca. 1467  
876 Ma, which display limited inter-site variability and likely reflect local heterogeneities or superimposed geological  
877 processes. These ages fall within the post-Athabasca Basin evolution, following basin deposition between ca. 1760  
878 and 1720 Ma (Ramaekers et al., 2007; Jeanneret et al., 2016) and continuing until ca. 1541 Ma (Creaser and  
879 Stasiuk, 2007). The data obtained in strongly illite-sudoite-altered zones of the basement, spatially associated with  
880 the uranium mineralization, record extensive mineralogical transformations and major geochemical and isotopic  
881 modifications driven by the circulation of basinal brines; i.e., the same fluids responsible for the characteristic  
882 illite-sudoite alteration halos observed around all unconformity-related uranium deposits in the eastern Athabasca  
883 Basin. The spread of the Rb–Sr single-spot dates may reflect either a single, long-lived fluid-rock interaction  
884 event with a paroxysm at ca. 1640 Ma, or a sequence of pulsed hydrothermal episodes represented by the GMM  
885 and radial plot populations.

886 The main peak at ca. 1640 Ma is widely recognized across the basin as marking a major sedimentary reorganization  
887 event associated with a rapid westward deepening and the deposition of deeper-water successions (ca. 1664–1590  
888 Ma; e.g., Pehrsson et al., 2023). This structural tilting correlates with the Racklan-Forward orogeny (ca. 1660–  
889 1590 Ma; e.g., Furlanetto et al., 2016; Pehrsson et al., 2023), a far-field intracontinental compressional event that  
890 reactivated deep crustal faults and deformed the northern Laurentian basement. Within the same time interval,  
891 zircon extracted from reworked tuff intraclasts of the Wolverine Point Formation (member b) yields a weighted  
892 mean  $^{207}\text{Pb}/^{206}\text{Pb}$  age of  $1644 \pm 13$  Ma ( $2\sigma$ ), interpreted as the crystallization age of the original tuff layers  
893 (Rainbird et al., 2007; Fig. 10). These tuffs are considered to be correlative with the Yavapai and Mazatzal  
894 Paleoproterozoic orogens, particularly within the Cochise block of the Mazatzal orogen, where juvenile arc  
895 terranes and syntectonic plutons range from ca. 1660 to 1600 Ma (Sims and Peterman, 1986; Karlstrom and  
896 Bowring, 1988; Eisele and Isachsen, 2001; Rainbird et al., 2007). In a broader geodynamic framework, this event  
897 may also be linked to the Racklan Orogeny of northwestern Laurentia, interpreted as the northwestern continuation  
898 of the Mazatzal orogenic system. Together, these orogenic events define a large-scale Paleoproterozoic  
899 accretionary system that affected the margins of the Canadian Shield and promoted significant crustal reworking,  
900 consistent with the hypothesis of a circum-Laurentian orogenic belt (e.g., Furlanetto et al., 2013). U–Pb data  
901 obtained from fluorapatite in the Athabasca Basin indicate a coherent phase of phosphate cementation, constrained  
902 by weighted mean  $^{207}\text{Pb}/^{206}\text{Pb}$  ages obtained on apatite with high radiogenic-to-common Pb ratios, and by Pb–Pb  
903 regression lines that are independent of common Pb (e.g., Davis et al., 2011). Fluorapatite from the Smart, Manitou  
904 Falls, and Wolverine Point formations of the Athabasca Basin yielded ages of  $1609 \pm 30$  Ma,  $1638 \pm 12$  Ma, and  
905  $1625 \pm 17$  Ma, respectively, clustering around a mean age of approximately  $1630 \pm 9$  Ma (e.g., Davis et al., 2011;  
906 Fig. 10). These ages are interpreted to record a basin-wide circulation of warm, oxidizing, P-rich brines produced  
907 by fluid-rock interactions between basinal brines and the altered crystalline basement during mesogenetic  
908 diagenesis. This large-scale fluid circulation is likely tectonically driven and related to the regional geodynamic

909 evolution of the basin, as proposed by Pehrsson et al. (2023), and can be temporally constrained to ca. 1640 Ma  
910 based on the concordance between Rb–Sr and U–Pb apatite ages.

911 [Taken together, these observations support the interpretation of a major basin-wide hydrothermal event at ca. 1640](#)  
912 [Ma](#). Illite-sudoite alteration dated at ca. 1640 Ma can be interpreted in two alternative, but not mutually exclusive,  
913 ways. First, this alteration may predate the main stage of uranium oxide precipitation, commonly dated between  
914 ca. 1590 and 1200 Ma based on U–Pb analyses of uraninite and K–Ar/Ar–Ar geochronology of clay minerals  
915 (Cumming and Krstic, 1992; Philippe et al., 1993; McGill et al., 1993; Fayek [et al., 2002](#) and Riciputi, 2002;  
916 Alexandre et al., 2009; Cloutier et al., 2011; Powell et al., 2022). In this scenario, the ca. 1640 Ma illite-sudoite  
917 alteration would represent a basin-scale hydrothermal event that prepared the basement-basin interface for  
918 subsequent uranium mineralization by enhancing permeability, redox reactivity, and uranium mobility.  
919 Alternatively, the 1640 Ma alteration may record an early phase of uranium mineralization itself, subsequently  
920 overprinted and partially reset by younger tectono-hydrothermal events. Such a model is consistent with studies  
921 demonstrating that the U–Pb systematics of uraninite and associated alteration minerals in unconformity-related  
922 uranium deposits are commonly affected by multiple fluid-flow episodes, leading to partial Pb loss and a wide  
923 dispersion of apparent ages (Kotzer and Kyser, 1990; Fayek and Kyser, 1997; Fayek et al., [2002a,b](#)2002; [Fayek](#)  
924 [and Riciputi, 2002](#); Kyser et al., 2015). Consequently, an older hydrothermal and/or mineralizing system active  
925 during the ca. 1680–1640 Ma interval cannot be excluded, but may remain cryptic due to subsequent uranium  
926 remobilization and isotopic resetting during younger basin-wide fluid circulation events. This interpretation is  
927 further supported by analogues from northern Australia, where *in situ* U–Pb analyses of uraninite indicate initial  
928 mineralization or hydrothermal alteration as early as ca. 1680–1640 Ma, followed by multiple resetting episodes  
929 extending into the Mesoproterozoic and Paleozoic (Clauer et al., 2015; Skirrow et al., 2016).

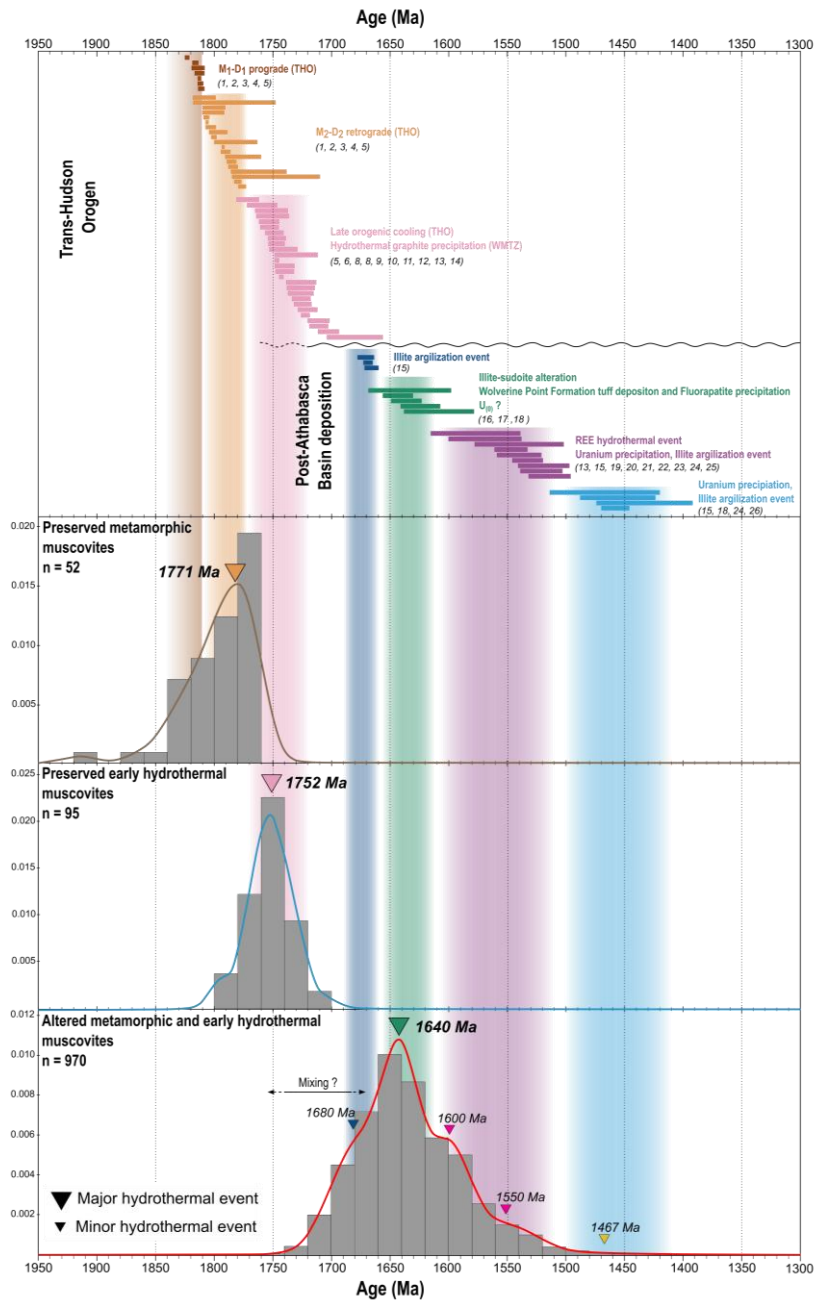
930 In addition to the main population associated with illite-sudoite alteration at ca. 1640 Ma, several consistent  
931 statistical sub-populations are identified by the GMM. However, no chemical or mineralogical modifications are  
932 observed in the zones where these single-spot data were measured. A first sub-population calculated around ca.  
933 1680 Ma can be interpreted in two ways. It may represent a mixed population between preserved and altered data  
934 (Fig. 6F), reflecting the onset of alteration and a partial loss of radiogenic <sup>87</sup>Sr caused by this early alteration stage  
935 at ca. 1640 Ma. Such mixing would tend to skew the single-spot Rb–Sr dates of metamorphic muscovite, which  
936 crystallized prior to early hydrothermal muscovite, toward older dates. Alternatively, this ca. 1680 Ma population  
937 could correspond to an argillization episode dated to this period by Alexandre et al. (2009) using Ar–Ar analyses  
938 on basement-hosted illite, which yielded pseudo-plateau ages at McArthur River of 1669 ± 4 Ma, 1666 ± 6 Ma,  
939 and 1671 ± 7 Ma, interpreted as a pre-ore alteration event (Fig. 10). However, the actual geological significance  
940 of each published age and its attribution to a specific event are often difficult to evaluate in this context, due to  
941 successive episodes of intense fluid circulation and associated fluid-rock interaction processes that promote  
942 substantial Ar loss and consequently yield younger ages (Chi et al., 2018). Nevertheless, during this time interval,  
943 the basin is characterized by a half-graben architecture, with sediment transport predominantly directed toward the  
944 northwest and enhanced sediment accumulation along the southeastern basin margin. This configuration reflects  
945 an intracontinental extensional regime established after the THO orogeny, which may have facilitated the  
946 circulation of early fluids within the basement and may also have reset the Rb–Sr system.

947 [The younger age populations at ca. 1600–1550 Ma are consistent with hydrothermal and mineralizing events that](#)  
948 [have been independently documented throughout the Athabasca Basin.](#) The sub-populations at ca. 1600 Ma and  
949 ca. 1550 Ma document hydrothermal activity previously identified in the Athabasca Basin and its underlying  
950 basement, although it remains unclear whether they reflect a single event, a series of pulsatile episodes, or  
951 processes potentially related to, or distinct from, the ca. 1640 Ma event. This hydrothermal activity is highlighted  
952 in the basement by anatase precipitation, a low-pressure, low-temperature TiO<sub>2</sub> polymorph, yielding a weighted  
953 mean <sup>207</sup>Pb/<sup>206</sup>Pb age of 1569 ± 31 Ma (MSWD = 0.30, n = 5, 2σ; Adlakha and Hattori, 2021, Fig. 10). This age  
954 has been interpreted as reflecting the onset of oxidizing hydrothermal activity in the basement, contemporaneous  
955 with U precipitation at the world-class McArthur River deposit, which has been dated by U–Pb analyses of U  
956 oxides with two discordant ages of 1540 ± 19 Ma (Alexandre et al., 2009) and 1540 ± 38 Ma (Alexandre [and](#)  
957 [Kyser, et al., 2005](#)). Additional ages at ca. 1520 Ma, including 1514 ± 18 Ma ([CummingsCumming](#) and Krstic,  
958 1992), 1519 ± 22 Ma (Fayek [et al., 2002b](#) and [Riciputi, 2002](#)), and 1521 ± 18 Ma (McGill et al., 1993), have been  
959 interpreted as minimum crystallization ages for primary uraninite. An episode of argillization contemporaneous  
960 with these fluid-circulation events has also been identified at 1577 ± 38 Ma (K–Ar muscovite from gneiss;  
961 Philippe et al., 1993) at Cigar Lake, and at 1533 ± 13 Ma (Ar–Ar on illite; Alexandre et al., 2009) at McArthur  
962 River. A further rare-earth-phosphate hydrothermal episode is documented in the eastern Athabasca Basin within  
963 the Maw Zone rare-earth-element deposit. U–Pb dating of xenotime yielded a <sup>207</sup>Pb/<sup>206</sup>Pb age of 1547 ± 14 Ma  
964 (Rabiei et al., 2017; Fig. 10), and both isotopic signatures and fluid-inclusion characteristics support the  
965 interpretation that the fluids responsible for xenotime precipitation were part of the same oxidizing-reducing  
966 hydrothermal system involved in the development of major uraninite mineralization across the Athabasca Basin.  
967 More broadly, these events are associated with a renewed phase of subsidence and marine flooding, attributed to  
968 intracontinental rifting or extension and linked to the emplacement of the Kuungmi Formation basalts in the  
969 adjacent Thelon Basin. This rifting episode coincides with a reorganization of the Laurentian crust following the  
970 Australia-Laurentia collision, and precedes the stabilization of Nuna, potentially promoting large-scale fluid  
971 circulation through both the basement and the basin, capable of resetting the Rb–Sr geochronometer in muscovite.

972 Finally, the minor [age](#) population at ca. 1467 Ma [could](#) correspond to [a first mineralizing early](#)  
973 [mineralization](#) event, [as](#) recorded [in the Cigar Lake deposit](#) by discordant U–Pb ages of 1467 ± 47 Ma [at the Cigar](#)  
974 [Lake deposit](#) (Fayek [et al., 2002b](#)) and [Riciputi, 2002](#)) and by weighted mean <sup>207</sup>Pb/<sup>206</sup>Pb ages of 1458 ± 12 Ma [at](#)  
975 [the McArthur River deposit](#) (Kister, 2003). An argillization event contemporaneous with these fluid-circulation  
976 episodes has also been identified at 1456 ± 32 Ma (K–Ar on the <2 μm fraction from gneiss; Philippe et al., 1993)  
977 at Cigar Lake, and at 1433 ± 31 Ma (Ar–Ar on illite; Alexandre et al., 2009) at McArthur River. Overall, current  
978 data do not allow discrimination between a single protracted fluid-rock interaction episode at ca. 1640 Ma leading  
979 to the formation of an illite-sudoite alteration halo and multiple episodic fluid pulses to account for the Rb–Sr  
980 single-spot age distribution in altered metamorphic and early hydrothermal muscovite. Nevertheless, these results  
981 clearly demonstrate the applicability of the Rb–Sr chronometer for constraining hydrothermal fluid circulation at  
982 basin-basement interfaces. The distinct age populations identified in muscovite and alteration products correspond  
983 to tectono-hydrothermal events that are independently recognized in the regional geological record and have been  
984 previously dated using other geochronological methods. Comparable multi-stage fluid-thermal histories have been  
985 documented in other hydrothermal systems, such as gold deposit systems, where primary mineral phases  
986 commonly preserve evidence for repeated isotopic resetting, trace-element redistribution, and microstructural

987 overprinting associated with episodic fluid and heat input (e.g., Bevan et al., 2021; Chen et al., 2024; Drake et al.,  
988 2023; Huang et al., 2023; Liu et al., 2018; Mao et al., 2013; Olierook et al., 2020; Redaa et al., 2021, 2022; Şengün  
989 et al., 2019; Wang et al., 2022; Zametzer et al., 2022; Tian et al., 2024; Boschetti et al., 2025; Huang et al., 2025).  
990 Such behaviour underscores the capacity of mineral-scale chronometers to resolve protracted hydrothermal  
991 evolution. In this context, the present data suggest that the Rb–Sr system in muscovite and alteration minerals is  
992 sensitive to successive hydrothermal events at basin-basement interfaces, highlighting its potential as a robust tool  
993 for reconstructing the timing and duration of fluid circulation processes, while emphasizing the need for further  
994 work to evaluate mineralogical and geochemical controls on system behaviour. Although these initial results are  
995 promising, further work is required to assess potential mineralogical or geochemical specificities that may  
996 influence the Rb–Sr system under such conditions.

997



998

999 **Figure 10.** Compilation of published geochronological constraints for the Trans-Hudson orogen and the Athabasca Basin, integrated  
 1000 with the new Rb-Sr single-spot ages obtained in this study. The onset of sedimentation in the Athabasca Basin occurred at ca. 1760

1001 1720 Ma (Ramaekers et al., 2007; Jeanneret et al., 2016). The diagram synthesizes available ages documenting the prograde  
1002 metamorphic path, the retrograde evolution, and the late-orogenic cooling stages of the Trans-Hudson orogen, together with the timing  
1003 of hydrothermal events recorded both in the Athabasca Basin and in its crystalline basement. Literature ages are derived from multiple  
1004 minerals and chronometers. Included datasets comprise: U–Pb on zircon and monazite from (1) Annesley et al., 1992; (2) Annesley et  
1005 al., 1997; (3) Annesley et al., 1999; (4) Toma et al., 2024; (5) Jeanneret et al., 2016; (6) Card, 2012; (7) Card, 2014; (8) Card and Noll,  
1006 2016); Rb–Sr on biotite from (9) Worden et al., 1985; (10) [SehenierSchneider](#) et al., 2007); U–Pb on rutile from (11) Adlakha and  
1007 Hattori, 2021); Ar–Ar on muscovite from (12) Alexandre et al., 2009); K–Ar on muscovite from (13) Philippe et al., 1993); Re–Os on  
1008 graphite from (14) Toma et al., 2024); Ar–Ar on illite from (15) Alexandre et al., 2009); U–Pb on zircon from (16) Rainbird et al.,  
1009 [2017](#)); U–Pb on fluorapatite from (17) Davis et al., 2011); K–Ar on <2 µm fractions from gneiss from (18) Philippe et al., 1993);  
1010 U–Pb on xenotime from (19) Rabiei et al., 2017); U–Pb on anatase from (20) Adlakha and Hattori, 2021); U–Pb on UO<sub>2</sub> from (21)  
1011 Alexandre et al., 2009; (22) Alexandre [and Kyser](#) et al., 2005; (23) [CummingsCumming](#) and Krstić, 1992; (24) [Fayek et al., 2002](#) and  
1012 [Ricciuti, 2002](#); (25) McGill et al., 1993; (26) Kister, 2003). Probability density distribution and histogram plots of Rb–Sr single-spot  
1013 ages obtained from preserved early hydrothermal and metamorphic muscovite unaffected by post-crystallization alteration are  
1014 correlated with recognized Trans-Hudson orogenic events. Probability density distribution and histogram plots of Rb–Sr single-spot  
1015 ages derived from muscovites overprinted by post-crystallization illite-sudoite alteration are presented along with the results of a  
1016 Gaussian Mixture Model (GMM) used to identify distinct age components. The central age population at ca. 1640 Ma is interpreted to  
1017 record the main illite-sudoite hydrothermal alteration event, whereas subordinate components may correspond to additional  
1018 hydrothermal pulses documented in the literature.

## 1019 6. Conclusions

1020 This study tests the relevance and limitations of the Rb–Sr chronometer applied to muscovite from pelitic gneisses,  
1021 including migmatites, and granitoids from the Paleoproterozoic basement of the Wollaston-Mudjatik Transition  
1022 Zone, within the context of hydrothermal alteration (formed by an association of illite and sudoite) associated with  
1023 the formation of Athabasca Basin unconformity-related uranium deposits. The primary objective was to determine  
1024 to what extent this isotopic system, conventionally used to date the crystallization or cooling of crustal rocks, can  
1025 also record and quantify late-stage fluid circulation events, despite the complexity induced by partial system  
1026 reopening through fluid-rock interaction.

1027 Petrographic and isotopic analyses of preserved domains demonstrate that, in areas lacking illite-sudoite alteration,  
1028 metamorphic and early hydrothermal muscovite yield ages of ca. 1780 Ma and ca. 1750 Ma, respectively. Retro-  
1029 metamorphic muscovite specifically records the transition to temperatures below its closure temperature (450–  
1030 600 °C), marking cooling, possibly in the presence of fluids, following the peak metamorphism and isothermal  
1031 decompression of the THO basement. Early hydrothermal muscovite, in turn, records the exhumation and orogenic  
1032 cooling phase of the THO, during which anatectic granitoids were emplaced and/or magmatic activity of the  
1033 Kivalliq Igneous Suite occurred. Its formation is also consistent with the circulation of carbon-bearing aqueous  
1034 fluids that facilitated the development of hydrothermal graphite. These results demonstrate that, in minimally  
1035 altered domains, the Rb–Sr system yields ages consistent with established geochronological constraints obtained  
1036 from independent isotopic systems and mineral phases for both episodes, thereby confirming that the Rb–Sr  
1037 chronometer remains fully reliable for dating the terminal Paleoproterozoic thermo-metamorphic events.

1038 In contrast, muscovite from pelitic gneiss or granitic protoliths affected by illite-sudoite alteration developed after  
1039 the deposition of the Athabasca Basin displays deeply modified mineralogical, geochemical, and isotopic  
1040 signatures. These signatures reflect the micrometre-scale reopening of the Rb–Sr isotopic system through fluid-  
1041 rock interaction during brine circulation, in response to the structural destabilization of muscovite during

1042 illitization and/or sudoitization. The preferential transfer of radiogenic  $^{87}\text{Sr}$  into clay phases and/or the fluid phase  
1043 constitutes the major mechanism driving isotopic resetting.

1044 The dominant population of Rb–Sr single spot data at ca. 1640 Ma reflects a major hydrothermal event. This age  
1045 interval coincides with a first-order sedimentary reorganization of the basin and with crustal-scale reactivation  
1046 related to the late Paleoproterozoic Racklan-Mazatzal orogenic system (ca. ~~1.66–1.59 Ga~~1660–1590 Ma), which  
1047 affected the northwestern to southern margins of Laurentia and the adjacent edge of the Canadian Shield. These  
1048 tectonic processes are accompanied by widespread fluid circulation and diagenetic to hydrothermal events in the  
1049 Athabasca Basin, as independently documented by U–Pb ages obtained on fluorapatite. Comparison with other  
1050 geochronological constraints and regional geodynamic reconstructions supports the interpretation that the ages  
1051 measured on altered muscovite and associated alteration products are geologically meaningful and temporally  
1052 consistent. Rather than reflecting localized or spurious resetting, these ages are best interpreted as recording a  
1053 geologically realistic and regionally significant hydrothermal event, broadly coeval with the Racklan-Mazatzal  
1054 orogenic continuum, which represents the northwestern expression of a circum-Laurentian orogenic belt affecting  
1055 the margins of the Canadian Shield. It corresponds to the principal illite-sudoite alteration event responsible for  
1056 the mineralized halos around uranium deposits and represents the key event recorded by altered muscovites.  
1057 Additional age populations reflect further hydrothermal episodes or fluid-reactivation phases: (i) ca. 1680 Ma,  
1058 possibly linked to a pre-ore argillization event documented by Ar–Ar ages on illite, or to an initial stage of partial  
1059 disturbance of the Rb–Sr system; (ii) ca. 1600 Ma and ca. 1550 Ma, corresponding to a major oxidizing  
1060 hydrothermal phase concomitant with a mineralizing event, recognized from U–Pb ages on anatase, xenotime,  
1061 and uraninite, notably at McArthur River; (iii) ca. 1467 Ma, associated with a major mineralizing episode recorded  
1062 in the district (Cigar Lake).

1063 This study demonstrates that the *in situ* Rb–Sr geochronometer applied to muscovite and related alteration  
1064 products constitutes a relevant tool not only for constraining late-metamorphic and late-magmatic and/or early  
1065 hydrothermal histories in unaltered domains, but also for identifying and dating post-crystallization hydrothermal  
1066 circulation events after basin sedimentation, associated with unconformity-related metallic deposits. By coupling  
1067 detailed petrographic analysis with *in situ* geochemical characterization, it becomes possible to distinguish  
1068 preserved ages reflecting Paleoproterozoic crystallization or cooling from reset ages marking Mesoproterozoic  
1069 hydrothermal episodes. The Rb–Sr chronometer thus emerges as a powerful and complementary tool within the  
1070 existing suite of fluid tracers, opening new perspectives for the temporal and spatial reconstruction of paleo-  
1071 hydrothermal systems across basin-basement interfaces.

#### 1072 **Code and data availability**

1073 All data supporting the findings of this study are provided in the Appendix.

#### 1074 **Supplement**

1075 The supplement related to this article is available at:

#### 1076 **Author contributions**

1077 Conceptualization: QB, JM; Fieldwork: QB, GM, EF, TO, AK, JM; Methodology and data acquisition: QB, CP,  
1078 AL, JM; Data curation: QB, MS, TO, CP, AL, JM; Writing (original draft preparation): QB, GM, EF, CB, AL, PM,  
1079 JM; Funding acquisition: JM.

#### 1080 **Competing interests**

1081 The authors declare that they have no conflict of interest.

#### 1082 **Disclaimer**

1083 Publisher's note: Copernicus Publications remains neutral with regard to jurisdictional claims made in the text,  
1084 published maps, institutional affiliations, or any other geographical representation in this paper. While Copernicus  
1085 Publications makes every effort to include appropriate place names, the final responsibility lies with the authors.

#### 1086 **Acknowledgements**

1087 The French Agence Nationale de la Recherche (ANR) and Orano are thanked for funding this project. The authors  
1088 gratefully acknowledge Orano Canada and Cameco for providing access to the field sites, samples, and data  
1089 transfer. Special thanks are extended to Charles Khairallah, Magdalena Anderson, Andrew Kaczowka, and Gerard  
1090 Zaluski for their valuable assistance during the field missions and data sharing.

#### 1091 **Financial support**

1092 This research has been supported by the French Agence Nationale de la Recherche (ANR) and Orano, under grant  
1093 ANR-21-CHIN-0006 (project GeomIn3D).

#### 1094 **References**

1095 Adlakha, E. E., and Hattori, K.: Compositional variation and timing of aluminum phosphate-sulfate minerals in  
1096 the basement rocks along the P2 fault and in association with the McArthur River uranium deposit, Athabasca  
1097 Basin, Saskatchewan, Canada, *Am. Mineral.*, 100, 1386-1399, 10.2138/am-2015-5069, 2015.

1098 Adlakha, E., and Hattori, K.: Thermotectonic events recorded by U–Pb geochronology and Zr-in-rutile  
1099 thermometry of Ti oxides in basement rocks along the P2 fault, eastern Athabasca Basin, Saskatchewan, Canada,  
1100 *Geol. Soc. Am. Bull.*, 134, 567-576, 10.1130/B35820.1, 2021.

1101 Aldega, L., Viola, G., Casas-Sainz, A., Marcén, M., Román-Berdiel, T., and van der Lelij, R.: Unraveling Multiple  
1102 Thermotectonic Events Accommodated by Crustal-Scale Faults in Northern Iberia, Spain: Insights From K–Ar  
1103 Dating of Clay Gouges, *Tectonics*, 38, 3629-3651, <https://doi.org/10.1029/2019TC005585>, 2019.

1104 Alexandre, P., Kyser, K., Polito, P., and Thomas, D.: Alteration mineralogy and stable isotope geochemistry of  
1105 Paleoproterozoic basement-hosted unconformity-type uranium deposits in the Athabasca Basin, Canada, *Econ.*  
1106 *Geol.*, 100, 1547-1563, 10.2113/gsecongeo.100.8.15473, 2005.

1107 Alexandre, P. and Kyser, T. K.: GEOCHEMISTRY OF URANIFEROUS BITUMEN IN THE SOUTHWEST  
1108 ATHABASCA BASIN, SASKATCHEWAN, CANADA, *Economic Geology*, 101, 1605-1612,  
1109 <https://doi.org/10.2113/gsecongeo.101.8.1605>, 2006.

1110 Alexandre, P., Kyser, K., Thomas, D., Polito, P., and Marlat, J.: Geochronology of unconformity-related uranium  
1111 deposits in the Athabasca Basin, Saskatchewan, Canada and their integration in the evolution of the basin, *Miner.*  
1112 *Deposita*, 44, 41-59, [10.1007/s00126-007-0153-3](https://doi.org/10.1007/s00126-007-0153-3), 2009.

1113 Alexandre, P., Jiricka, D., and Witt, G.: Formation and evolution of the Centennial unconformity-related uranium  
1114 deposit in the south-central Athabasca Basin, Canada, *Econ. Geol.*, 107, 385-400, [10.2113/econgeo.107.3.385](https://doi.org/10.2113/econgeo.107.3.385),  
1115 2012.

1116 Anders, M. H., Laubach, S. E., and Scholz, C. H.: Microfractures: A review, *Journal of Structural Geology*, 69,  
1117 377-394, <https://doi.org/10.1016/j.jsg.2014.05.011>, 2014.

1118 Ansdell, K. M.: Tectonic evolution of the Manitoba-Saskatchewan segment of the Paleoproterozoic Trans-Hudson  
1119 Orogen, Canada, *Can. J. Earth Sci.*, 42, 741-759, <https://doi.org/10.1139/e05-035>, 2005.

1120 Annesley, I., Madore, C., and Krogh, T. E.: U-Pb ~~geochronology of some granitoids~~ zircon, titanite, and monazite  
1121 ages from the ~~Peter-Lake~~ Wollaston Domain: A summary, Summary of Investigations, Saskatchewan Geological  
1122 Survey, Saskatchewan Energy and mines, Miscellaneous Report, ~~168-171~~ 92-4, p. 61-65, 1992.

1123 Annesley, I.R., and Madore, C.: A geological study of the Wollaston-Mudjatik domain boundary in the Wollaston  
1124 Lake area, Hearne Province, Saskatchewan, Saskatchewan Research Council, Publ. R-1230-6-C-94, 162 p., 1994.

1125 Annesley, I.R., Madore, C., and Shi, R.: Thermotectonic evolution of the Wollaston EAGLE Project Area ,  
1126 Saskatchewan Research Council, Publ. R-1420-2-C-97, Part 1, 1-62, 1997a.

1127 Annesley, I., Madore, C., Shi, R., and Krogh, T.: U-Pb geochronology of thermotectonic events in the Wollaston  
1128 Lake area, Wollaston Domain: A summary of 1994-1996 results, Summary of Investigations 1997, Saskatchewan  
1129 Geological Survey, Saskatchewan Energy and Mines, 1, 162-173, 1997b.

1130 Annesley, I.R., Madore, C., and Krogh, T.E.: U-Pb geochronology of peraluminous pegmatites from  
1131 the Wollaston Lake area, northern Saskatchewan, *Geol. Assoc. Can.-Mineral. Assoc. Can. Annual Meeting*,  
1132 *Program with Abstracts*, 22, A-4, 1997c.

1133 Annesley, I.R., Madore, C., Shi, R., and Krogh, T.E.: U-Pb geochronology and thermotectonic history of the  
1134 Wollaston Domain in the Wollaston Lake area, Hearne Province, Saskatchewan, *Geol. Assoc. Can.-Mineral. Assoc.*  
1135 *Can. Annual Meeting, Program with Abstracts*, 21, A-4, 1999a.

1136 Annesley, I.R., Madore, C., Krogh, T.E., Kwok, Y.Y., and Kamo, S.L.: New U-Pb zircon and  
1137 monazite geochronological results for Archean and Paleoproterozoic basement to the southeastern part of the  
1138 Athabasca Basin, Saskatchewan, Saskatchewan Geological Survey, Misc. Rep. 99-4.2, 90-99, 1999b.

1139 Annesley, I. R., Madore, C., and Portella, P.: Geology and thermotectonic evolution of the western margin of the  
1140 Trans-Hudson Orogen: evidence from the eastern sub-Athabasca basement, Saskatchewan, *Can. J. Earth Sci.*, 42,  
1141 573-597, <https://doi.org/10.1139/e05-034>, 2005.

1142 Beaufort, D., Patrier, P., Laverret, E., Bruneton, P., and Mondy, J.: Clay Alteration Associated with Proterozoic  
1143 Unconformity-Type Uranium Deposits in the East Alligator Rivers Uranium Field, Northern Territory, Australia,  
1144 *Economic Geology*, 100, 515-536, <https://doi.org/10.2113/gsecongeo.100.3.515>, 2005.

1145 Bevan, D., Coath, C. D., Lewis, J., Schwieters, J., Lloyd, N., Craig, G., Wehrs, H., and Elliott, T.: In situ Rb–Sr  
1146 dating by collision cell, multicollection inductively-coupled plasma mass-spectrometry with pre-cell mass-filter,  
1147 (CC-MC-ICPMS/MS), *J. Anal. At. Spectrom.*, 36, 917-931, <https://doi.org/10.1039/D1JA00006C>, 2021.

1148 Boiron, M.-C., Cathelineau, M., and Richard, A.: Fluid flows and metal deposition near basement /cover  
1149 unconformity: lessons and analogies from Pb-Zn-F-Ba systems for the understanding of Proterozoic U deposits,  
1150 *Geofluids*, 10, 270-292, <https://doi.org/10.1111/j.1468-8123.2010.00289.x>, 2010.

1151 Boschetti, L., Boullerne, C., Rolland, Y., Schwartz, S., Milesi, G., Bienveignant, D., Macret, E., Charpentier, D.,  
1152 Münch, P., Mercadier, J., Iemmolo, A., Lanari, P., Rossi, M., and Mouthereau, F.: Shear zone memory revealed by  
1153 in-situ Rb–Sr and 40Ar/39Ar dating of Pyrenean and Alpine tectonic phases in the external Alps, *Lithos*, 514-  
1154 515, 108168, <https://doi.org/10.1016/j.lithos.2025.108168>, 2025.

1155 Bickford, M., Chiarenzelli, J., Van Schmus, W., Collerson, K. D., and Lewry, J.: Proterozoic collisional tectonism  
1156 in the Trans-Hudson orogen, Saskatchewan, *Geology*, 18, 14-18, [https://doi.org/10.1130/0091-7613\(1990\)018](https://doi.org/10.1130/0091-7613(1990)018)  
1157 %253C0014:PCTITT%253E2.3.CO;2, 1990.

1158 Bickford, M. E., Mock, T. D., Steinhart Iii, W. E., Collerson, K. D., and Lewry, J. F.: Origin of the Archean Sask  
1159 craton and its extent within the Trans-Hudson orogen: evidence from Pb and Nd isotopic compositions of basement  
1160 rocks and post-orogenic intrusions, *Can. J. Earth Sci.*, 42, 659-684, <https://doi.org/10.1139/e04-064>, 2005.

1161 ~~Bisehoff, A., Heap, M. J., Mikkola, P., Kuva, J., Reuschlé, T., Jolis, E. M., Engström, J., Reijonen, H., and Leskelä,  
1162 T.: Hydrothermally altered shear zones: A new reservoir play for the expansion of deep geothermal exploration in  
1163 crystalline settings, *Geothermics*, 118, 102895, <https://doi.org/10.1016/j.geothermics.2023.102895>, 2024.~~

1164 Bishop, C. M. and Nasrabadi, N. M.: *Pattern recognition and machine learning*, Springer, 2006.

1165 Brigatti, M. F. and Guggenheim, S.: Mica Crystal Chemistry and the Influence of Pressure, Temperature, and Solid  
1166 Solution on Atomistic Models, *Reviews in Mineralogy and Geochemistry*, 46, 1-97,  
1167 <https://doi.org/10.2138/rmg.2002.46.01>, 2002.

1168 Brooks, C., Hart, S. R., Hofmann, A., and James, D. E.: Rb–Sr mantle isochrons from oceanic regions, *Earth and  
1169 Planetary Science Letters*, 32, 51-61, [https://doi.org/10.1016/0012-821X\(76\)90184-9](https://doi.org/10.1016/0012-821X(76)90184-9), 1976.

1170 Bruneton, P.: Geological environment of the Cigar Lake uranium deposit, *Can. J. Earth Sci.*, 30, 653-673,  
1171 <https://doi.org/10.1139/e93-054>, 1993.

1172 Campanha, G. A. C., Hueck, M., Wemmer, K., Esteves, M. C. B., Joncew, H. C., Faleiros, F. M., and Veloso, R. S.  
1173 S.: Foreland deformation of Brasileiro orogens at the eastern and western margins of the São Francisco Craton:  
1174 K–Ar illite dating of the Araçuaí and Brasília fold-and-thrust belts, *JGS*, 183, jgs2025-138,  
1175 <https://doi.org/10.1144/jgs2025-138>, 2026.

1176 Card, C.: *The Origins of Anomalously Graphitic Rocks and Quartzite Ridges in the Basement to the Southeastern  
1177 Athabasca Basin*, 2012.

1178 Card, C.: *Altered Pelitic Gneisses and Associated " Quartzite Ridges " Beneath the Southeastern Athabasca Basin:  
1179 Alteration Facies and their Relationship to Uranium Deposits along the Wollaston-Mudjatik Transition*, 2014.

1180 Card, C. and Noll, J.: Host-Rock Protoliths, Pre-Ore Metasomatic Mineral Assemblages and Textures, and Exotic  
1181 Rocks in the Western Athabasca Basin: Ore-System Controls and Implications for the Unconformity- Related  
1182 Uranium Model, <https://doi.org/10.13140/RG.2.2.26473.70241>, 2016.

1183 Carl, C., Pechmann, E. V., Höhndorf, A., and Ruhmann, G.: Mineralogy and U/Pb, Pb/Pb, and Sm/Nd  
1184 geochronology of the Key Lake uranium deposit, Athabasca Basin, Saskatchewan, Canada, *Can. J. Earth Sci.*, 29,  
1185 879-895, <https://doi.org/10.1139/e92-075>, 1992.

1186 Cathelineau, M., Boiron, M.-C., Fourcade, S., Ruffet, G., Clauer, N., Belcourt, O., Coulibaly, Y., Banks, D. A., and  
1187 Guillocheau, F.: A major Late Jurassic fluid event at the basin/basement unconformity in western France:  
1188  $^{40}\text{Ar}/^{39}\text{Ar}$  and  $\text{K}-\text{Ar}$  dating, fluid chemistry, and related geodynamic context, *Chemical Geology*, 322-323, 99-  
1189 120, <https://doi.org/10.1016/j.chemgeo.2012.06.008>, 2012.

1190 Chen, M., Chen, G., An, P., Zhang, L., and Wang, Y.: In situ illite  $\text{Rb}-\text{Sr}$  dating indicates the coevality of Carlin-  
1191 type gold deposits inside and around the isolated carbonate platform in western Guangxi, China, *Ore Geology*  
1192 *Reviews*, 165, 105905, <https://doi.org/10.1016/j.oregeorev.2024.105905>, 2024.

1193 Cherniak, D. J. and Watson, E. B.: Pb diffusion in zircon, *Chemical Geology*, 172, 5-24,  
1194 [https://doi.org/10.1016/S0009-2541\(00\)00233-3](https://doi.org/10.1016/S0009-2541(00)00233-3), 2001.

1195 Cherniak, D. J., Watson, E. B., Grove, M., and Harrison, T. M.: Pb diffusion in monazite: a combined RBS/SIMS  
1196 study, *Geochimica et Cosmochimica Acta*, 68, 829-840, <https://doi.org/10.1016/j.gca.2003.07.012>, 2004.

1197 Chi, G., Li, Z., Chu, H., Bethune, K. M., Quirt, D. H., Ledru, P., Normand, C., Card, C., Bosman, S., Davis, W. J.,  
1198 and Potter, E. G.: A SHALLOW-BURIAL MINERALIZATION MODEL FOR THE UNCONFORMITY-  
1199 RELATED URANIUM DEPOSITS IN THE ATHABASCA BASIN, *Economic Geology*, 113, 1209-1217,  
1200 <https://doi.org/10.5382/econgeo.2018.4588>, 2018.

1201 Chiarenzelli, J.: Petrogenesis and tectonic significance of the Guncoat and Nistowiak gneisses, Glennie Lake  
1202 Domain, northern Saskatchewan, Unpublished Ph. D. thesis, University of Kansas, 229, 1989.

1203 Chiarenzelli, J., Aspler, L., Villeneuve, M., and Lewry, J.: Early Proterozoic Evolution of the Saskatchewan Craton  
1204 and Its Allochthonous Cover, Trans-Hudson Orogen, *The Journal of Geology*, 106, 247-268,  
1205 <https://doi.org/10.1086/516020>, 1998.

1206 Clauer, N., ~~Vidal, P., and Auvray, B.: Differential behaviour of the Rb-Sr and K-Ar systems of spilitic flows and~~  
1207 ~~interbedded metasediments: the spilitic group of Erquy (Brittany, France). Paleomagnetic implications, *Contr.*~~  
1208 ~~*Mineral. and Petrol.*, 89, 81-89, <https://doi.org/10.1007/BF01177593>, 1985.~~

1209 ~~Clauer, N.,~~ Środoń, J., Francu, J., and Šucha, V.:  $\text{K}-\text{Ar}$  dating of illite fundamental particles separated from illite-  
1210 smectite, *Clay Minerals*, 32, 181-196, <https://doi.org/10.1180/claymin.1997.032.2.02>, 1997.

1211 Clauer, N., Mercadier, J., Patrier, P., Laverret, E., and Bruneton, P.: Relating unconformity-type uranium  
1212 mineralization of the Alligator Rivers Uranium Field (Northern Territory, Australia) to the regional Proterozoic  
1213 tectono-thermal activity: An illite  $\text{K}-\text{Ar}$  dating approach, *Precambrian Research*, 269, 107-121,  
1214 <https://doi.org/10.1016/j.precamres.2015.08.007>, 2015.

1215 Cloutier, J., Kyser, K., Olivo, G. R., Alexandre, P., and Halaburda, J.: The Millennium Uranium Deposit, Athabasca  
1216 Basin, Saskatchewan, Canada: An Atypical Basement-Hosted Unconformity-Related Uranium Deposit, *Economic*  
1217 *Geology*, 104, 815-840, <https://doi.org/10.2113/gsecongeo.104.6.815>, 2009.

1218 Cloutier, J., Kyser, K., Olivo, G. R., and Alexandre, P.: Contrasting Patterns of Alteration at the Wheeler River  
1219 Area, Athabasca Basin, Saskatchewan, Canada: Insights into the Apparently Uranium-Barren Zone K Alteration  
1220 System, *Economic Geology*, 105, 303-324, <https://doi.org/10.2113/gsecongeo.105.2.303>, 2010.

1221 Cloutier, J., Kyser, K., Olivo, G. R., and Brisbin, D.: Geochemical, isotopic, and geochronologic constraints on  
1222 the formation of the Eagle Point basement-hosted uranium deposit, Athabasca Basin, Saskatchewan, Canada and  
1223 recent remobilization of primary uraninite in secondary structures, *Miner Deposita*, 46, 35-56,  
1224 <https://doi.org/10.1007/s00126-010-0308-5>, 2011.

1225 Corrigan, D.: Paleoproterozoic crustal evolution and tectonics processes: Insights from the LITHOPROBE  
1226 program in the Trans-Hudson orogen, Canada, *Tectonic Styles in Canada: The LITHOPROBE Perspective*, 49,  
1227 237-284, 2012.

1228 Corrigan, D., Hajnal, Z., Németh, B., and Lucas, S. B.: Tectonic framework of a Paleoproterozoic arc-continent to  
1229 continent-continent collisional zone, Trans-Hudson Orogen, from geological and seismic reflection studies, *Can.*  
1230 *J. Earth Sci.*, 42, 421-434, <https://doi.org/10.1139/e05-025>, 2005.

1231 Corrigan, D., Pehrsson, S., Wodicka, N., and De Kemp, E.: The Palaeoproterozoic Trans-Hudson Orogen: a  
1232 prototype of modern accretionary processes, *SP*, 327, 457-479, <https://doi.org/10.1144/SP327.19>, 2009.

1233 Creaser, R. and Stasiuk, L. D.: Depositional age of the Douglas formation, Northern Saskatchewan, determined by  
1234 RE-Os geochronology, *Bulletin of the Geological Survey of Canada*, 341-346, 2007.

1235 Cumming, G. L. and Krstic, D.: The age of unconformity-related uranium mineralization in the Athabasca Basin,  
1236 northern Saskatchewan, *Can. J. Earth Sci.*, 29, 1623-1639, <https://doi.org/10.1139/e92-128>, 1992.

1237 [Cuney, M. and Kyser, K.: \*Geology and geochemistry of uranium and thorium deposits, Mineralogical Association\*](#)  
1238 [of Canada, 2015.](#)

1239 DePaolo, D. J.: Trace element and isotopic effects of combined wallrock assimilation and fractional crystallization,  
1240 *Earth and Planetary Science Letters*, 53, 189-202, [https://doi.org/10.1016/0012-821X\(81\)90153-9](https://doi.org/10.1016/0012-821X(81)90153-9), 1981.

1241 Derome, D., Cathelineau, M., Cuney, M., Fabre, C., Lhomme, T., and Banks, D. A.: Mixing of Sodic and Calcic  
1242 Brines and Uranium Deposition at McArthur River, Saskatchewan, Canada: A Raman and Laser-Induced  
1243 Breakdown Spectroscopic Study of Fluid Inclusions, *Economic Geology*, 100, 1529-1545,  
1244 <https://doi.org/10.2113/gsecongeo.100.8.1529>, 2005.

1245 Davis, W., Gall, Q., Jefferson, C. W., and Rainbird, R.: Fluorapatite in the Paleoproterozoic Thelon Basin:  
1246 Structural-stratigraphic context, in situ ion microprobe U-Pb ages, and fluid-flow history, *Geological Society of*  
1247 *America Bulletin*, 123, 1056-1073, <https://doi.org/10.1130/B30163.1>, 2011.

1248 Dickin, A. P.: *Radiogenic Isotope Geology*, 3rd ed., Cambridge University Press,  
1249 <https://doi.org/10.1017/9781316163009>, 2018.

1250 Dodson, M. H.: Closure temperature in cooling geochronological and petrological systems, *Contr. Mineral. and*  
1251 *Petrol.*, 40, 259-274, <https://doi.org/10.1007/BF00373790>, 1973.

1252 Drake, H., Tillberg, M., Reinhardt, M., Whitehouse, M. J., and Kooijman, E.: In Situ Rb/Sr Geochronology and  
1253 Stable Isotope Geochemistry Evidence for Neoproterozoic and Paleozoic Fracture-Hosted Fluid Flow and  
1254 Microbial Activity in Paleoproterozoic Basement, SW Sweden, *Geochem Geophys Geosyst*, 24, e2023GC010892,  
1255 <https://doi.org/10.1029/2023GC010892>, 2023.

1256 Eberlei, T., Habler, G., Wegner, W., Schuster, R., Körner, W., Thöni, M., and Abart, R.: Rb/Sr isotopic and  
1257 compositional retentivity of muscovite during deformation, *Lithos*, 227, 161-178,  
1258 <https://doi.org/10.1016/j.lithos.2015.04.007>, 2015.

1259 Eisele, J. and Isachsen, C. E.: Crustal Growth in Southern Arizona: U–Pb Geochronologic and Sm-Nd Isotopic  
1260 Evidence for Addition of the Paleoproterozoic Cochise Block to the Mazatzal Province, *American Journal of*  
1261 *Science*, 301, 773-797, <https://doi.org/10.2475/ajs.301.9.773>, 2001.

1262 Etheridge, M. A., Wall, V. J., and Vernon, R. H.: The role of the fluid phase during regional metamorphism and  
1263 deformation, *Journal Metamorphic Geology*, 1, 205-226, <https://doi.org/10.1111/j.1525-1314.1983.tb00272.x>,  
1264 1983.

1265 Evans, J., MILLAR, I., and NOBLE, S.: Hydration during uplift is recorded by reset Rb–Sr whole-rock ages,  
1266 *Journal of The Geological Society - J GEOL SOC*, 152, 209-212, <https://doi.org/10.1144/gsjgs.152.2.0209>, 1995.

1267 Faulkner, D. R., Jackson, C. A. L., Lunn, R. J., Schlische, R. W., Shipton, Z. K., Wibberley, C. A. J., and Withjack,  
1268 M. O.: A review of recent developments concerning the structure, mechanics and fluid flow properties of fault  
1269 zones, *Journal of Structural Geology*, 32, 1557-1575, <https://doi.org/10.1016/j.jsg.2010.06.009>, 2010.

1270 Faure, G., Mensing, T. M., and Faure, G.: *Isotopes: principles and applications*, Third edition., John Wiley & Sons,  
1271 Inc, Hoboken, New Jersey, 897 pp., 2013.

1272 Fayek, M. and Kyser, T. K.: Characterization of multiple fluid-flow events and rare-earth-element mobility  
1273 associated with formation of unconformity-type uranium deposits in the Athabasca Basin, Saskatchewan, *The*  
1274 *Canadian Mineralogist*, 35, 627-658, 1997.

1275 Fayek, M., Harrison, T. M., Ewing, R. C., Grove, M., and Coath, C. D.: O and Pb isotopic analyses of uranium  
1276 minerals by ion microprobe and U–Pb ages from the Cigar Lake deposit, *Chemical Geology*, 185, 205-225,  
1277 [https://doi.org/10.1016/S0009-2541\(01\)00401-6](https://doi.org/10.1016/S0009-2541(01)00401-6), ~~2002a~~2002.

1278 Fayek, M., ~~Kyser, T. K.,~~ and Riciputi, L. R.: U AND Pb ISOTOPE ANALYSIS OF URANIUM MINERALS  
1279 BY ION MICROPROBE AND THE GEOCHRONOLOGY OF THE McARTHUR RIVER AND SUE ZONE  
1280 URANIUM DEPOSITS, SASKATCHEWAN, CANADA, ~~The isotope analysis of uranium minerals by ion~~  
1281 ~~microprobe and the geochronology of McArthur River and Sue Zone uranium deposits, Saskatchewan, Canada,~~  
1282 *Canadian Mineralogist*, 40, 1553-~~1570~~1569, <https://doi.org/10.2113/gscanmin.40.6.1553>, ~~2002b~~2002.

1283 Fraley, C. and Raftery, A. E.: Model-Based Clustering, Discriminant Analysis, and Density Estimation, *Journal of*  
1284 *the American Statistical Association*, 97, 611-631, <https://doi.org/10.1198/016214502760047131>, 2002.

1285 Frey, M., Bossennec, C., Seib, L., Bär, K., Schill, E., and Sass, I.: Interdisciplinary fracture network  
1286 characterization in the crystalline basement: a case study from the Southern Odenwald, SW Germany, *Solid Earth*,  
1287 13, 935-955, <https://doi.org/10.5194/se-13-935-2022>, 2022.

1288 Furlanetto, F., Thorkelson, D. J., Daniel Gibson, H., Marshall, D. D., Rainbird, R. H., Davis, W. J., Crowley, J. L.,  
1289 and Vervoort, J. D.: Late Paleoproterozoic terrane accretion in northwestern Canada and the case for circum-  
1290 Columbian orogenesis, *Precambrian Research*, 224, 512-528, <https://doi.org/10.1016/j.precamres.2012.10.010>,  
1291 2013.

1292 Furlanetto, F., Thorkelson, D. J., Rainbird, R. H., Davis, W. J., Gibson, H. D., and Marshall, D. D.: The  
1293 Paleoproterozoic Wernecke Supergroup of Yukon, Canada: Relationships to orogeny in northwestern Laurentia  
1294 and basins in North America, East Australia, and China, *Gondwana Research*, 39, 14-40,  
1295 <https://doi.org/10.1016/j.gr.2016.06.007>, 2016.

1296 Galbraith, R. F.: Graphical Display of Estimates Having Differing Standard Errors, *Technometrics*, 30, 271-281,  
1297 <https://doi.org/10.2307/1270081>, 1988.

1298 Galbraith, R. F.: The radial plot: Graphical assessment of spread in ages, *International Journal of Radiation*  
1299 *Applications and Instrumentation. Part D. Nuclear Tracks and Radiation Measurements*, 17, 207-214,  
1300 [https://doi.org/10.1016/1359-0189\(90\)90036-W](https://doi.org/10.1016/1359-0189(90)90036-W), 1990.

1301 Gerardin, M., Milesi, G., Mercadier, J., Cathelineau, M., and Bartier, D.: Development of an integrated analytical  
1302 platform for clay mineral separation, characterization and K-Ar dating, *Geoscientific Instrumentation, Methods*  
1303 *and Data Systems*, 13, 309-323, <https://doi.org/10.5194/gi-13-309-2024>, 2024.

1304 Glodny, J. and Grauert\*, B.: Evolution of a hydrothermal fluid-rock interaction system as recorded by Sr isotopes:  
1305 A case study from the Schwarzwald, SW Germany, *Miner Petrol*, 95, 163-178, [https://doi.org/10.1007/s00710-](https://doi.org/10.1007/s00710-008-0034-1)  
1306 [008-0034-1](https://doi.org/10.1007/s00710-008-0034-1), 2009.

1307 Glodek, M., Schels, M., and Schwenker, F.: Ensemble Gaussian mixture models for probability density estimation,  
1308 *Comput Stat*, 28, 127-138, <https://doi.org/10.1007/s00180-012-0374-5>, 2013.

1309 [Glorie, S., Gilbert, S. E., Hand, M., and Lloyd, J. C.: Calibration methods for laser ablation Rb-Sr geochronology:  
1310 comparisons and recommendation based on NIST glass and natural reference materials, \*Geochronology\*, 6, 21-36,  
1311 <https://doi.org/10.5194/gchron-6-21-2024>, 2024.](https://doi.org/10.5194/gchron-6-21-2024)

1312 Grand'Homme, A., Janots, E., Bosse, V., Seydoux-Guillaume, A. M., and De Ascensão Guedes, R.: Interpretation  
1313 of U-Th-Pb in-situ ages of hydrothermal monazite-(Ce) and xenotime-(Y): evidence from a large-scale regional  
1314 study in clefts from the western alps, *Miner Petrol*, 110, 787-807, <https://doi.org/10.1007/s00710-016-0451-5>,  
1315 2016.

1316 [Guillou-Frottier, L., Milesi, G., Roche, V., Duwiquet, H., and Taillefer, A.: Heat flow, thermal anomalies, tectonic  
1317 regimes and high temperature geothermal systems in fault zones, \*Comptes Rendus. Géoscience\*, 356, 389-421,  
1318 <https://doi.org/10.5802/ergos.213>, 2024.](https://doi.org/10.5802/ergos.213)

- 1319 Gyomlai, T., Agard, P., Herviou, C., Jolivet, L., Monié, P., Mendes, K., and Iemmolo, A.: In situ Rb–Sr and 40Ar-  
1320 39Ar dating of distinct mica generations in the exhumed subduction complex of the Western Alps, *Contrib Mineral*  
1321 *Petrol*, 178, 58, <https://doi.org/10.1007/s00410-023-02042-8>, 2023.
- 1322 Halter, G.: Zonalite des alterations dans l'environnement des gisements d'uranium associés à la discordance du  
1323 proterozoïque moyen (saskatchewan, canada), These de doctorat, Université Louis Pasteur (Strasbourg) (1971-  
1324 2008), 1988.
- 1325 Hastie, T., Friedman, J., and Tibshirani, R.: *The Elements of Statistical Learning*, Springer New York, New York,  
1326 NY, <https://doi.org/10.1007/978-0-387-21606-5>, 2001.
- 1327 Hobson, G. D., Canada, G. S. of, and MacAulay, H. A.: A Seismic Reconnaissance Survey of the Athabasca  
1328 Formation, Alberta and Saskatchewan (part of 74), Department of Energy, Mines and Resources, 36 pp., 1969.
- 1329 Hoeve, J. and Sibbald, T. I. I.: On the genesis of Rabbit Lake and other unconformity-type uranium deposits in  
1330 northern Saskatchewan, Canada, *Economic Geology*, 73, 1450-1473,  
1331 <https://doi.org/10.2113/gsecongeo.73.8.1450>, 1978.
- 1332 Hogmalm, K. J., Zack, T., Karlsson, A. K.-O., Sjöqvist, A. S. L., and Garbe-Schönberg, D.: In situ Rb–Sr and K-  
1333 Ca dating by LA-ICP-MS/MS: an evaluation of N<sub>2</sub>O and SF<sub>6</sub> as reaction gases, *J. Anal. At. Spectrom.*, 32, 305-  
1334 313, <https://doi.org/10.1039/C6JA00362A>, 2017.
- 1335 Holness, M.: PARNELL, J. (ed.) 1998. *Dating and Duration of Fluid Flow and Fluid-Rock Interaction*. Geological  
1336 Society Special Publication no. 144. vi+284 pp. Price £69.00, US \$115.00 (hard covers); members' price £35.00,  
1337 US \$58.00. ISBN 1 86239 019 3. -, *Geological Magazine*, 137, 705-712,  
1338 <https://doi.org/10.1017/S0016756800274736>, 2000.
- 1339 Huang, C., Wang, H., Xie, L., Xu, L., Wu, S., Yang, Y., and Yang, J.: High-precision Rb–Sr isotope analysis with  
1340 Neoma MS/MS: Enhancing in situ geochronology by laser ablation, *Spectrochimica Acta Part B: Atomic*  
1341 *Spectroscopy*, 224, 107117, <https://doi.org/10.1016/j.sab.2025.107117>, 2025.
- 1342 Huang, Y., Qi, X., Wu, Q., Li, J., Ren, M., Duan, L., Xiong, T., Yang, Z., Zhao, Y., Ciren, L., Wei, W., Duan, J.,  
1343 and Yan, M.: In Situ Rb-Sr Dates of Muscovite and Sulfur Isotope of Pyrite from the Yangshan Gold Deposit in  
1344 Western Qinling, China, *Acta Geologica Sinica (Eng)*, 97, 1475-1489, <https://doi.org/10.1111/1755-6724.15091>,  
1345 2023.
- 1346 Hueck, M., Wemmer, K., Ksienzyk, A. K., Kuehn, R., and Vogel, N.: Potential, premises, and pitfalls of interpreting  
1347 illite argon dates - A case study from the German Variscides, *Earth-Science Reviews*, 232, 104133,  
1348 <https://doi.org/10.1016/j.earscirev.2022.104133>, 2022.
- 1349 Jeanneret, P., Goncalves, P., Durand, C., [Trap, P., Marquer, D., Quirt, D., and Ledru, P.: Tectono-metamorphic](#)  
1350 [evolution of the pre-Athabasca basement within the Wollaston–Mudjatik Transition Zone, Saskatchewan, \*Can. J.\*](#)  
1351 [Earth Sci., 53, 231–259, <https://doi.org/10.1139/cjes-2015-0136>, 2016.](#)
- 1352 [Jeanneret, P., Goncalves, P., Durand, C., Poujol, M., Trap, P., Marquer, D., Quirt, D., and Ledru, P.:](#)  
1353 [Geochronological constraints on the trans-Hudsonian tectono-metamorphic evolution of the pre-Athabasca](#)

1354 basement within the Wollaston-Mudjatik Transition Zone, Saskatchewan, Precambrian Research, 301, 152-178,  
1355 <https://doi.org/10.1016/j.precamres.2017.07.019>, 2017.

1356 Jefferson, C. W., Thomas, D. J., Gandhi, S. S., Ramaekers, P., Delaney, G., Brisbin, D., Cutts, C., Portella, P., and  
1357 Olson, R. A.: Unconformity-associated uranium deposits of the Athabasca Basin, Saskatchewan and Alberta,  
1358 <https://doi.org/10.4095/223744>, [2007e2007](https://doi.org/10.4095/223744).

1359 Jegal, Y., Zimmermann, C., Reisberg, L., Yeghicheyan, D., Cloquet, C., Peiffert, C., Gerardin, M., Deloule, E., and  
1360 Mercadier, J.: Characterisation of Reference Materials for In Situ Rb-Sr Dating by LA-ICP-MS / MS, Geostandard  
1361 Geoanalytic Res, 46, 645-671, <https://doi.org/10.1111/ggr.12456>, 2022.

1362 Jenkin, G. R. T., Ellam, R. M., Rogers, G., and Stuart, F. M.: An investigation of closure temperature of the biotite  
1363 Rb–Sr system: The importance of cation exchange, Geochimica et Cosmochimica Acta, 65, 1141-1160,  
1364 [https://doi.org/10.1016/S0016-7037\(00\)00560-3](https://doi.org/10.1016/S0016-7037(00)00560-3), 2001.

1365 Juhász, A., Tóth, T. M., Ramseyer, K., and Matter, A.: Connected fluid evolution in fractured crystalline basement  
1366 and overlying sediments, Pannonian Basin, SE Hungary, Chemical Geology, 182, 91-120,  
1367 [https://doi.org/10.1016/S0009-2541\(01\)00269-8](https://doi.org/10.1016/S0009-2541(01)00269-8), 2002.

1368 Kaczowka, A. J., Kyser, T. K., Kotzer, T. G., Leybourne, M. I., and Layton-Matthews, D.: Geometallurgical ore  
1369 characterization of the high-grade polymetallic unconformity-related uranium deposit, The Canadian Mineralogist,  
1370 59, 813-845, <https://doi.org/10.3749/canmin.2000050>, 2021.

1371 Kalt, A., Grauert, B., and Baumann, A.: Rb-Sr and U-Pb isotope studies on migmatites from the Schwarzwald  
1372 (Germany): constraints on isotopic resetting during Variscan high-temperature metamorphism, Journal  
1373 Metamorphic Geology, 12, 667-680, <https://doi.org/10.1111/j.1525-1314.1994.tb00050.x>, 1994.

1374 Karlstrom, K.: [Refining Rodinia: Geologic Evidence for the Australia–Western U.S. connection in the Proterozoic,](https://doi.org/10.1130/GSAT-1999-10-01-science)  
1375 [GSAT, 9, 1–7](https://doi.org/10.1130/GSAT-1999-10-01-science), <https://doi.org/10.1130/GSAT-1999-10-01-science>, 1999. E. and Bowring, S. A.: [Early Proterozoic](https://doi.org/10.1016/S0016-7037(94)00114-N)  
1376 [Assembly of Tectonostratigraphic Terranes in Southwestern North America. J. Geol., 96, 561-576, 1988.](https://doi.org/10.1016/S0016-7037(94)00114-N)

1377 Kister, P.: Mobilité des éléments géochimiques dans un bassin sédimentaire clastique, du Protérozoïque à nos  
1378 jours : le bassin Athabasca (Saskatchewan, Canada), phdthesis, Institut National Polytechnique de Lorraine, 2003.

1379 Kister, P., Vieillard, P., Cuney, M., Quirt, D., and Laverret, E.: Thermodynamic constraints on the mineralogical  
1380 and fluid composition evolution in a clastic sedimentary basin: the Athabasca Basin (Saskatchewan, Canada), ejm,  
1381 17, 325-341, <https://doi.org/10.1127/0935-1221/2005/0017-0325>, 2005.

1382 Kohn, M.: Titanite Petrochronology, Reviews in Mineralogy and Geochemistry, 2017.

1383 Kotzer, T. G. and Kyser, T. K.: Fluid history of the Athabasca Basin and its relation to uranium deposits.  
1384 Saskatchewan Energy and Mines, Saskatchewan Geological Survey Miscellaneous Report, 90, 153-157, 1990.

1385 Kotzer, T. G. and Kyser, T. K.: Petrogenesis of the Proterozoic Athabasca Basin, northern Saskatchewan, Canada,  
1386 and its relation to diagenesis, hydrothermal uranium mineralization and paleohydrogeology, Chemical Geology,  
1387 120, 45-89, [https://doi.org/10.1016/0009-2541\(94\)00114-N](https://doi.org/10.1016/0009-2541(94)00114-N), 1995.

1388 Kyser, K., ~~Hiatt, E., Renac, C., Durocher, K., Holk, G., and Deckart, K.: Diagenetic fluids in Paleo-~~Cuney, M.:  
1389 ~~Basins and uranium deposits, In: Geology and Geochemistry of Uranium and Thorium Deposits, Short Course~~  
1390 ~~Series, 46, pp. 224-250, 2015~~and Meso-Proterozoic sedimentary basins and their implications for long protracted  
1391 ~~fluid histories, Mineralogical Association of Canada Short Course, 28, 225-262, 2000.~~

1392 Kyser, K., Lahusen, L., Drever, G., Dunn, C., Leduc, E., and Chipley, D.: Using Pb isotopes in surface media to  
1393 distinguish anthropogenic sources from undercover uranium sources, *Comptes Rendus. Géoscience*, 347, 215-226,  
1394 2015.

1395 ~~Kyser, K., Hiatt, E., Renac, C., Durocher, K., Holk, G., and Deckart, K.: Diagenetic fluids in Paleo- and Meso-~~  
1396 ~~Proterozoic sedimentary basins and their implications for long protracted fluid histories.,~~  
1397 ~~<https://doi.org/10.13140/2.1.1033.1847>, 2005.~~

1398 ~~Lacombe, O., Tavani, S., Lamarche, J., Balsamo, F., and Agosta, F.: Introduction: Faults and fractures in rocks:~~  
1399 ~~mechanics, occurrence, dating, stress history and fluid flow, *Geol. Mag.*, 159, 1847-1854,~~  
1400 ~~<https://doi.org/10.1017/S0016756823000031>, 2022.~~

1401 Larsen, R. T. and Sundvoll: Rb-Sr isotope systematics In the magmatic rocks of the Oslo Rift, 2008.

1402 ~~Laverret, E., Clauer, N., Falliek, A., Patrier-Mas, P., Beaufort, D., Quirt, D., Kister, P., and Bruneton, P.: K-Ar~~  
1403 ~~dating and stable isotope tracing of illite associated with the Sea Creek unconformity type uranium deposits~~  
1404 ~~(Athabasca Basin, Canada), in: "Bridging Clays" Joint meeting CMS/GFA, Oléron, France, 164, 2006.~~

1405 Liebmann, J., Kirkland, C. L., Kelsey, D. E., Korhonen, F. J., and Rankenburg, K.: Lithological fabric as a proxy  
1406 for Rb-Sr isotopic complexity, *Chemical Geology*, 608, 121041, <https://doi.org/10.1016/j.chemgeo.2022.121041>,  
1407 2022.

1408 Liu, W., Zhang, X., Zhang, J., and Jiang, M.: Sphalerite Rb-Sr Dating and in situ Sulfur Isotope Analysis of the  
1409 Daliangzi Lead-Zinc Deposit in Sichuan Province, SW China, *J. Earth Sci.*, 29, 573-586,  
1410 <https://doi.org/10.1007/s12583-018-0785-5>, 2018.

1411 Macdonald, C. C.: Mineralogy and geochemistry of a precambrian regolith in the Athabasca Basin, 1980.

1412 Mao, G., Hua, R., Long, G., and Lu, H.: Rb-Sr Dating of Pyrite and Quartz Fluid Inclusions and Origin of Ore-  
1413 forming Materials of the Jinshan Gold Deposit, Northeast Jiangxi Province, South China, *Acta Geologica Sinica*  
1414 (Eng), 87, 1658-1667, <https://doi.org/10.1111/1755-6724.12166>, 2013.

1415 McLachlan, G. and Peel, D.: Finite Mixture Models, 1st ed., Wiley, <https://doi.org/10.1002/0471721182>, 2000.

1416 Martz, P.: Caractéristiques, chronologie et rôles des circulations fluides dans le bassin d'Athabasca et son socle :  
1417 implications dans la formation et l'évolution du gisement d'uranium de Cigar Lake, These de doctorat, Université  
1418 de Lorraine, 2017.

1419 Martz, P., Mercadier, J., Cathelineau, M., Boiron, M.-C., Quirt, D., Doney, A., Gerbeaud, O., De Wally, E., and  
1420 Ledru, P.: Formation of U-rich mineralizing fluids through basinal brine migration within basement-hosted shear  
1421 zones: A large-scale study of the fluid chemistry around the unconformity-related Cigar Lake U deposit

1422 (Saskatchewan, Canada), *Chemical Geology*, 508, 116-143, <https://doi.org/10.1016/j.chemgeo.2018.05.042>,  
1423 2019a.

1424 Martz, P., Mercadier, J., Perret, J., Villeneuve, J., Delouie, E., Cathelineau, M., Quirt, D., Doney, A., and Ledru,  
1425 P.: Post-crystallization alteration of natural uraninites: Implications for dating, tracing, and nuclear forensics,  
1426 *Geochimica et Cosmochimica Acta*, 249, 138-159, <https://doi.org/10.1016/j.gca.2019.01.025>, 2019b.

1427 Matheny, R. K., Brookins, D. G., Wallin, E. T., Shafiqullah, M., and Damon, P. E.: Incompletely reset Rb · Sr  
1428 systems from a Cambrian red-rock granophyre terrane, Florida Mountains, New Mexico, U.S.A., *Chemical*  
1429 *Geology: Isotope Geoscience section*, 86, 29-47, [https://doi.org/10.1016/0168-9622\(90\)90004-V](https://doi.org/10.1016/0168-9622(90)90004-V), 1990.

1430 Melnykov, V. and Melnykov, I.: Initializing the EM algorithm in Gaussian mixture models with an unknown  
1431 number of components, *Computational Statistics & Data Analysis*, 56, 1381-1395,  
1432 <https://doi.org/10.1016/j.csda.2011.11.002>, 2012.

1433 Mcfarlane, C. and Markharrison, T.: Pb-diffusion in monazite: Constraints from a high-T contact aureole setting,  
1434 *Earth and Planetary Science Letters*, 250, 376–384, <https://doi.org/10.1016/j.epsl.2006.06.050>, 2006.

1435 McGill ~~BD~~, B. D., Marlat ~~HL~~, J. L., Matthews ~~RB~~, R. B., Sopuck ~~VJ~~, V. J., Homeniuk ~~LA~~, L. A., and Hubregtse  
1436 ~~H~~, J. J.: The P2 North uranium deposit, Saskatchewan, Canada, *Explor. Min. Geol.*, 2(4), 321–331, 1993.

1437 McLachlan, G. J., Lee, S. X., and Rathnayake, S. I.: Finite Mixture Models, *Annual Review of Statistics and Its*  
1438 *Application*, 6, 355-378, <https://doi.org/10.1146/annurev-statistics-031017-100325>, 2019.

1439 Menier, A., Roy, R., Harrison, G., Zerff, R. W., and Kinar, D.: Relationship between rock physical properties and  
1440 spectral mineralogy applied to exploration for an unconformity-related uranium deposit (Saskatchewan, Canada),  
1441 *Can. J. Earth Sci.*, 57, 1349-1364, <https://doi.org/10.1139/cjes-2019-0080>, 2020.

1442 Mercadier, J., Cuney, M., Cathelineau, M., and Lacorde, M.: U redox fronts and kaolinisation in basement-hosted  
1443 unconformity-related U ores of the Athabasca Basin (Canada): late U remobilisation by meteoric fluids, *Miner*  
1444 *Deposita*, 46, 105-135, <https://doi.org/10.1007/s00126-010-0314-7>, 2011.

1445 Mercadier, J., Richard, A., and Cathelineau, M.: Boron- and magnesium-rich marine brines at the origin of giant  
1446 unconformity-related uranium deposits:  $\delta^{11}\text{B}$  evidence from Mg-tourmalines, *Geology*, 40, 231-234,  
1447 <https://doi.org/10.1130/G32509.1>, 2012.

1448 Młynarska, M., Barnes, C. J., Zack, T., Majka, J., and Mazur, S.: In situ white mica Rb/Sr geochronology of the  
1449 Leszczyniec metaigneous complex, West Sudetes: evidence of upper plate deformation at the onset of Variscan  
1450 collision, *Int J Earth Sci (Geol Rundsch)*, 113, 319-333, <https://doi.org/10.1007/s00531-023-02373-8>, 2024.

1451 Muñoz-Montecinos, J., Giuliani, A., Oesch, S., Volante, S., Peters, B., and Behr, W.: In situ rubidium-strontium  
1452 geochronology of white mica in young metamafic and metasomatic rocks from Syros: testing the limits of laser-  
1453 ablation triple-quadrupole inductively coupled plasma mass spectrometer mica dating using different anchoring  
1454 approaches, *Geochronology*, 6, 585-605, <https://doi.org/10.5194/gchron-6-585-2024>, 2024.

1455 Ng, R., Alexandre, P., Kyser, K., Cloutier, J., Abdu, Y. A., and Hawthorne, F. C.: Oxidation state of iron in alteration  
1456 minerals associated with sandstone-hosted unconformity-related uranium deposits and apparently barren alteration

1457 systems in the Athabasca Basin, Canada: Implications for exploration, *Journal of Geochemical Exploration*, 130,  
1458 22-43, <https://doi.org/10.1016/j.gexplo.2013.02.009>, 2013.

1459 Nguyen, H. and McLachlan, G.: Maximum likelihood estimation of Gaussian mixture models without matrix  
1460 operations, *Advances in Data Analysis and Classification*, 9, <https://doi.org/10.1007/s11634-015-0209-7>, 2015.

1461 Obin, T.: Mobilités du carbone et du soufre dans l'environnement du Bassin de l'Athabasca (Saskatchewan,  
1462 Canada) et impact(s) sur la formation des gisements d'uranium de type discordance, Thèse de doctorat, Université  
1463 de Lorraine, 2025.

1464 Olierook, H. K. H., Rankenburg, K., Ulrich, S., Kirkland, C. L., Evans, N. J., Brown, S., McInnes, B. I. A., Prent,  
1465 A., Gillespie, J., McDonald, B., and Darragh, M.: Resolving multiple geological events using in situ Rb—Sr  
1466 geochronology: implications for metallogenesis at Tropicana, Western Australia, *Geochronology*, 2, 283-303,  
1467 <https://doi.org/10.5194/gchron-2-283-2020>, 2020.

1468 Oummouch, A., Essaifi, A., Zayane, R., Maddi, O., Zouhair, M., and Maacha, L.: Geology and Metallogenesis of  
1469 the Sediment-Hosted Cu-Ag Deposit of Tizert (Igherm Inlier, Anti-Atlas Copperbelt, Morocco), *Geofluids*, 2017,  
1470 7508484, <https://doi.org/10.1155/2017/7508484>, 2017.

1471 Pacquet, A. and Weber, F.: Pétrographie et minéralogie des halos d'altération autour du gisement de Cigar Lake et  
1472 leurs relations avec les minéralisations, *Can. J. Earth Sci.*, 30, 674-688, <https://doi.org/10.1139/e93-055>, 1993.

1473 [Pagel, M.: Cadre géologique des gisements d'uranium dans la structure de Carswell \(Saskatchewan, Canada\).  
1474 Etudes des phases fluides. Thèse de 3ème cycle, Université de Nancy, Nancy, France, 1975a.](#)

1475 [Pagel, M.: Détermination des conditions physico-chimiques de la silicification diagénétique des grès Athabasca  
1476 \(Canada\) au moyen des inclusions fluides. \*Comptes Rendus Académie Sci. Paris, Série D\*, 280, 2301–2304, 1975b.](#)

1477 Paton, C., Hellstrom, J., Paul, B., Woodhead, J., and Hergt, J.: Iolite: Freeware for the visualisation and processing  
1478 of mass spectrometric data, *J. Anal. At. Spectrom.*, 26, 2508-2518, <https://doi.org/10.1039/C1JA10172B>, 2011.

1479 Pehrsson, S., Eglinton, B., Rainbird, R., Regis, D., Ramaekers, P., and Jefferson, C.: Extent and significance of  
1480 the Racklan-Forward Orogen in Canada: far-field interior reactivation during Nuna assembly, *SP*, 531, 47-75,  
1481 <https://doi.org/10.1144/SP531-2022-307>, 2023.

1482 Percival, J. B. and Kodama, H.: Sudoite from cigar lake, Saskatchewan, *The Canadian Mineralogist*, 27, 633-641,  
1483 1989.

1484 Philippe, S., Lancelot, J. R., Clauer, N., and Pacquet, A.: Formation and evolution of the Cigar Lake uranium  
1485 deposit based on U—Pb and K—Ar isotope systematics, *Can. J. Earth Sci.*, 30, 720-730,  
1486 <https://doi.org/10.1139/e93-058>, 1993.

1487 Powell, J. W., Percival, J. B., Potter, E. G., Van Der Lelij, R., and Xie, R.: Mineralogy and K—Ar geochronology  
1488 of clay alteration associated with uranium mineralization in the Patterson Lake Corridor, Saskatchewan, *GEEA*,  
1489 22, [geochem2021-061](https://doi.org/10.1144/geochem2021-061), <https://doi.org/10.1144/geochem2021-061>, 2022.

1490 [Qiu, E., Larson, K. P., Camacho, A., and Zhang, Y.: Reassessing the timing of high-strain deformation in the](#)  
1491 [Strangways Metamorphic Complex, Central Australia, by in situ mica Rb–Sr and titanite U–Pb geochronology,](#)  
1492 [JGS. 181, jgs2023-163, <https://doi.org/10.1144/jgs2023-163>, 2024.](#)

1493 Rabiei, M., Chi, G., Normand, C., Davis, W. J., Fayek, M., and Blamey, N. J. F.: Hydrothermal Rare Earth Element  
1494 (Xenotime) Mineralization at Maw Zone, Athabasca Basin, Canada, and Its Relationship to Unconformity-Related  
1495 Uranium Deposits, *Economic Geology*, 112, 1483-1507, <https://doi.org/10.5382/econgeo.2017.4518>, 2017.

1496 Rainbird, R. H., Stern, R. A., Rayner, N., Jefferson, C. W., and Delaney, G.: Age, provenance, and regional  
1497 correlation of the Athabasca Group, Saskatchewan and Alberta, constrained by igneous and detrital zircon  
1498 geochronology, *Bulletin-Geological Survey of Canada*, 588, 193, 2007.

1499 Ramaekers, P., Jefferson, C. W., Yeo, G. M., Collier, B., Long, D. G. F., Drever, G., McHardy, S., Jiricka, D., Cutts,  
1500 C., and Wheatley, K.: Revised geological map and stratigraphy of the Athabasca Group, Saskatchewan and Alberta,  
1501 *Bulletin-Geological Survey of Canada*, 588, 155, 2007.

1502 Rasmussen, B., Fletcher, I. R., and McNaughton, N. J.: Dating low-grade metamorphic events by SHRIMP U–Pb  
1503 analysis of monazite in shales, *Geol*, 29, 963, [https://doi.org/10.1130/0091-7613\(2001\)029](https://doi.org/10.1130/0091-7613(2001)029)  
1504 [%253C0963:DLGMEB %253E2.0.CO;2](https://doi.org/10.1130/0091-7613(2001)029%253C0963:DLGMEB%253E2.0.CO;2), 2001.

1505 Rasmussen, B., Sheppard, S., and Fletcher, I. R.: Testing ore deposit models using in situ U–Pb geochronology  
1506 of hydrothermal monazite: Paleoproterozoic gold mineralization in northern Australia, *Geology*, 34, 77-80,  
1507 <https://doi.org/10.1130/G22058.1>, 2006.

1508 Rasmussen, B., Zi, J.-W., and Muhling, J. R.: Tectonic fluid expulsion: U–Pb evidence for punctuated  
1509 hydrothermal fluid flow and hydraulic fracturing during orogenesis, *Earth and Planetary Science Letters*, 604,  
1510 117997, <https://doi.org/10.1016/j.epsl.2023.117997>, 2023.

1511 Redaa, A., Farkaš, J., Gilbert, S., Collins, A. S., Wade, B., Löhr, S., Zack, T., and Garbe-Schönberg, D.: Assessment  
1512 of elemental fractionation and matrix effects during in situ Rb–Sr dating of phlogopite by LA-ICP-MS/MS:  
1513 implications for the accuracy and precision of mineral ages, *J. Anal. At. Spectrom.*, 36, 322-344,  
1514 <https://doi.org/10.1039/DOJA00299B>, 2021.

1515 Redaa, A., Farkaš, J., Hassan, A., Collins, A. S., Gilbert, S., and Löhr, S. C.: Constraints from in-situ Rb–Sr dating  
1516 on the timing of tectono-thermal events in the Umm Farwah shear zone and associated Cu-Au mineralisation in  
1517 the Southern Arabian Shield, Saudi Arabia, *Journal of Asian Earth Sciences*, 224, 105037,  
1518 <https://doi.org/10.1016/j.jseae.2021.105037>, 2022.

1519 Reynolds, R. C. and Thomson, C. H.: Illite from the Potsdam Sandstone of New York: A Probable  
1520 Noncentrosymmetric Mica Structure, *Clays and clay miner.*, 41, 66-72,  
1521 <https://doi.org/10.1346/CCMN.1993.0410107>, 1993.

1522 Ribeiro, B. V., Kirkland, C. L., Finch, M. A., Faleiros, F. M., Reddy, S. M., Rickard, W. D. A., and Hartnady, M.  
1523 I. H.: Microstructures, geochemistry, and geochronology of mica fish: Review and advances, *Journal of Structural*  
1524 *Geology*, 175, 104947, <https://doi.org/10.1016/j.jsg.2023.104947>, 2023a.

1525 Ribeiro, B. V., Kirkland, C. L., Kelsey, D. E., Reddy, S. M., Hartnady, M. I. H., Faleiros, F. M., Rankenburg, K.,  
1526 Liebmann, J., Korhonen, F. J., and Clark, C.: Time-strain evolution of shear zones from petrographically  
1527 constrained Rb–Sr muscovite analysis, *Earth and Planetary Science Letters*, 602, 117969,  
1528 <https://doi.org/10.1016/j.epsl.2022.117969>, 2023b.

1529 Richard, A., Banks, D. A., Mercadier, J., Boiron, M.-C., Cuney, M., and Cathelineau, M.: An evaporated seawater  
1530 origin for the ore-forming brines in unconformity-related uranium deposits (Athabasca Basin, Canada): Cl/Br and  
1531  $\delta^{37}\text{Cl}$  analysis of fluid inclusions, *Geochimica et Cosmochimica Acta*, 75, 2792-2810,  
1532 <https://doi.org/10.1016/j.gca.2011.02.026>, 2011.

1533 Richard, A., Cauzid, J., Cathelineau, M., Boiron, M. -C., Mercadier, J., and Cuney, M.: Synchrotron XRF and  
1534 XANES investigation of uranium speciation and element distribution in fluid inclusions from unconformity-related  
1535 uranium deposits, *Geofluids*, 13, 101-111, <https://doi.org/10.1111/gfl.12009>, 2013.

1536 Richard, A., Montel, J.-M., Leborgne, R., Peiffert, C., Cuney, M., and Cathelineau, M.: Monazite Alteration in  
1537  $\text{H}_2\text{O} \pm \text{HCl} \pm \text{NaCl} \pm \text{CaCl}_2$  Fluids at 150 °C and psat: Implications for Uranium Deposits, *Minerals*, 5, 693-706,  
1538 <https://doi.org/10.3390/min5040518>, 2015.

1539 Rösel, D. and Zack, T.: LA-ICP-MS/MS Single-Spot Rb-Sr Dating, *Geostandard Geoanalytic Res*, 46, 143-168,  
1540 <https://doi.org/10.1111/ggr.12414>, 2022.

1541 Saito, T., Qiu, H.-N., Shibuya, T., Li, Y.-B., Kitajima, K., Yamamoto, S., Ueda, H., Komiya, T., and Maruyama,  
1542 S.: Ar–Ar dating for hydrothermal quartz from the 2.4 Ga Ongeluk Formation, South Africa: implications for  
1543 seafloor hydrothermal circulation, *R Soc Open Sci*, 5, 180260, <https://doi.org/10.1098/rsos.180260>, 2018.

1544 Schneider, D. A., Heizler, M. T., Bickford, M. E., Wortman, G. L., Condie, K. C., and Perilli, S.: Timing constraints  
1545 of orogeny to cratonization: Thermochronology of the Paleoproterozoic Trans-Hudson orogen, Manitoba and  
1546 Saskatchewan, Canada, *Precambrian Research*, 153, 65-95, <https://doi.org/10.1016/j.precamres.2006.11.007>,  
1547 2007.

1548 Scott Anderson, F., Levine, J., and Whitaker, T. J.: Rb–Sr resonance ionization geochronology of the Duluth  
1549 Gabbro: A proof of concept for in situ dating on the Moon, *Rapid Communications in Mass Spectrometry*, 29,  
1550 1457-1464, <https://doi.org/10.1002/rcm.7253>, 2015.

1551 Şengün, F., Bertrandsson Erlandsson, V., Högalm, J., and Zack, T.: In situ Rb–Sr dating of K-bearing minerals  
1552 from the orogenic Akçaabat gold deposit in the Menderes Massif, Western Anatolia, Turkey, *Journal of Asian Earth*  
1553 *Sciences*, 185, 104048, <https://doi.org/10.1016/j.jseaes.2019.104048>, 2019.

1554 Schmitz, B., Biermanns, P., Hueck, M., Wemmer, K., Schmid, S. M., Onuzi, K., Reicherter, K., and Ustaszewski,  
1555 K.: Kinematics and Age of the Orogen-Perpendicular Shkoder-Peja Normal Fault in North Albania Constrained  
1556 by Fault-Slip Data, Raman Spectroscopy and K–Ar Fault-Gouge Dating, *Tectonics*, 44, e2024TC008660,  
1557 <https://doi.org/10.1029/2024TC008660>, 2025.

1558 Skirrow, R. G., Mercadier, J., Armstrong, R., Kuske, T., and Deloule, E.: The Ranger uranium deposit, northern  
1559 Australia: Timing constraints, regional and ore-related alteration, and genetic implications for unconformity-  
1560 related mineralisation, *Ore Geology Reviews*, 76, 463-503, <https://doi.org/10.1016/j.oregeorev.2015.09.001>, 2016.

- 1561 Sibson, R. H.: Conditions for fault-valve behaviour, *SP*, 54, 15-28,  
1562 <https://doi.org/10.1144/GSL.SP.1990.054.01.02>, 1990.
- 1563 Sims, P. K. and ~~Petermar~~Peterman, Z. E.: Early Proterozoic Central Plains orogen: A major buried structure in the  
1564 north-central United States, *Geology*, 14, 488-491, [https://doi.org/10.1130/0091-7613\(1986\)14](https://doi.org/10.1130/0091-7613(1986)14)  
1565 %253C488:EPCPOA%253E2.0.CO;2, 1986.
- 1566 Skipton, D. R., St-Onge, M. R., Schneider, D. A., and McFarlane, C. R. M.: Tectonothermal Evolution of the  
1567 Middle Crust in the Trans-Hudson Orogen, Baffin Island, Canada: Evidence from Petrology and Monazite  
1568 Geochronology of Sillimanite-bearing Migmatites, *Journal of Petrology*, 57, 1437-1462,  
1569 <https://doi.org/10.1093/petrology/egw046>, 2016.
- 1570 Tian, J., Wang, J., Tian, T., Wang, L., Wang, Y., Yu, X., Zhang, W., Ren, T., and Sun, B.: In-Situ Geochemical and  
1571 Rb-Sr Dating Analysis of Sulfides from a Gold Deposit Offshore of Northern Sanshandao, Jiaodong Peninsula,  
1572 North China: Implications for Gold Mineralization, *Minerals*, 14, 456, <https://doi.org/10.3390/min14050456>,  
1573 2024.
- 1574 Tichomirowa, M., Käßner, A., Sperner, B., Lapp, M., Leonhardt, D., Linnemann, U., Münker, C., Ovtcharova, M.,  
1575 Pfänder, J. A., Schaltegger, U., Sergeev, S., von Quadt, A., and Whitehouse, M.: Dating multiply overprinted  
1576 granites: The effect of protracted magmatism and fluid flow on dating systems (zircon U-Pb: SHRIMP/SIMS,  
1577 LA-ICP-MS, CA-ID-TIMS; and Rb-Sr, Ar-Ar) - Granites from the Western Erzgebirge (Bohemian Massif,  
1578 Germany), *Chemical Geology*, 519, 11-38, <https://doi.org/10.1016/j.chemgeo.2019.04.024>, 2019.
- 1579 Tran, H., Ansdell, K., Bethune, K., Ashton, K., and Hamilton, M.: Provenance and tectonic setting of  
1580 Paleoproterozoic metasedimentary rocks along the eastern margin of Hearne craton: Constraints from SHRIMP  
1581 geochronology, Wollaston Group, Saskatchewan, Canada, *Precambrian Research*, 167, 171-185,  
1582 <https://doi.org/10.1016/j.precamres.2008.08.003>, 2008.
- 1583 Toma, J., Creaser, R. A., Card, C., Stern, R. A., Chacko, T., and Steele-MacInnis, M.: Re-Os systematics and  
1584 chronology of graphite, *Geochimica et Cosmochimica Acta*, 323, 164-182,  
1585 <https://doi.org/10.1016/j.gca.2022.02.012>, 2022.
- 1586 Toma, J., Creaser, R. A., Card, C., Pana, D., Dufrane, A., and Li, L.: Nuna supercontinent assembly linked to  
1587 carbon cycling in shear zones 1.9-1.7 billion years ago, *Nat. Geosci.*, 17, 1038-1045,  
1588 <https://doi.org/10.1038/s41561-024-01519-w>, 2024.
- 1589 Velde, B. and Christophe, R.: Smectite to illite conversion and K-AR ages, *Clay Minerals*, 31, 25-32, 1996.
- 1590 Vermeesch, P.: IsoplotR: A free and open toolbox for geochronology, *Geoscience Frontiers*, 9, 1479-1493,  
1591 <https://doi.org/10.1016/j.gsf.2018.04.001>, 2018.
- 1592 Villa, I. M.: Isotopic closure, *Terra Nova*, 10, 42-47, <https://doi.org/10.1046/j.1365-3121.1998.00156.x>, 1998.
- 1593 [Villa, I. M.: Dating deformation: the role of atomic-scale processes, \*JGS\*, 179, jgs2021-098,  
1594 <https://doi.org/10.1144/jgs2021-098>, 2022.](https://doi.org/10.1144/jgs2021-098)

1595 Viswanathan, H. S., Ajo-Franklin, J., Birkholzer, J. T., Carey, J. W., Guglielmi, Y., Hyman, J. D., Karra, S., Pyrak-  
1596 Nolte, L. J., Rajaram, H., Srinivasan, G., and Tartakovsky, D. M.: From Fluid Flow to Coupled Processes in  
1597 Fractured Rock: Recent Advances and New Frontiers, *Reviews of Geophysics*, 60, e2021RG000744,  
1598 <https://doi.org/10.1029/2021RG000744>, 2022.

1599 [Walawender, M. J., Gastil, R. G., Clinkenbeard, J. P., McCormick, W. V., Eastman, B. G., Wernicke, R. S.,  
1600 Wardlaw, M. S., Gunn, S. H., and Smith, B. M.: Chapter 1: Origin and evolution of the zoned La Posta-type  
1601 plutons, eastern Peninsular Ranges batholith, southern and Baja California, in: \*Geological Society of America  
1602 Memoirs\*, vol. 174, Geological Society of America, 1–18, <https://doi.org/10.1130/MEM174-p1>, 1990.](https://doi.org/10.1130/MEM174-p1)

1603 Walter, B., Géraud, Y., Bartier, D., Kluska, J.-M., Diraison, M., Morlot, C., and Raisson, F.: Petrophysical and  
1604 mineralogical evolution of weathered crystalline basement in western Uganda: Implications for fluid transfer and  
1605 storage, *Bulletin*, 102, 1035-1065, <https://doi.org/10.1306/0810171610917171>, 2018.

1606 Wang, C., Alard, O., Lai, Y.-J., Foley, S. F., Liu, Y., Munnikhuis, J., and Wang, Y.: Advances in in-situ Rb–Sr  
1607 dating using LA-ICP-MS/MS: applications to igneous rocks of all ages and to the identification of unrecognized  
1608 metamorphic events, *Chemical Geology*, 610, 121073, <https://doi.org/10.1016/j.chemgeo.2022.121073>, 2022.

1609 Weinberg, R. F., Wolfram, L. C., Nebel, O., Hasalová, P., Závada, P., Kylander-Clark, A. R. C., and Becchio, R.:  
1610 Decoupled U–Pb date and chemical zonation of monazite in migmatites: The case for disturbance of isotopic  
1611 systematics by coupled dissolution-precipitation, *Geochimica et Cosmochimica Acta*, 269, 398-412,  
1612 <https://doi.org/10.1016/j.gca.2019.10.024>, 2020.

1613 Willigers, B. J. A., Mezger, K., and Baker, J. A.: Development of high precision Rb–Sr phlogopite and biotite  
1614 geochronology; an alternative to <sup>40</sup>Ar/<sup>39</sup>Ar tri-octahedral mica dating, *Chemical Geology*, 213, 339-358,  
1615 <https://doi.org/10.1016/j.chemgeo.2004.07.006>, 2004.

1616 Woodhead, J. D. and Hergt, J. M.: Strontium, Neodymium and Lead Isotope Analyses of NIST Glass Certified  
1617 Reference Materials: SRM 610, 612, 614, *Geostandards Newsletter*, 25, 261-266, [https://doi.org/10.1111/j.1751-  
1618 908X.2001.tb00601.x](https://doi.org/10.1111/j.1751-1751-908X.2001.tb00601.x), 2001.

1619 Worden, J.M., Cumming, G.L., and Baadsgaard, H.: Geochronology of host rocks and mineralization of the  
1620 Midwest uranium deposit, northern Saskatchewan, In: Sibbald, T.I., Petruk, W. (Eds.), *Geology of Uranium  
1621 Deposits*, Canadian Institute of Mining and Metallurgy, 32, 67-72, 1985.

1622 Yardley, B. W. D.: Quartz veins and devolatilization during metamorphism, *JGS*, 140, 657-663,  
1623 <https://doi.org/10.1144/gsjgs.140.4.0657>, 1983.

1624 Yardley, B. W. D. and Bodnar, R. J.: Fluids in the Continental Crust, *GeochemPersp*, 3, 1-127,  
1625 <https://doi.org/10.7185/geochempersp.3.1>, 2014.

1626 Yeo, G. M. and Delaney, G.: The Wollaston Supergroup, stratigraphy and metallogeny of a Paleoproterozoic  
1627 Wilson cycle in the Trans-Hudson Orogen, Saskatchewan, <https://doi.org/10.4095/223746>, 2007.

1628 Zack, T. and Hogmalm, K. J.: Laser ablation Rb/Sr dating by online chemical separation of Rb and Sr in an oxygen-  
1629 filled reaction cell, *Chemical Geology*, 437, 120-133, <https://doi.org/10.1016/j.chemgeo.2016.05.027>, 2016.

1630 Zametzer, A., Kirkland, C. L., Barham, M., Hartnady, M. I. H., Bath, A. B., and Rankenburg, K.: Episodic alteration  
1631 within a gold-bearing Archean shear zone revealed by in situ biotite Rb–Sr dating, *Precambrian Research*, 382,  
1632 106872, <https://doi.org/10.1016/j.precamres.2022.106872>, 2022.

1633